Characterization of Dust-Plasma Interactions In Non-Thermal Plasmas Under Low Pressure and the Atmospheric Pressure

A THESIS

SUBMITTED TO THE FACULTY OF THE GRADUATE SCHOOL

OF THE UNIVERSITY OF MINNESOTA

BY

Narula Bilik

IN PARTIAL FULFILLMENT OF THE REQUIREMENTS

FOR THE DEGREE OF

Doctor of Philosophy

Prof. Uwe R. Kortshagen, Adviser

March, 2016

Acknowledgements

I would like to thank my adviser, Professor Uwe Kortshagen, for his guidance and mentoring. I would like to thank the members on my thesis exam committee for their help and advise. I would also like to thank friends, family, and the student and faculty members of the University of Minnesota High Temperature and Plasma Lab for their kind support.

Abstract

This dissertation research focuses on the experimental characterization of dust-plasma interactions at both low and atmospheric pressure. Its goal is to fill the knowledge gaps in (1) the fundamental research of low pressure dusty plasma electrons, which mainly relied on models with few experimental results; and (2) the nanoparticle synthesis process in atmospheric pressure uniform glow plasmas (APGDs), which is largely unexplored in spite of the economical advantage of APGDs in nanotechnology.

The low pressure part of the dissertation research involves the development of a complete diagnostic process for an argon-siline capacitively-coupled RF plasma. The central part of the diagnostic process is the Langmuir probe measurement of the electron energy probability function (EEPF) in a dusty plasma, which has never been measured before. This is because the dust particles in the plasma cause severe probe surface contamination and consequently distort the measurement. This problem is solved by adding a solenoid-actuated shield structure to the Langmuir probe, which physically protects the Langmuir probe from the dust particle deposition to ensure reliable EEPF measurements. The dusty plasma EEPFs are characterized by lower electron density and higher electron temperature accompanied by a drop in the low energy electron population. The Langmuir probe measurement is complemented with other characterizations including the capacitive probe measurement, power measurement, and dust particle collection. The complete diagnostic process then gives a set of local plasma parameters as well as the details of the dust-electron interactions reflected in the EEPFs. This set of data serves as input for an analytical model of nanoparticle charging to yield the time evolution of nanoparticle size and charge in the dusty plasma.

The atmospheric pressure part of the dissertation focuses on the design and development of an APGD for zinc oxide nanocrystal synthesis. One of the main difficulties in

maintaining an APGD is ensuring its uniformity over large discharge volume. By examining past atmospheric pressure plasma reactor designs and looking into the details of the atmospheric pressure gas breakdown mechanism, three design features are proposed to ensure the APGD uniformity. These include the use of a dielectric barrier and the RF driving frequency, as well as a pre-ionization technique achieved by having a non-uniform gap spacing in a capacitively-coupled concentric cylinder reactor. The resulting APGD reactor operates stably in the abnormal glow regime using either helium or argon as the carrier gas. Diethylzinc (DEZ) and oxygen precursors are injected into the APGD to form zinc oxide nanocrystals. The physical and optical properties of these nanocrystals are characterized, and the system parameters that impact the nanoparticle size and deposition rate are identified.

Contents

List of Tables

List of Figures

Chapter 1

Introduction

1.1 Plasma

Plasma is a form of ionized gas composed of charged and neutral particles. By definition, a plasma is quasi-neutral and its constituent charged particles exhibit a collective behavior. This means the total positive charge is equal to the total negative charge in the plasma, and the charged particles oscillate collectively at a natural frequency due to the long range Coulomb force. The physics of the plasma particles is thus governed by the Maxwell's equations as well as the momentum and energy conservation laws. Further complications such as the presence of dust particles, the addition of the magnetic field, and possible chemical reactions make the plasma system complex to predict and model.

Plasmas exist both in nature and in man-made reactors and operate under very different conditions. Figure 1.1 shows the operation regimes of a variety of plasmas as a function of the plasma density n and the electron temperature T_e; λ_{De} is the Debye length, which will be discussed in the next chapter [1]. This dissertation specifically focuses on the regime labeled the "glow discharge", which is the regime most relevant to the semiconductor manufacturing industry. Glow discharge typically has the following properties: (1) it is driven electrically rather than thermally; (2) it is non-thermal—the neutral gas temperature, typically ranging from the room temperature up to a few hundred degrees celsius, is much lower than the electron temperature; (3) it is driven at the DC, kHz or

radio frequency (RF); (4) it is weakly ionized: $n_i/(n_g + n_i) \ll 1$, where n_i and n_g are the ion density and the neutral gas density, respectfully.

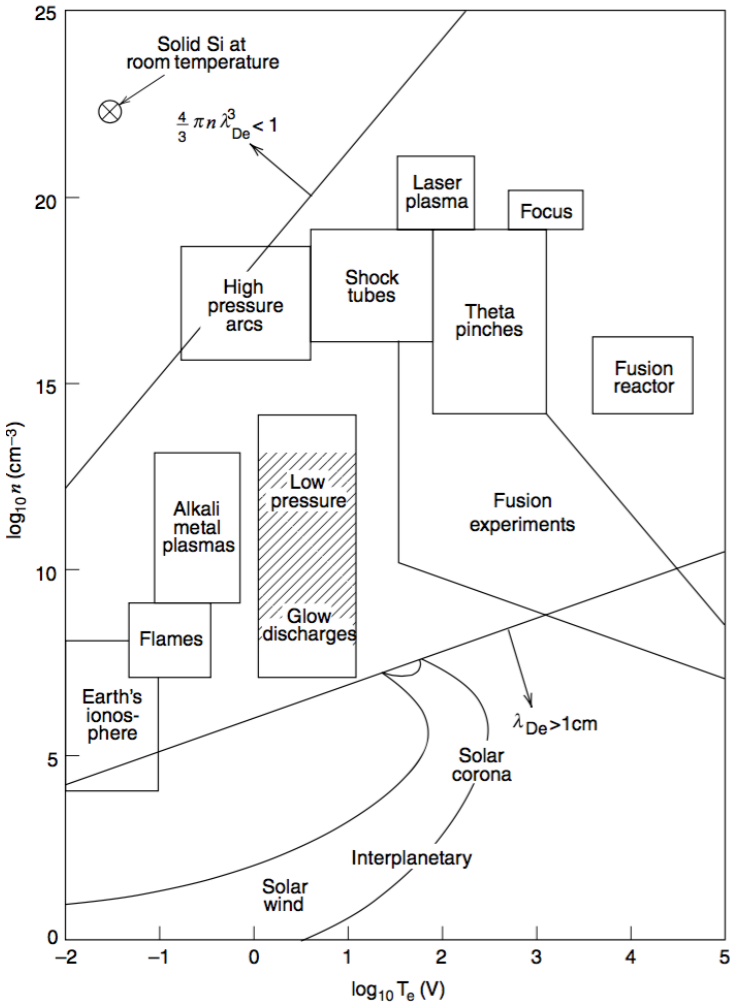

Figure 1.1: Operation regimes of plasmas as a function of density and electron temperature on a log-log plot [1].

Dusty (or complex) plasmas, the main subject of the dissertation research, are plasmas containing charged solid particles with dimensions much less than the Debye length (on the order of nanometers or micrometers) [2, 3]. They are found in interstellar clouds, in the mesosphere, and most relevantly, in industrial processing plasmas. Processing plasmas are typically chemically reactive and the dust particles may form as part of the reaction byproduct. Even in noble gas discharges, dust particles can emerge from chamber wall depositions [4]. In industrial etching plasma reactors used for integrated circuit manufacturing, these dust particles can nucleate and land on the substrate surface,

leading to defects and possibly equipment down-time [5–7]. In the case of plasma-assisted nanoparticle synthesis in laboratory settings, however, these dust particles are the final product of interest and often exhibit interesting optical and electrical properties [8–11].

Motivated by interests in both astrophysics and nanotechnology, dusty plasma science has been a fast-growing field of research. Early dusty plasma research focused on the dust acoustic wave patterns, which continue to attract strong interest today [12–19]. In the 1990s, interest in the dusty plasma was boosted by the discovery of plasma crystals—ordered structures formed by the dust particles in the discharge [20–23]. This eventually lead to the surge of interest in dusty plasmas under microgravity conditions in the early 2000s [24–26]. Recently, magnetized dusty plasmas have been attracting attention due to their potential significance in astrophysics [27, 28]. Meanwhile, fundamental research of the physical interactions between the dust particles and the plasma species continued throughout the decades [8, 14, 29–49]. Such research focused on the modeling and simulation of the nucleation, growth and charging of the dust particles, as well as their interactions with the electrons and ions. Today, a complete understanding of these interactions is yet to be achieved. This is partially due to the lack of experimental methods to directly measure these interactions.

This dissertation also examines the dust-plasma interactions at the atmospheric pressure. Glow discharges operating at the atmospheric pressure are rare today, but they have drawn strong interests in the past decades due to their low cost and potential biomedical applications. Maintaining a glow discharge at atmospheric pressure is difficult, since the electron and gas temperatures tend to equalize under such high pressure. In 1988, Kanazawa *et al.* developed the first stable, large-volume and uniform atmospheric pressure glow discharge (APGD) reactor [50]. In the 1970s, the development of the APGDs was facilitated by the research of atmospheric pressure gas lasers. Since then, various reactor geometries and techniques have been utilized to ensure the stability and uniformity of such reactors [51–62]. Today, atmospheric pressure plasma-assisted nanoparticle synthesis is an increasingly popular topic of research. A few atmospheric pressure plasma

reactors have been developed for the synthesis of silicon and carbon nanoparticles [63–68]. However, these reactors are not technically large volume APGDs due to their small size or filamentary nature.

1.2 Plasma Application in Nanotechnology

The nano-manufacturing industry relies on plasma-assisted processes to produce integrated circuits and solar cells. This is because plasma-assisted processes have a unique set of advantages. In a typical glow discharge reactor, while the temperature of the neutral gas molecules remain relatively low, the high energy plasma electrons can sustain chemical reactions that are difficult to initiate using other commercial processes. For etching applications, the presence of the capacitive plasma sheath allows the control of the ion bombardment energy. In plasma-assisted deposition reactors, plasma electrons help breaking down the precursor chemicals, significantly improving the chemical reaction rate. Plasma-assisted processes also have an environmental advantage since they produce minimal pollution compared to solvent-based processes. Figure 1.2 shows the role of plasma etching in a pattern transfer process during the manufacturing of integrated circuits [69]. As shown in step three, plasma etching is responsible for stripping away the film layer according to the photoresist pattern through ion-surface interactions—a combination of physical sputtering and chemical reactions. This process is repeated to build up layers of patterned materials to form the desired integrated circuits.

Four key factors determine the quality of the final etch product: the etch rate, the uniformity, the selectivity, and the anisotropy (the horizontal etch rate relative to the vertical etch rate). High degree of anisotropy is critical for etching a large number of narrow vertical channels within a small area of the substrate. This is especially important to the semiconductor industry, where the demand for higher transistor counts per unit area is constant. Plasma-assisted processing proved to be a reliable mean to achieve such high degree of anisotropy. To illustrate this, figure 1.3 shows the side view of a 0.2 μm by 4 μm trench etched in a silicon substrate using plasma-assisted processes.

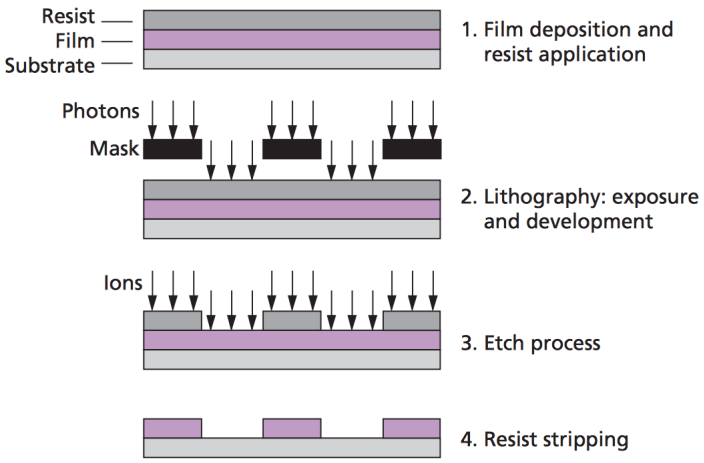

Figure 1.2: Basic pattern transfer process in circuit manufacturing [69].

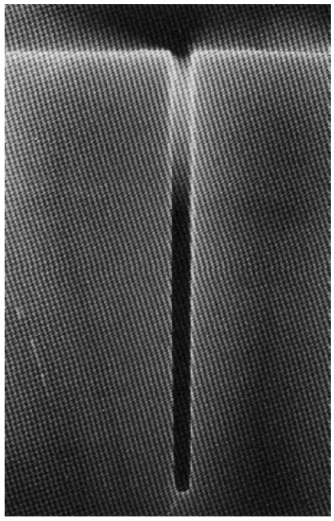

Figure 1.3: Plasma-etched 0.2 μm by 4 μm trench in a single crystal silicon [1].

Innovative plasma reactor designs allow the independent control of the ion flux and the ion temperature in the etching process. The ion temperature, which influences the ion bombardment energy, is determined by the voltage drop across the capacitive sheath. While capacitive plasma reactors have the desirable sheath properties, they usually have low plasma densities and thus low ion flux. To address this issue, a variety of hybrid or dual frequency systems have been developed [1, 69, 70]. In a typical hybrid system, an inductively coupled plasma acts as a high density source, and a secondary capacitive source drives the substrate to achieve the desirable capacitive sheath voltage drop. In a dual frequency system, a high frequency source generates the high plasma density, while

the low frequency source creates the large sheath voltage drop over the substrate. As discusses earlier, the presence of dust particles in these industrial plasmas continues to be a challenge. This is especially true as the circuit features become increasingly small. Today, experimentalists and computer simulation scientists continue to study the transport of dust particles in plasma reactors in order to design systems and recipes that minimizes the wafer contamination and wall deposition.

Plasma is not only essential to the nano-manufacturing industry, it also plays an important role in the laboratories. When used for nanoparticle synthesis, the plasma efficiently heats the particles through energetic surface reactions; this makes the particles crystalize even when the neutral gas molecules are close to the room temperature [11,71]. Due to the difference between the electron and ion mobilities, the synthesized particles are negatively charged, leading to lower agglomeration and less wall deposition. These unique advantages have lead to many successful attempts of plasma-assisted nanocrystal synthesis in research laboratories, where nanocrystals with novel properties are produced as the building blocks for electronics such as thin film solar cells, nano-scale light emitters, thermoelectrics, and transparent conducting films [8–11,72–76]. Figure 1.4 shows a series of plasma-synthesized silicon nanocrystals exhibiting light emissions in the visible spectrum after being excited by a UV lamp. The light emissions originate from both quantum confinement and surface defects. This demonstrates the plasma synthesis process's extraordinary ability to fine-tune the nanocrystal size and therefore their emission properties [77].

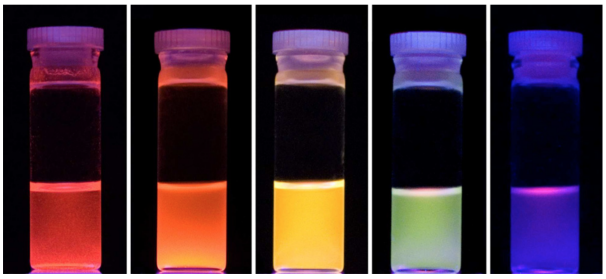

Figure 1.4: Light emission due to quantum confinement and surface defects by plasma-synthesized silicon nanocrystals dispersed in methanol and exposed to UV radiation [77].

1.3 Motivation

Currently, plasma-synthesized nanocrystals are mainly produced in laboratory settings in small quantities with few industrial adaptations. In order to make the synthesis process more attractive to industries, it is desirable to reduce the cost of the process and increase the production quantity. Both of these goals can be achieved by shifting the plasma synthesis process from the low pressure to the atmospheric pressure. Today, most plasma reactors operate at low pressures; in order to achieve the low pressure, large and expensive vacuum equipment (vacuum-tight stainless steel chambers, piping and flanges, etc.) must be purchased and maintained. Compared to low pressure reactors, atmospheric pressure plasma reactors are extremely attractive. This is because at the atmospheric pressure, expensive vacuum equipment such as the turbopumps and stainless steel vacuum chambers can be replaced by simple mechanical pumps and non-airtight plastic containers to greatly reduce the cost.

There are two main challenges in developing an atmospheric pressure nanocrystal synthesis plasma. First, nanoparticle-plasma (or dust-plasma) interaction is not fully understood. So far, understanding of these interactions has concentrated on low pressure plasmas and mostly relied on computer simulations, with very few experimental results [40–49, 78]. The second challenge is the difficulty in developing a large-volume atmospheric pressure plasma source due to electrical and thermal instabilities. Most atmospheric pressure glow plasma sources today are microplasmas with a small production yield [65–67, 79–82].

This dissertation research then focuses on addressing these two challenges through a series experimental efforts. It aims to (1) develop a reliable and complete diagnostic process to fully characterize a dusty plasma system, including electrical probe measurements that directly measures the dust-electron interactions for the first time; and to (2) develop and characterize a stable and low cost APGD plasma source for nanocrystal synthesis.

By achieving these goals, the dissertation research will facilitate the understanding of the dust-plasma interactions at both the low pressure and the atmospheric pressure. It

will establish a foundation for the development of an accurate physical model of a dusty plasma system, as well as the basis for future theoretical and experimental studies of APGDs to achieve the final goal of shifting the plasma processes from the low pressure to the atmospheric pressure.

1.4 Structure of Thesis

- Chapter 2 discusses the background information necessary to understand the experimental characterization of low pressure dusty plasmas.
- Chapter 3 describes the experimental method and the system used in the low pressure dusty plasma characterization.
- Chapter 4 presents the experimental results and data analysis associated with the low pressure dusty plasma system.
- Chapter 5 discusses the background information necessary to understand the development of a large volume APGD system for nanocrystal synthesis.
- Chapter 6 describes the APGD system and the experimental procedures for nanocrystal synthesis.
- Chapter 7 presents the experimental results and data analysis associated with the APGD system.
- Chapter 8 presents the conclusion of the presented research.

Chapter 2

Low Pressure Plasma Diagnostics: Background

2.1 Capacitively Coupled Plasma Source

The main subject of the dissertation research is the capacitively-coupled plasma (CCP) source. This section introduces the basic physics of such source that is essential to the understanding the dissertation research.

A basic model of the CCP consists of a plasma discharge generated between two electrodes. One electrode is grounded and the other one is driven by a power source. The electron and ions respond to the applied electric field differently depending on the driving frequency. Electrons are able to respond to field oscillations below the electron plasma frequency:

$$\omega_{pe} = \sqrt{\frac{e^2 n}{\epsilon_o m_e}}, \tag{2.1}$$

where m_e is the electron mass. Since ions have a much larger mass, the ion plasma frequency is much lower than the electron plasma frequency:

$$\omega_{pi} = \sqrt{\frac{e^2 n}{\epsilon_o m_i}}, \tag{2.2}$$

where m_i is the ion mass. For low pressure CCPs, ω_{pe} is typically in the 1 GHz range and ω_{pi} is typically in the 1 MHz range. For RF plasmas, this often means the electron motion is able to respond to the applied field oscillation while the ion motion cannot.

One major difference between a CCP and a capacitor is the flow of the electrical current through the devices. In a true capacitor, there is no actual charge transport through the dielectric between the capacitor plates, and the current flow is given by the displacement current. A plasma discharge, on the other hand, has both capacitive and conductive (or dielectric) properties. The total current flow through a CCP discharge is the summation of the displacement current and the conduction current:

$$J_{rf} = \epsilon_o \frac{\partial E}{\partial t} + J, \tag{2.3}$$

where E is the electric field and J is the conduction current.

The plasma discharge then divides into two regions: the bulk plasma region and the sheath region at the plasma boundaries. The bulk region is quasi-neutral: $n = n_e = n_i$, where n_e is the electron density and n_i is the ion density. Due to the charge shielding effect, significant electric field can only exist within the Debye length given by

$$\lambda_{De} = \sqrt{\frac{\epsilon_o k T_e}{e n}}, \tag{2.4}$$

where e is the elementary charge and k is the Boltzmann's constant. The sheath region, on the other hand, is a region of positive space charge where $n_i > n_e$. The sheath forms due to the difference between m_e and m_i. Since $m_i \gg m_e$, the electron thermal velocity is much greater than the ion thermal velocity, leading to the rapid loss of electrons to the walls and a net positive space charge within the sheath. This establishes a significant sheath electric field that points toward the plasma boundary (such as a floating chamber wall). The sheath electric field directs the electrons into the bulk plasma and accelerates the ions towards the wall, thus sustaining the discharge. In order to maintain the positive space charge within the sheath, the ions are accelerated in a region between the bulk and

the sheath called the presheath, and enter the sheath at the Bohm velocity:

$$u_b = \sqrt{\frac{eT_e}{m_i}}. \tag{2.5}$$

This velocity must be achieved in order to satisfy the ion energy conservation and the ion flux continuity across the bulk and the sheath regions. The drop of the potential profile across the sheath means the potential of the surface at the plasma boundary will always be negative compared to V_s, the plasma potential. The difference between V_s and the electrode potential is called the DC bias, corresponding to the voltage drop across the sheath. Consider two electrodes A and B where A is driven and B is grounded. The grounded electrode naturally gains a larger effective surface area. As a result of such asymmetry, the sheath voltage drop at A is greater than the sheath voltage drop at B. The difference between the two voltage drops is called the self bias. Since there is no significant electric field in the bulk region, the current in the bulk region can be approximated as the conduction current. Similarly, there is little conduction current in the sheath region due to the low electron density, and the current in the sheath region is mainly given by the displacement current. Most of the applied RF voltage is dropped across the sheath and little is dropped across the bulk region.

Macroscopically, the RF CCP can be modeled as a homogeneous (not considering spacial variation within the bulk and the sheath) circuit model shown in figure 2.1. I_{rf} represents the power source, and C_o, L_p and R_p correspond to the bulk capacitance, inductance and resistance; the current through the sheaths is represented by $\bar{I}_i$, while C_a and C_b, R_a and R_b represents the capacitance and resistance (due to stochastic heating) of the two sheaths. The dashed line indicates that the nonlinear elements C_a, C_b, R_a and R_b combine to yield the linear elements C_s and R_s, the total sheath capacitance and resistance [1].

While it is practical to consider the time-averaged sheath properties, it is also useful to understand that these properties do vary over a RF cycle as the the sheath collapses and expands. Figure 2.2 shows the time-varying plasma potential, the driven electrode

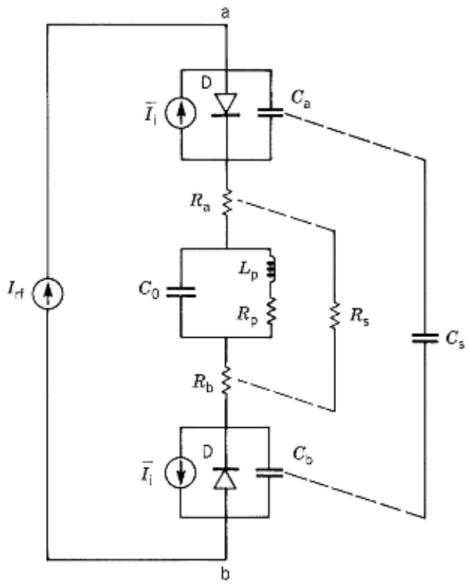

Figure 2.1: Nonlinear circuit model of a homogeneous RF plasma discharge. The linear elements C_s and R_s are resulted from the nonlinear elements C_a and C_b, and R_a and R_b, as indicated by the dashed line [1].

potential, the electron current and the ion current over RF cycles. The DC bias is clearly observed: the driven electrode potential is always below the plasma potential. A spike of the electron conduction current appears during the sheath collapse (when the electrode potential is equal to the plasma potential). The ion current is very small due to the low ion mobility and is nearly constant [83].

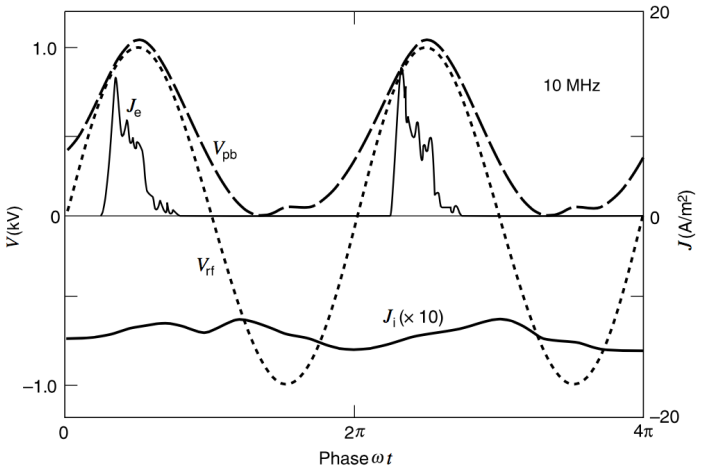

Figure 2.2: Time-varying plasma potential V_{pb}, driven electrode potential V_{rf}, electron current J_e and ion current J_i over RF cycles. The ion current is plotted ten times larger [83].

2.2 Dust Transport and Charging

As introduced in the first chapter, dusty plasmas contain charged solid particles with dimensions much less than the Debye length. This dissertation mainly focuses on the charging of the dust particles by the electrons and ions, while considering some dust transport and growth phenomena. For the study of dust acoustic waves and crystal formation in strongly coupled plasmas, please refer to the review paper by Shukla [2]. Due to the large difference between electron and ion mobilities, dust particles usually have a negative charge (under some conditions the particles can acquire a positive charge due to the electron emission by UV irradiation or heating). The interaction between the dust particles and the charged species is one of the most important factors governing the dust motion and growth. Such interactions, however, are challenging to predict and model due to its non-linear and non-equilibrium nature. For example, the electron flux to the particle is determined by the electron energy distribution and the particle potential, both of which can be updated by the incoming electron flux and the particle growth over time.

The motion of dust particles in the plasma is determined by five main forces. First is the force due to the electric field expressed as $F_e = Q_d E$, where Q_d is the particle charge. The second force is the ion drag force, which tends to push the particles outward towards the sheath. The ion drag force is the summation of two parts—the ion drag due to the ions collected by the particle, and the ion drag due to the ion-particle Coulomb scattering:

$$F_i = m_i n_i v_{i,\text{eff}} u_i (\pi b_c^2 + \pi b_o^2 \text{Ln}\Lambda), \tag{2.6}$$

where $v_{i,\text{eff}}$ is the ion effective velocity, u_i is the ion drift velocity, b_c is the ion collection radius calculated assuming an orbital motion limited (OML) ion current, b_o is the impact parameter for ion-dust Coulomb scattering, and Λ is the Coulomb logarithm [1]. The remaining three forces are the neutral drag force, the gravitational force, and thermophoresis in plasmas with large temperature gradients (originating from the difference in the momentum transfer cross sections between the hot side and the cold side of the

particle).

Due to these forces, dust particles in the plasma typically have a non-uniform and time-evolving spatial distribution. Since these forces scale differently with a, the particle radius, the particle spatial distribution has a strong time dependence as the particles nucleate and grow in size. The temporal evolution of the dust spatial distribution has been extensively monitored using laser scattering techniques for a variety of discharge conditions [33, 84–89]. These studies are typically motivated by the need to keep the dust contaminations from the substrate during the plasma etching process. Since the gravitational force scales with a^3, for submicron-sized particles the gravity is negligible, and the most important forces are the ion drag force F_i and the electrostatic force F_e. While F_i drives the particles towards the sheath, F_e directs the negatively charged particles inward towards the bulk. As a result of this force balance, most particles are confined near the sheath region. Scaling-wise, F_i scales with a^2 and F_e scales with a. This implies that as the particles grow larger, F_i becomes more dominant and causes an expansion of the particle spatial distribution away from the center region [84]. The balance between these two forces then evolves with time, often leading to void regions within the distribution. One method to reduce the expansion of the particles into the sheath region is to restrict their growth. This is often achieved by using pulsed discharges. During the off phase, gravity dominates since the dust particles lose their negative charge.

The most widely used model for particle charging is based on the OML theory, which assumes collisionless electron and ion orbits around the particle, and expresses the electron and ion currents based on the conservation of energy and angular momentum [90]. Since a dust particle in the plasma can be approximated as a sphere, assuming isotropic Maxwellian distributions for the charged species, the OML electron and ion currents to the particle can be expressed as

$$I_e = \pi a^2 e n_e \sqrt{\frac{8kT_e}{\pi m_e}} \exp(\frac{eV_p}{kT_e}), \tag{2.7}$$

and

$$I_i = \pi a^2 e n_i \sqrt{\frac{8kT_i}{\pi m_i}} \exp(1 - \frac{eV_p}{kT_i}), \tag{2.8}$$

where V_p is the particle potential and T_i is the ion temperature. Since the particle is at the floating condition, the particle potential can be calculated by equating the electron current to the ion current:

$$eV_p = -T_e[\mathrm{Ln}(\frac{m_i}{m_e}\frac{T_e}{T_i}\frac{n_e^2}{n_i^2})^{1/2} - \mathrm{Ln}(1 - \frac{eV_p}{T_i})]. \tag{2.9}$$

This OML model is only applicable to a small range of particle and plasma regimes due to its set of simplifying assumptions. Numerous models have been developed to modify the OML theory to extend its validity over a wider range of regimes [29, 90–94]. For example, the OML theory neglects the trapped ions—ions generated by the charge-exchange collisions in the particle sheath region and are trapped around the particle. Neglecting the effect of these ions leads to an over-prediction of the negative particle potential [39, 95, 96]. In 2008, Gatti and Kortshagen developed an analytical model for particle charging which takes the trapped ions into account, and is valid over a wide range of pressure regimes [39]. The model defines the concept of an ion capture radius R_o: the radius around the dust particle at which the ion potential energy is equal to its kinetic energy. An ion within this radius will be eventually captured by the particle:

$$R_o = \frac{e|V_p|a(1 + \frac{a}{\lambda_{DL}})}{E_{kin} + e|V_p|\frac{a}{\lambda_{DL}}}, \tag{2.10}$$

where E_{kin} is the ion kinetic energy and λ_{DL} is the dusty plasma Debye length defined by $1/\lambda_{DL}^2 = 1/\lambda_{Di}^2 + 1/\lambda_{De}^2$, where λ_{Di} is the ion Debye length and λ_{De} is the electron Debye length. The model then defines an ion capture Knudsen number $Kn_{R_o} = \lambda_i/(2\alpha_o R_o)$ where λ_i is the ion mean free path and $\alpha_o = 1.22$ arrises from integrating R_o over a Maxwellian ion energy distribution. Note that for $a \ll \lambda_{De}$, $R_o \approx (e|V_p|\alpha)/E_{kin}$. It is worth pointing out that the analytical model has only a weak dependence on the ion energy

distribution function–integrating over Maxwellian and non-Maxwellian ion energy distributions give similar results. Taking advantage of the newly defined ion capture Knudsen number, the model expresses the total ion current to the particle as the summation of the ion currents in three pressure regimes, each weighed by their relative probability:

$$I_i = P_0 I_i^{OML} + P_1 I_i^{CE} + P_{>1} I_i^{HY}, \tag{2.11}$$

where I_i is the total ion current, I_i^{OML}, I_i^{CE} and I_i^{HY} are the ion currents in the low pressure OML regime, the transitional collision enhanced regime, and the high pressure hydrodynamics regime respectively; P_0, P_1 and $P_{>1}$ are the probabilities of an ion performing zero, one and more than one collisions within the capture radius, respectively. The expressions for the currents in the three regimes can be found in literature, and the probabilities are functions of Kn_{R_o} and are evaluated based on the Poisson distribution [97]. Finally, equating the ion current to the electron current, the model arrives at a modified version of equation 2.9. It expresses the particle potential (and therefore charge) as a function of measurable plasma parameters:

$$\begin{aligned}\frac{n_i}{n_e}\sqrt{\frac{M}{\tau}}\Big\{(1+\tau z) + \frac{2[2\alpha_o z\tau(\eta+1)]^3}{Kn_a(3\eta+2z\tau)^3} + \frac{3\pi}{4\sqrt{2}}Kn_a\tau z\Big[\exp\Big(\frac{4\alpha_o z\tau(\eta+1)}{Kn_a(3\eta+2z\tau)}\Big) \\ -\Big(1+\frac{4\alpha_o z\tau(\eta+1)}{Kn_a(3\eta+2z\tau)}\Big)\Big]\Big\} \times \exp\Big(-\frac{4\alpha_o z\tau(\eta+1)}{Kn_a(3\eta+2z\tau)}\Big)\exp(z) = 1,\end{aligned} \tag{2.12}$$

where M, τ, z, Kn_a and η are dimensionless parameters: $M = m_e/m_i$, $\tau = T_e/T_i$, $z = (-eV_p)/(kT_e)$, $Kn_a = \lambda_i/a$, and $\eta = \lambda_{DL}/a$. An accurate way to experimentally measure these properties is to monitor the electron energy distribution function. The electron energy distribution not only allows the derivation of the electron density and the electron temperature, it also contains detailed information about the electron-dust interactions. The next section introduces the basics of the electron energy distribution function and its relation to local plasma properties.

2.3 Electron Energy Distribution Function

The distribution function of a particular particle species can be written as $F(\vec{r}, \vec{v}, t)$; it specifies the population of the species at $\vec{r}$ (position) and $\vec{v}$ (velocity) as a function of t (time). Integrating F over a six dimensional position and velocity phase space then gives the total number of that species at a particular time. Considering particles flowing in and out of a control volume in a six dimensional phase space defined by $\vec{r}$ and $\vec{v}$, a general form of the particle conservation can be expressed using the concept of the distribution function:

$$\frac{\partial F}{\partial t} + \vec{v} \cdot \nabla_r F + \vec{a} \cdot \nabla_v F = \left.\frac{\partial F}{\partial t}\right|_c . \tag{2.13}$$

This is the Boltzmann equation, from which a variety of particle energy and momentum conservation laws can be derived. The left hand side of the equation is in the form of a material derivative, where the first term accounts for the variation of F in time, and the second and third terms are convective derivatives that account for the variations of F in the spaces defined by $\vec{r}$ and $\vec{v}$. The right hand side of the equation is the collision term, which represents the particles suddenly "appearing" and "disappearing" within the control volume due to short time scale interactions that occurs faster than the evolution time of F.

The electron distribution function (EDF) is then simply the distribution function applied to the electron population. For probe measurements, the electron distribution is usually measured at a particular position and a particular time and therefore is only a function of $\vec{v}$, and can be written as $f(\vec{v})$, the electron velocity distribution. Assuming the electrons are isotropic and simplifying $f(\vec{v})$ to the electron speed distribution $f(v)$, the electron energy distribution function (EEDF) $g(\varepsilon)$ can be derived:

$$g(\varepsilon) = 2\pi(2e/m_e)^{3/2}\varepsilon^{1/2} f(v(\varepsilon)), \tag{2.14}$$

where $v(\varepsilon) = (2e\varepsilon/m_e)^{1/2}$. The electron energy probability function (EEPF), a normalized

version of the EEDF is often used instead:

$$f_p(\varepsilon) = \varepsilon^{-1/2} g(\varepsilon). \tag{2.15}$$

When the electron population is in thermal equilibrium without time variation, spatial gradient or acceleration, its speed distribution is given by the Maxwellian distribution:

$$f_{Maxwellian}(v) = n(\frac{m_e}{2\pi kT})^{3/2} \exp(-\frac{m_e v^2}{2kT}). \tag{2.16}$$

The corresponding Maxwellian EEPF is

$$f_{Maxwellian,p}(\varepsilon) = \frac{2}{\sqrt{\pi}} n_e T_e^{-3/2} e^{-\varepsilon/T_e}. \tag{2.17}$$

Note that $\mathrm{Ln}(f_{Maxwellian,p}(\varepsilon))$ is a linear function of ε.

EEPFs in weakly-ionized plasmas are typically non-Maxwellian. For non-Maxwellian plasmas, knowing the EEPF, either by experimental measurement or by modeling and solving the Boltzmann equation, allows the calculation of the the local electron density and the average electron temperature:

$$n_e = \int_0^\infty \sqrt{(\varepsilon)} f_p(\varepsilon) d\varepsilon, \tag{2.18}$$

and

$$T_e = \frac{2}{3} {n_e}^{-1} \int_0^\infty \varepsilon^{\frac{3}{2}} f_p(\varepsilon) d\varepsilon. \tag{2.19}$$

Generally, the average value of a function $h(v)$ (such as a collision cross section) can be obtained by averaging the function over the entire distribution:

$$< h(v) >= \frac{\int h(v) f(v) dv}{n_{species}}, \tag{2.20}$$

where $n_{species}$ is the density of the species.

ν_m, the electron-neutral elastic collision frequency, critically determines of the shape

of the distribution function. A Maxwellian distribution assumes that ν_m is constant. However, ν_m is usually dependent on the electron velocity:

$$\nu_m = n_g \sigma_m v, \tag{2.21}$$

where σ_m is the collision cross-section. If σ_m is assumed to be constant such as in hard-sphere collisions, the Druyvesteyn distribution is obtained [1]. Druyvesteyn distribution is characterized by a depleted high-energy tail compared to the Maxwellian and often more accurately captures the electron energy distributions in weakly ionized plasmas.

Real EEPFs are rarely perfectly Maxwellian or Druyevsteyn. Instead, they follow a generalized form: $f_{p,generalized}(\epsilon) = c_1 \exp(-c_2 \epsilon^n)$, where c_1, c_2 and n are constants [47]; for a perfectly Maxwellian distribution, $n = 1$ and for a perfectly Druyvesteyn distribution, $n = 2$. Most real EEPFs have n values between 1 and 2. A change from $n \approx 2$ to $n \approx 1$ is called Maxwellianization.

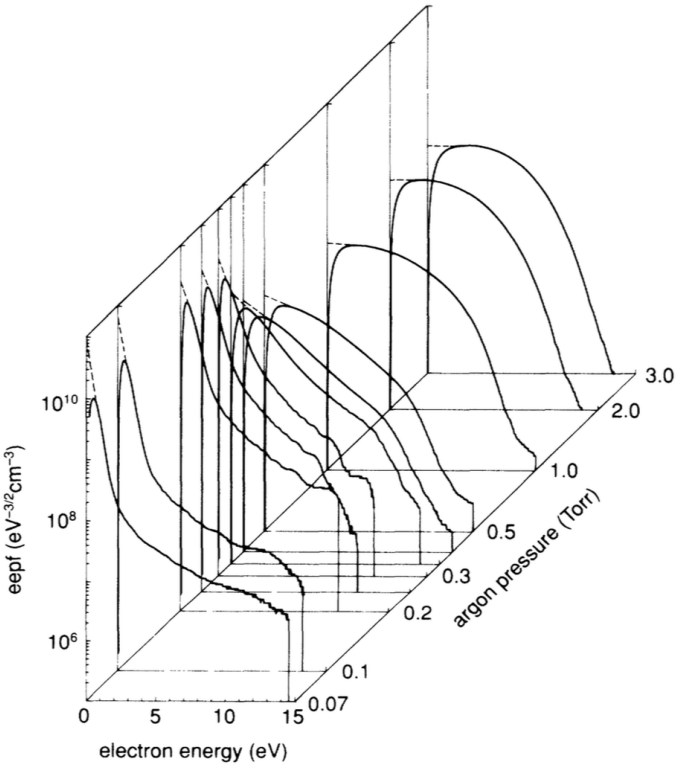

Figure 2.3: EEPF evolution with pressure in a low pressure RF CCP argon plasma [98].

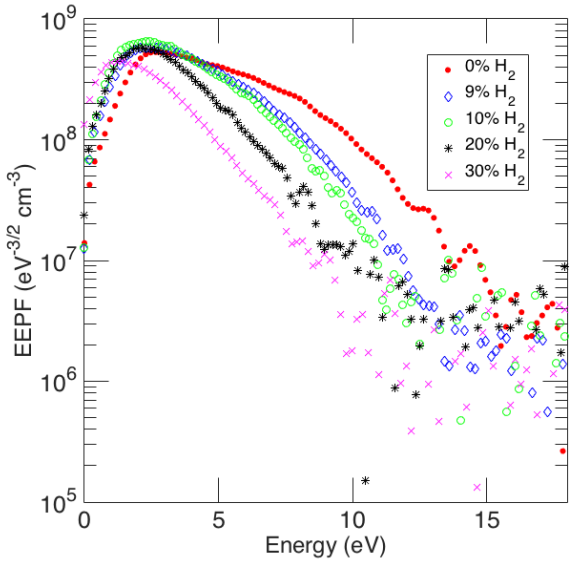

Figure 2.4: EEPF evolution with percent hydrogen in a low pressure RF CCP argon plasma; the percent is based on the hydrogen partial pressure.

Experimentally measured EEPFs not only provide local electron properties such as n_e and T_e, they also reveal the information about the physics and chemical reaction rates in the discharge. Figure 2.3 shows a series of EEPF measurements made by Godyak in a low pressure RF CCP argon plasma [98]. For higher pressure ranges, the EEPFs are Druyvesteyn-like. For low pressure ranges, the EEPFs evolve into a pattern that can be expressed as a summation of two Maxwellian-distributions with two temperatures. The two-temperature pattern is characterized by a low energy peak and a high energy tail, illustrating the transition of the electron heating mode from a collisional, ohmic heating mode to a stochastic, sheath-based heating mode. The stochastic heating mode divides the electrons into two populations: a higher energy population heated by the sheath field and efficiently ionizes the neutrals, and a lower energy population trapped in the bulk with a very low electron-neutral collision frequency. Figure 2.4 shows the evolution of EEPF with percent hydrogen in a low pressure ($\approx$ 500 mTorr) RF CCP argon plasma. The percent hydrogen is based on the hydrogen partial pressure. As the hydrogen content is increased, the EEPFs show an increased depletion of the electron population in the range of $4 - 14$ eV, corresponding to the hydrogen dissociation energy at 4.5 eV and the hydrogen atom ionization energy at 13.6 eV.

Since the EEPF contains detailed information about the electron's interactions with the other species, it is highly desirable to measure the EEPFs in dusty plasmas. This can be done using a Langmuir probe—an electrical probe that enables highly accurate measurements of EEPF in low pressure plasmas.

2.4 Langmuir Probe

Part of this section has been published in *Journal of Physics D: Applied Physics* in 2015 [99].

2.4.1 Current-Voltage Characteristics

A Langmuir probes is a conductor immersed in the plasma that draws electron or ion current depending on the applied probe bias V_e. The probe current voltage (I-V) characteristic can be used to determine the plasma potential (V_s), the floating potential (V_f), the electron saturation current (I_{es}), the ion saturation current (I_{is}) and the EEPF. Figure 2.5 shows a typical Langmuir probe I-V characteristic [100]. At point B, the probe bias V_e is at the floating potential: the electron and ion currents to the probe is the same resulting in zero net current. To the left side of the floating potential is the ion current (plotted negative) region, where the probe bias is negative and mostly ion current is collected. To the right side of the floating potential is the electron current region between point B and C. When the probe bias is close to the floating potential, the Langmuir probe collects only the most energetic electrons that are able to pass through the potential barrier; as the probe bias increases, the electron current also increases as the probe collects both energetic and low energy electrons. When the probe reaches the plasma potential at point C, the electron current saturates and the probe collects the electron current defined by the electron thermal velocity. If the probe is biased further beyond the plasma potential, the sheath around the probe expands. The sheath expansion increases the probe's effective collection area, and the electron current increases again as a result. The shape of the

region C-D depends on the probe geometry. For a planar probe, the expansion follows the Child Law:

$$d_s = \frac{\sqrt{2}}{3}\lambda_{De}(\frac{2(V_e)}{T_e})^{3/4}, \tag{2.22}$$

where d_s is the sheath thickness. Further biasing the probe beyond point D can lead to a sharp increase in the current (not shown in the figure) as the probe replaces one of the electrodes.

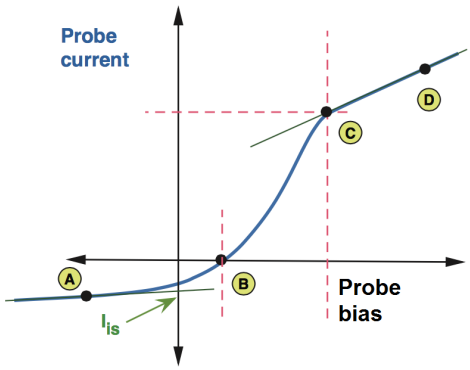

Figure 2.5: Typical Langmuir probe current-voltage curve in a non-thermal plasma [100].

Region C-D and region A-B in figure 2.5 demonstrate the electron saturation current I_{es} is much greater than the ion saturation current I_{is} due to the greater electron mobility. For a planar probe with a collisionless sheath, the magnitude of the ion saturation current is given by

$$I_{is} = 0.6 n_i e u_b A_p, \tag{2.23}$$

where A_p is the probe surface area and the factor 0.6 arises from the drop in n_i in the presheath region. The electron saturation current is given by the thermal flux:

$$I_{es} = \frac{1}{4} n_e e v_{e,th} A_p, \tag{2.24}$$

where $v_{e,th}$ is the electron thermal velocity. For a long (length $\gg$ radius) cylindrical probe with a collisionless sheath and local species under the isotropic Maxwellian distribution

such that the OML assumptions apply, the saturation current can be approximated by

$$I_{s,ei} = 2ena_p l\sqrt{\frac{2eV_e}{m}}, \tag{2.25}$$

where a_p is the probe radius, l is the probe length, $I_{s,ei}$ represents either I_{is} or I_{es} and m is the corresponding mass [1].

Equations 2.23, 2.24 and 2.24 make rather strong assumptions regarding the probe geometry and the electron velocity distribution. For different probe geometries and more dynamic discharge conditions, n_e and T_e should be derived from the measured EEPF using equations 2.18 and 2.19 instead of using the saturation currents. The EEPF can be obtained by taking the second derivative of the probe I-V characteristic using the Druyvesteyn method:

$$\frac{d^2 I_e}{dV_e^2} = -\frac{e^2 A_p \varepsilon}{4}\sqrt{\frac{2e}{m_e V_e}} f_p(\varepsilon), \tag{2.26}$$

where I_e is the electron probe current [4]. This method has two main advantages: it is independent of the probe geometry for all convex probes, and its is valid for all isotropic electron velocity distributions (including non-Maxwellian) [1]. However, it requires high precision in the measurement of the I-V characteristics.

2.4.2 Requirements for Reliable Langmuir Probe Measurements

Though the Langmuir probe appears to be a simple instrument and has been used since the beginning of the 20th century, great care must be taken in the construction of the probe and the interpretation of the probe data in order to achieve reliable results. This is because the measured EEPF depends on the second derivative of the probe I-V characteristic, a slight error in the probe measurement can lead to great error in the resulting EEPF and local plasma parameters. The Druyvesteyn method is valid only under strict conditions (for example, the plasma needs to be isotropic and under low pressure); for Langmuir probe measurements in special plasmas such as high pressure plasmas, magnetized plasmas and dusty plasmas, the probe geometry and the data interpretation method must be redesigned

accordingly. This subsection introduces a few basic requirements necessary for accurate probe measurements in a low pressure isotropic plasma, considering both the probe design criteria as well as the data interpretation guidelines.

The probe's physical design must help minimize the plasma and sheath perturbation. Generally speaking, the probe dimension should satisfy the small-probe assumption to ensure there is no electron-neutral collision in the probe sheath and presheath regions:

$$a_p \mathrm{Ln}[\frac{\pi l}{4a_p}], b_p, \lambda_{De} \ll \lambda_e \text{ and } I_p \ll J_{rf}, I_r, I_z, \tag{2.27}$$

where b_p is the probe holder radius, λ_e is the electron mean free path, I_p is the probe current, I_r is the maximal current provided by the reference probe (equal to the ion current to the grounded chamber wall), and I_z is the current due to the generation of electrons in the plasma volume (electron flux with energy ε in the volume defined by the chamber characteristic size or by the electron relaxation length) [4]. Another inequality to consider is the ratio of the probe surface area A_p to the chamber wall area A_{ch}. This is because the wall-sheath resistance, especially at higher pressure, may not be negligible and can alter the I-V characteristic significantly near the plasma potential, distorting the low energy portion of the EEPF measurement. Figure 2.6 shows a typical probe measurement configuration in an inductively coupled plasma and its equivalent circuit, showing the wall sheath resistance as a part of the internal resistance [101]. To be able to neglect the wall sheath resistance, the following inequality must be satisfied:

$$(A_p n_c / A_{ch} n_s)(m_i / 2\pi m_e)^{1/2} \ll 1, \tag{2.28}$$

where n_c is the plasma density near the probe and n_s is the plasma density near the wall [4].

As figure 2.6 shows, the measured probe voltage consists of the probe bias as well as the noise components due to RVS, R_{ext} and R_{int}. These noises need to be compensated for accurate probe bias determination. R_{ext} can be accounted for using an analog circuit

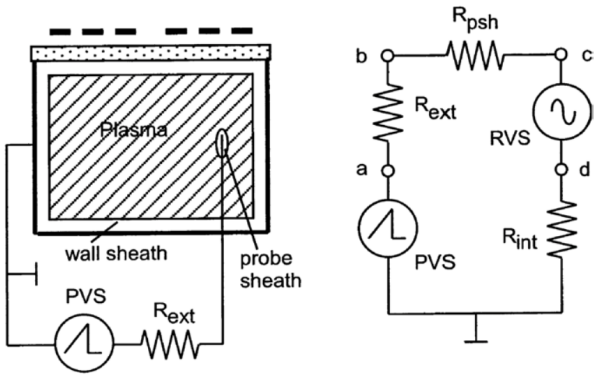

Figure 2.6: Typical probe measuring configuration in an inductively coupled plasma and its equivalent circuit. PVS is the probe voltage source, RVS is a noise voltage source (due to the plasma potential), R_{ext} is the external resistance, R_{psh} is the probe sheath resistance, and R_{int} is the internal resistance including the wall sheath resistance [101].

known as the gyrator [4]. To cancel out RVS and R_{int}, a differential approach is used as shown in figure 2.7, where MP is the main probe measuring the I-V characteristic and RP is a floating reference probe. The probe voltage driver takes the difference between the PVS signal and the RP signal, minimizing the noises due to RVS and R_{int} [101]. Still, this differential method alone is insufficient to cancel out the noises due to the plasma oscillations at the RF frequency because of the speed limitation of the electronics. To account for the plasma oscillations, a separate filter is installed into the probe circuit. The filter consists of subminiature inductors acting as RF chokes due to self-resonance at the RF frequency and its harmonics. A good filter needs to have large and sharp impedance peaks at the plasma driving frequency and its harmonics (usually at 13.56 MHz and 27.12 MHz). Chokes in the filter need to be carefully chosen and individually tested, since the self-resonance frequency depends on the inductor's intrinsic resistance and capacitance which maybe vary significantly from inductor to inductor.

Once an EEPF measurement is obtained, its accuracy can be determined by the sharpness of the I-V curve "knee" at the plasma potential. The plasma potential, sometimes called the inflection point, corresponds to the probe bias at the maximum of the first derivative and the zero point of the second derivative of the I-V characteristic. Ideally, the peak of the first derivative should occur sharply, such that the resulted second derivative has a maximum immediately after the zero point $\varepsilon = 0$. However, in reality, electrical

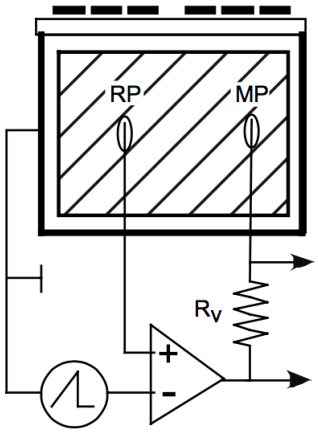

Figure 2.7: Differential driver circuit for noise cancellation in probe measurements. The reference probe (RP) signal feeds into the positive input and the measuring probe (MP) signal feeds into the negative input; the driver outputs the difference [101].

noises and probe contamination often lead to the broadening of the first derivative peak, and the second derivative maximum (also the EEPF maximum) occurs several eV units beyond $\varepsilon = 0$. The EEPF information in this region is then lost. A significant loss of information in this region is unacceptable, since a majority of the electrons are typically within the range of $\varepsilon = 0$ to $\varepsilon = T_e$. Generally speaking, the gap between $\varepsilon = 0$ and the EEPF maximum should not exceed $(0.3 - 0.5)T_e$ [4]. For most discharges, the electron temperature is in the range of $2 - 5$ eV. This limits the acceptable energy gap to $1 - 2.5$ eV.

Another factor that significantly reduces the accuracy of the EEPF measurements is the probe surface contamination. Often in chemically reactive plasmas and sometimes in noble gas plasmas, contaminants from residual gas or chamber wall deposit on the probe surface and form a thin dielectric film. This causes the work-function of the probe to drift, leading to hysteresis in the current-voltage characteristics and distortions in the EEPFs. The lower energy region of the EEPF is particularly vulnerable to such distortions [102]. To address this problem, Godyak developed a probe cleaning method which utilizes fast probe scanning cycles and automatic probe cleaning. Typical probe scan times are on the order of ms and a large bias voltage is applied between pulses of the scan voltage ramp to clean the probe surface via ion bombardment or electron current

heating. This approach was used to successfully obtain EEPF measurements in in low pressure chemically reactive plasmas where the film deposition rates were low (0.3 nm/s). For more details on improving the accuracy of the Langmuir probe measurements, please refer to the review paper by Godyak [4].

2.4.3 Langmuir Probe Measurements in Dusty Plasma

The main challenge in the Langmuir probe measurement in a dusty plasma is the probe surface contamination, as discussed in the previous subsection. The probe surface is contaminated when the dust particles deposit on the probe surface and form a dielectric film. In a dusty plasma, the rate of deposition is typically higher than that encountered in chemically reactive plasmas with low deposition rates. Particle films deposited on the probe surface can quickly grow to several 100s of nm in thickness. Because of this reason, Godyak's techniques alone are insufficient to address the probe contamination problem in the dusty plasma. As a result, in dusty plasmas the application of the Langmuir probe is often reduced to measuring basic plasma parameters such as the floating potential and the saturation current, from which rough estimates of the plasma density and the electron temperature can be made [17, 18, 23, 85, 103–107]. While some experimental attempts were made to measure the EEDF (electron energy distribution function) in dusty plasmas using an electrostatic energy analyzer [108], this approach has low precision compared to the Langmuir probe measurements. To address the contamination problem, the next chapter introduces a Langmuir probe equipped with a solenoid-actuated shield that exposes the MP wire to the dusty plasma momentarily and only during the probe current-voltage sweep. This method, combined with Godyak's fast pulsed scan and probe cleaning techniques, effectively minimizes probe contamination and allows reliable EEPF measurement in a dusty plasma for the first time.

Another concern worth discussing is the formation of a region devoid of dust particles around the negatively-biased probe. This has been investigated in the paper by Thomas Jr. [109]. It is possible to obtain reliable EEPFs in the dusty plasma in spite of the void

formation for two reasons. First, the dust particle frequency, $\sqrt{(Z^2e^2n_p)/(\epsilon_o m_p)}$ (where Z is the particle charge, n_p is the particle density and m_p is the particle mass) [110], is about 14 kHz for sub-micron sized particles in a typical low pressure CCP discharge. τ_p, the time scale during which particles can adjust to a change in electric field is about 0.07 ms (the inverse of the dust particle frequency), which is much shorter than the time it takes for a probe to complete a voltage sweep (on the order of ms). This means the void size will rapidly adjust to the probe voltage sweep, collapsing to very small sizes when the probe bias is small. The fact that probe coating occurs even if the probe is constantly scanning is an indication of this adjustment. Second, even when the void size is large, the electrons collected by the probe are still representative of the dusty region EEPF. This is because the void size, or the distance by which particles are repelled from the probe, is on the order of several Debye lengths; however, the electron energy relaxation length is much larger (on the order of several electron mean free paths) [111–113]. Because of this, electrons retain the information about the EEPF in the dusty region when entering the void region around the probe, and the dusty plasma EEPF can be obtained even if a dust-void region is present around the probe during the brief negatively biased part of the current-voltage sweep.

2.5 Capacitive Probe

The ion density can be measured using a capacitive probe, which consists of a planar tungsten probe connected in series to a 0.2 nF capacitor [114, 115]. The probe is placed inside the plasma and driven at a RF frequency. Since there is no direct current from the plasma to the ground through the probe, the probe maintains its floating potential by developing a DC bias, which then leads to the charging of the capacitor. fative charges on the plate adjacent to the plasma. The ion current then flows into the probe to discharge the capacitor in order for the probe to reach a new floating potential. The initial rate of the capacitor discharge is proportional to the ion flux. Assuming that the ion current is determined by the Bohm criterion, the ion density can be calculated from the ion flux and

the electron temperature (measured by the Langmuir probe):

$$n_i = \frac{C_p dV_c/dt}{A_p e\sqrt{eT_e/m_i}}, \tag{2.29}$$

where C_p is the probe capacitance, dV_c/dt is the discharge rate of the capacitor potential, and A_p is the capacitive probe area. This method is tolerant of dusty particle deposition on the probe surface, since the RF signal is able to travel through dielectric layers. The probe is usually driven at 1 MHz to avoid interference with the plasma potential oscillation at 13.56 MHz.

Caution needs to be taken when interpreting the capacitor discharge pattern. During the initial stage of the capacitor discharge, the probe bias is well below the plasma potential so dV_c/dt changes linearly with the ion flux. As the probe bias reaches the plasma potential, significant electron flux is able to reach the probe, and dV_c/dt is no longer a linear function of the ion flux. Therefore, only the initially linear potion of the discharge pattern should be considered in the ion flux calculation.

For reliable probe measurement, the probe sheath potential (proportional to the capacitor bias) should change slowly relative to the ion transit time across the sheath. The ion transit time is on the order of the ion plasma period:

$$\omega_{pi}^{-1} = (m_i \epsilon_o/(n_i e^2))^{1/2}. \tag{2.30}$$

Therefore dV_c/dt should satisfy that

$$dV_c/dt << \omega_{pi} kT_e/e. \tag{2.31}$$

Another phenomenon worth addressing is the dust particle's influence on the Bohm velocity. The Bohm velocity, as expressed in equation 2.5, is derived from the ion conservation of energy and flux, assuming Maxwellian electrons, cold ions, a collisionless sheath

free of ionizations and quasi-neutrality at the plasma-sheath interface [1]. Since these assumptions may not be true under more dynamic circumstances, efforts have been made to derive modified versions of the Bohm velocity [116–124]. A few of these studies involve the investigation of the Bohm velocity in dusty plasmas [125–128]. Among these, the paper by Liu discusses the modified Bohm velocity as a function of the dust size and density.

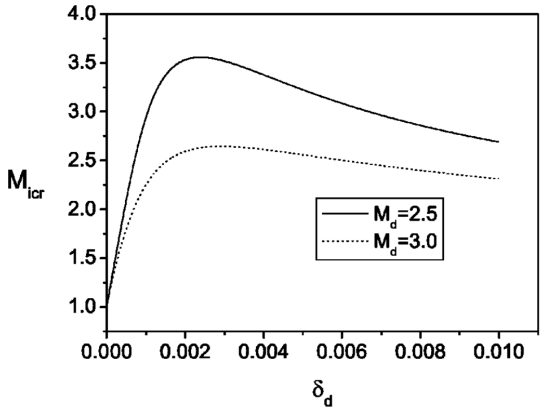

Figure 2.8: Ion critical Mach number M_{icr} as a function of δ_d, the ratio of the dust density to the electron density in an argon dusty plasma with $T_e = 1$ eV and dust size $a = 1\mu$m. M_d is the dust Mach number [128].

Specifically, Liu proposed an analytical model that addresses the changes in the ion sound velocity $c_{is} = \sqrt{T_e/m_i}$ in a plasma containing mobile dust particles with a uniform size distribution and negative charges due to the OML electron and ion flux. The main result is shown in figure 2.8, where M_{icr} is the ion critical Mach number and is equivalent to the ratio of the modified Bohm velocity to the original Bohm velocity, and δ_d is the ratio of the dust density to the electron density [128]. The graph shows that the dusty plasma Bohm velocity must exceed the original Bohm velocity due to the dust electrostatic drag force (DED) exerted on the ions by the dust particles. However, as the dust density exceeds a certain amount, DED decreases because the negative charges on each individual particle decreases due to the increased dust density. Two curves are plotted in figure 2.8: one for dust Mach number (the velocity at which the dust enters the sheath over the dust sound velocity) = 2.5 and the other for dust Mach number = 3.0. It was found that the change in the Bohm velocity is more signifiant for the smaller dust Mach number. This is because the larger the difference between the ion and the dust velocities, the larger the

DED. Overall, the modified Bohm velocity is within a factor of 2-4 of the original Bohm velocity.

Since the experimental conditions in the dissertation research is different from the more ideal conditions discussed in this model, it is reasonable to continue using the original form of the Bohm velocity to estimate the ion density, knowing that the ion density estimation should be accurate within a factor of 2-4. According to this model, the calculated ion densities corresponding to smaller dust densities and smaller dust sizes will have a higher accuracy.

2.6 Power Measurements

From a macroscopic point of view, a plasma is an electrical load connected to a power source. To ensure the efficient power delivery from the power source to the load, a matching network is required between the power source and the plasma. The amount of power delivered is always less than 100%: a certain portion of the applied power is reflected due to the imperfect impedance matching, and the other portion is dissipated in the matching network. This means P_d, the power that is actually dissipated in the plasma, is given by:

$$P_d = P_f - P_m, \tag{2.32}$$

where P_f is the total applied power (obtained by subtracting the reflected power from the forwarded power) and P_m is the power dissipated in the matching network.

P_f can be reliably determined by reading the in-line power meter at the power source (usually built into the power source equipment). P_m is often determined by comparing the values of P_f measured with the plasma and without the plasma while keeping the matcher resistance constant. The shortcoming of this method is it requires extinguishing the plasma whenever a measurement is performed. A more convenient method was developed by Godyak [129]. In this method, P_f values are again measured with and without the plasma, and the matcher conductance is kept constant under all cases by tuning a

variable capacitor in the matching network; this allows the determination of P_d without extinguishing the plasma during each measurement. Figure 2.9 shows a typical matcher and plasma circuit. The matcher is a π type network consisting of an input capacitance $C1$, an output capacitance $C2$, an inductance L_m, and a resistance R_m representing the matcher loss. The plasma discharge is modeled by the equivalent circuit consisting of a discharge capacitance C_d parallel to a discharge conductance G_d. The power source is attached to point 1 and the matcher connects to the discharge at point d. During all measurements, the matcher is tuned to the near-resonance condition (maximum forwarded power) by varying C_2. P_d then can be calculate from:

$$P_d = P_n - P_o(V_n/V_o)^2, \tag{2.33}$$

where P_n and V_n are the applied power and the electrode voltage measured with the discharge, and P_o and V_o are the applied power and the electrode voltage measured without the discharge.

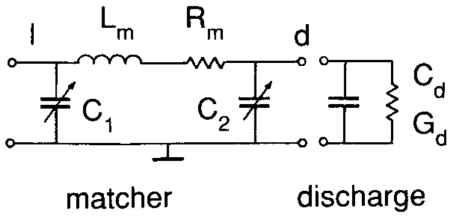

Figure 2.9: Typical matcher and capacitively-coupled plasma circuit. [129]

Chapter 3

Low Pressure Plasma Diagnostics: Experiment

Part of the content in this section has been published in *Journal of Physics D: Applied Physics* in 2015 [99].

3.1 System

Figure 3.1(a) shows a schematic of the capacitively coupled plasma reactor and the plasma diagnostics. The Langmuir and capacitive probes are inserted into the plasma chamber for EEPF and ion density measurements. A rotating TEM (transmission electron microscopy) grid holder is used for collecting nanoparticles at different times after the plasma has been initiated. The plasma is maintained between two circular 19.1 cm diameter aluminum showerhead electrodes separated by a 2.7 cm gap. Unless otherwise noted, all experiments were conducted at 80 mTorr in an argon-silane gas mixture: 4.7 sccm (standard cubic centimeters per minute) of 5% silane in argon flow diluted further with an additional 10 sccm of argon flow.

Each electrode has 97 1.5 mm diameter holes arranged in the pattern shown in figure 3.1(b). Gas is injected into the plasma through the showerhead holes and are pumped out through the holes in the lower electrode. The upper electrode is driven at 13.56 MHz

and the lower electrode is grounded. A Teflon insulator covers the top of the upper electrode to suppress parasitic discharges. The bottom electrode has a 2 mm hole in the center of the electrode for nanoparticle extraction. A TEM grid holder plate is placed below the bottom electrode in line with the 2 mm hole. The TEM grid holder is attached to a SMD210 PC-controlled stepper motor. When ready for particle collection, the stepper motor rotates the holder plate and aligns a TEM grid with the 2 mm diameter hole in the center of the bottom electrode, allowing collection of particles carried by the gas flow.

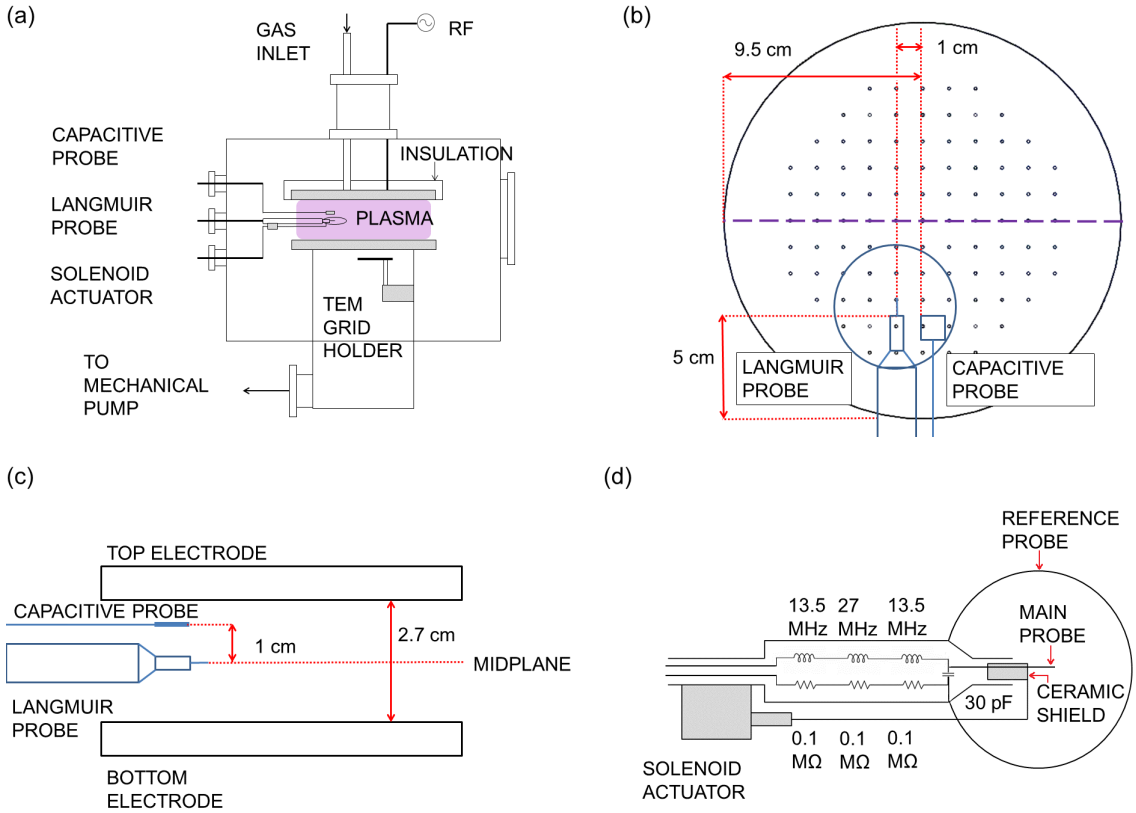

Figure 3.1: (a) A schematic of the capacitively coupled plasma reactor and the plasma diagnostics. (b) Top and (c) side views of the Langmuir and capacitive probes and their relative positions. (d) A schematic of the Langmuir probe electronic filter and the solenoid shield. Drawings are not to scale.

The capacitive probe, the Langmuir probe and the Langmuir probe shield are installed on three separate feedthroughs on one side of the plasma chamber. Figures 3.1(b) and 3.1(c) show the relative positions of the Langmuir probe and the capacitive probe. The

Langmuir probe is driven by the VGPS probe-diagnostic system® which allows for EEPF measurements using fast (on the order of 1 ms) voltage sweeps during which current-voltage characteristics are collected. Figure 3.2 shows the shape of the scanning voltage during each sweep. Each scan is 3 ms long with a negative-to-positive ramp followed by a positive-to-negative ramp. A −50 V bias (referenced to the probe floating potential) is applied between each ramp to clean the probe.

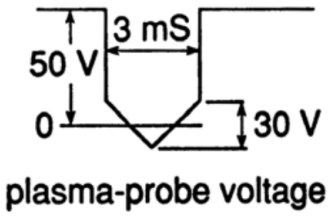

Figure 3.2: The Langmuir probe voltage ramp. Zero indicates the probe floating potential [4].

The Langmuir probe is specifically designed for EEPF measurements in a low pressure, weakly-ionized and isotropic plasma. Figure 3.1(d) shows the probe design and the electronic filter. The current collection probe is a 5 mm long wire surrounded by a ring-shaped reference probe. The reference probe has a large surface area relative to the main probe, and it acts both as the reference probe for RF noise suppression (see section 2.4.2) and as a shunting electrode that reduces the main probe's impedance relative to the plasma. Both the collection probe and the reference probe are made of 0.254 mm diameter tungsten wire. The reference probe loop diameter is 60 mm. The reference and the collection probes are connected to a two-channel RF filter comprised of three inductors self-resonating at 13.56 MHz and 27.12 MHz, three 0.1 MΩ resistors and a 30 pF capacitor arranged as shown in figure 3.1(d).

Fast current-voltage sweep and automatic cleaning techniques alone were found to be insufficient to effectively overcome probe surface contamination, especially when the plasma was turned off and dust particles were collected on the probe. To address this issue, the current collection probe is covered by a cylindrical ceramic shield controlled by a DC-powered solenoid actuator. The solenoid-actuated shield has an outer diameter of

3 mm and an inner diameter of 0.8 mm. When a $7 - 12$V DC voltage is applied, the solenoid actuator pulls the spring-loaded shield back and exposes the probe. When the DC voltage is turned off, the shield is pushed back by the spring force to cover the probe again. Probe contamination is minimized this way by keeping the probe covered with the shield except when acquiring the current-voltage characteristics using the fast voltage sweeps. The reference probe is not part of the current-collection circuit and therefore is not significantly affected by the contamination.

The 1.5 cm^2 planar capacitive probe is made of tungsten and is connected to a 0.2 nF capacitor. The probe is biased at 1 MHz, leading to the charging of the capacitor with electron current. The 1 MHz bias is periodically turned off and the ion current discharges the capacitor until the probe potential decays to the floating potential. The discharge rate is proportional to the ion flux [114, 115] which can be determined by monitoring the voltage drop across the capacitor using a Picoscope®. Assuming that the ion current is determined by the Bohm criterion, the ion density can be calculated from the ion flux and the the electron temperature (measured by the Langmuir probe).

The real power dissipated in the plasma is obtained by subtracting the power dissipated in the matching network from the total forward power from the RF power supply. This is done by measuring the electrode voltage and the forward power both with and without the plasma, while keeping the matching network at near-resonance condition by adjusting a variable capacitor in the matching network.

An *ex situ* laser scattering experiment was performed to monitor the particle size distribution over time with the Langmuir and capacitive probes inside the plasma. It was found that with the probes inserted, the time-evolving particle spatial distribution was absent: the dust particle spatial distribution was highly uniform and stayed uniform over the duration of the experiment (5 min).

3.2 Experiment Procedure

The above experiments were conducted in the following sequence.

1. EEPF and ion density were measured in a pristine argon plasma. This measurement is referred to as "initially pristine".

2. A plasma was initiated in an argon-silane mixture at the same pressure, during which silicon nanoparticles nucleated and grew. At designated times, the Langmuir probe current-voltage characteristics and the capacitive probe data were collected. The Langmuir and capacitive probe measurements were made separately and sequentially to prevent interference. There was approximately a 10 second delay between the Langmuir probe and the capacitive probe measurements.

3. After all dusty plasma measurements were completed, the plasma was turned off and all gas lines and the reactor were purged with argon.

4. Another pristine argon plasma was initiated at the same pressure and the EEPF was measured again. This measurement is referred to as "after purging".

In separate experiments, nanoparticles synthesized in the plasma were collected using the rotating TEM grid holder at predesignated times after plasma initiation. The pressure, power and gas flow rates were the same as those used during the probe measurements. During each experiment, nanoparticles were collected at a single designated time. Five experiments were conducted to collect nanoparticles formed at all designated times (30 s, 90 s, 150 s, 180 s, and 300 s after plasma initiation). Each of the five experiments was conducted in the following sequence. At the designated time, the PC-controlled stepper motor rotated and exposed a TEM grid for 10 seconds to the gas exiting the plasma through the 2 mm hole in the center of the bottom electrode. As soon as the TEM grid was aligned with the 2 mm hole, the plasma was turned off to detrap all dust particles. Finally, the reactor was purged and the TEM grid was retrieved.

Chapter 4

Low Pressure Plasma Diagnostics: Results

Part of the content in this section has been published in *Journal of Physics D: Applied Physics* in 2015 [99].

4.1 Data and Analysis

Figure 4.1 shows the EEPFs measured in a dusty plasma with and without the shield to protect the probe. In both cases, the probe was immersed in the dusty plasma for 420 s after plasma initiation. Without the shield the probe was exposed to the dusty plasma while constantly measuring EEPFs with repeated and rapid potential scans. During measurements with the shield, the probe was exposed for less than 6 s to the dusty plasma at 30 s, 120 s, 300 s and 420 s to measure the EEPF; the probe was otherwise shielded. Without the shield, the "after purging" EEPF differed significantly from the "initially pristine" EEPF, even though both measurements were conducted in a pristine argon plasma. This difference is due to probe surface contamination. When the shield was used, the "after purging" EEPF always matched the "initially pristine" EEPF, demonstrating the effectiveness of the shield in reducing probe surface contamination.

Figure 4.2(a) shows the temporal evolution of the EEPF in a dusty plasma. Dusty

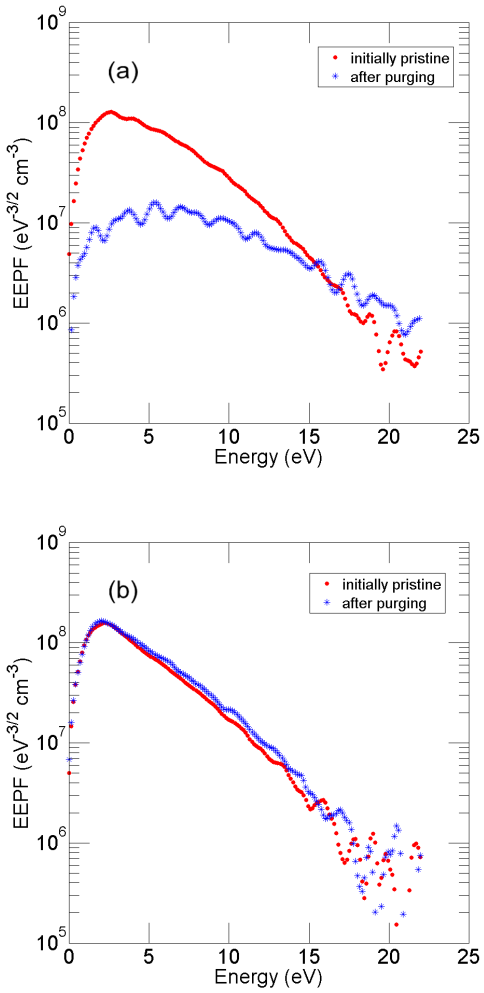

Figure 4.1: "initially pristine" and "after purging" EEPF measurements in 80 mTorr argon plasma maintained using 40 W of nominal RF power (a) without and (b) with the solenoid-actuated probe shield. In between the "initially pristine" and "after purging" measurements, an argon-silane dusty plasma was maintained at 80 mTorr and 40 W for 420 s.

plasma EEPFs were characterized by lower electron density and higher electron temperature. This finding agrees with the computer simulations by Denysenko *et al.* [46–49]. Interestingly, while the low energy portion of the EEPFs is increasingly depleted in the dusty plasma, the high energy tails of the EEPF at energies greater than 15 eV overlap throughout the experiment. This indicates that the ground state ionization rate of argon remains approximately constant (within a factor of two) while silicon nanoparticles nucleate and grow in the dusty plasma. For comparison purposes, figure 4.2(b) shows only the "initially pristine" EEPF and the EEPF obtained 30 s after dusty plasma initiation.

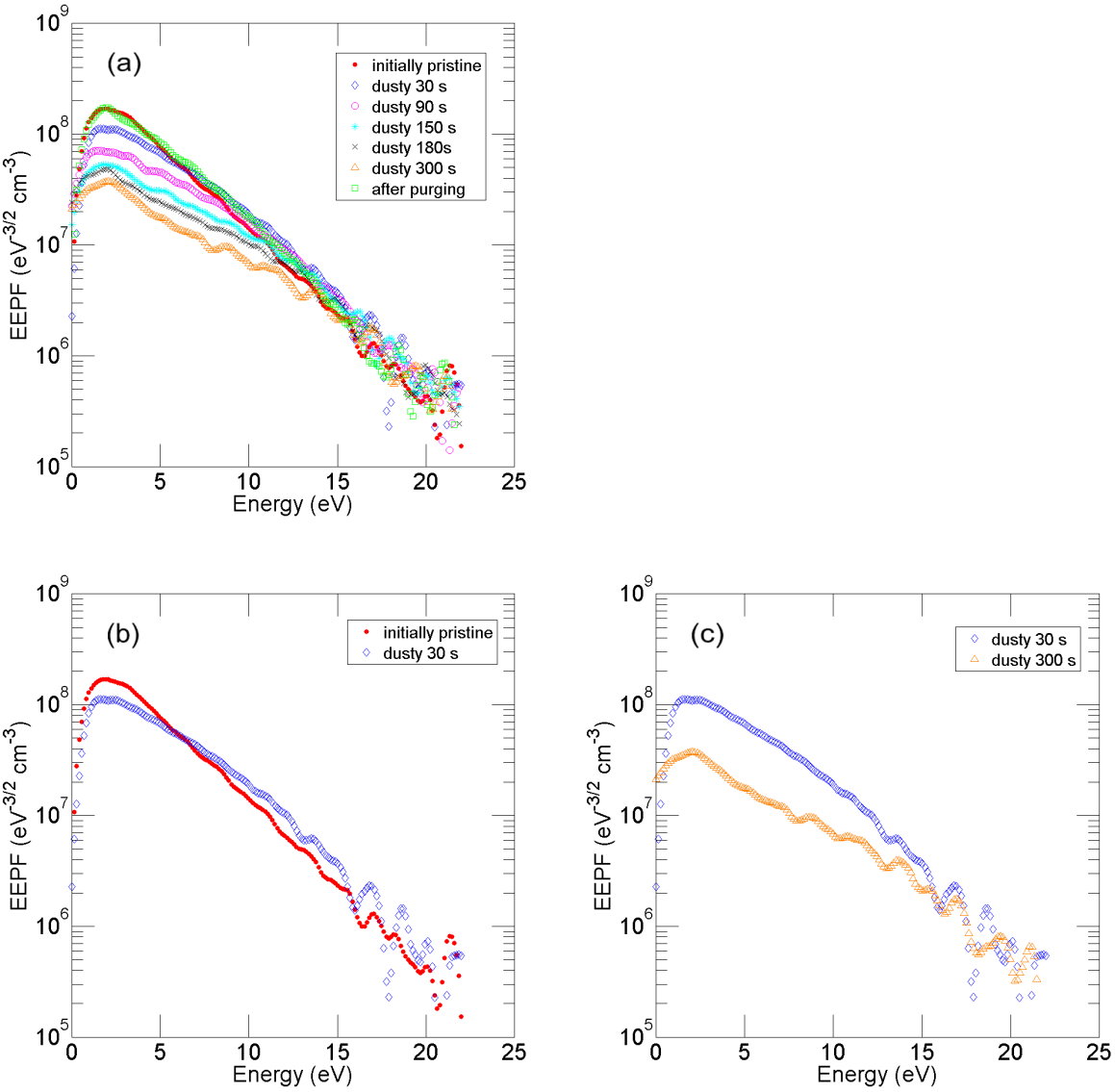

Figure 4.2: (a) Temporal evolution of the EEPF in a dusty argon-silane plasma maintained at 80 mTorr. The applied RF power was held constant at 40 W and the real power dissipated was 19.1 W in the "initially pristine" plasma, 28.5 W in dusty plasma, and 20.9 W in the "after purging" plasma. (b) EEPF in "Initially pristine" compared to EEPF in a dusty plasma 30 s after initiation. (c) Comparison of the EEPFs in a dusty plasma 30 s and 300 s after initiation.

Figure 4.2(c) shows only the EEPF obtained 30 s after dusty plasma initiation and the EEPF obtained 300 s after dusty plasma initiation. Figure 4.2(b) shows a decrease in the lower energy electron population and a slight increase in the higher energy population, consistent with increased electron temperature to increase the ionization rate [47]. Figure 4.2(c) shows the Maxwellization of the dusty plasma EEPF measured at 300 s

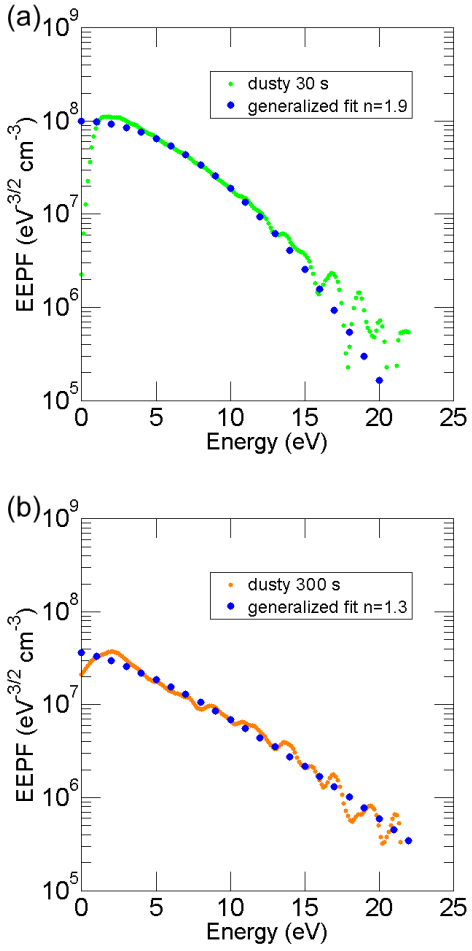

Figure 4.3: Dusty plasma EEPFs fitted with the generalized EEPF equation. (a) The EEPF measured at 30 s after dusty plasma initiation is Druyvesteyn-like ($n = 1.9$). (b) The EEPF measured at 300 s after dusty plasma initiation shows Maxwellization ($n = 1.3$).

compared to the Druyvesteyn-like EEPF measured at 30 s, demonstrating the significant loss of mid-energy range (4-10 eV) electrons to electron-particle collisions as dust particles grow in size, this finding is also consistent with the computer simulations by Denysenko, where the mid-energy range electrons are lost to mainly inelastic collisions with dust particles *et al.* [47]. To quantify the Maxwellization of the dusty 300 s EEPF compared to the dusty 30 s EEPF shown in figure 4.2(c), both EEPFs are fitted with a generalized EEPF, as shown in figure 4.3. As discussed in section 2.3, The generalized EEPF has the form $f_{p,generalized}(\epsilon) = c_1 \exp(-c_2 \epsilon^n)$ [47]; for a Maxwellian distribution, $n = 1$ and for a Druyvesteyn distribution, $n = 2$. The fitting gives $n = 1.9$ for the dusty 30 s EEPF and $n = 1.3$ for the dusty 300 s EEPF, showing that the 30 s dusty EEPF is more

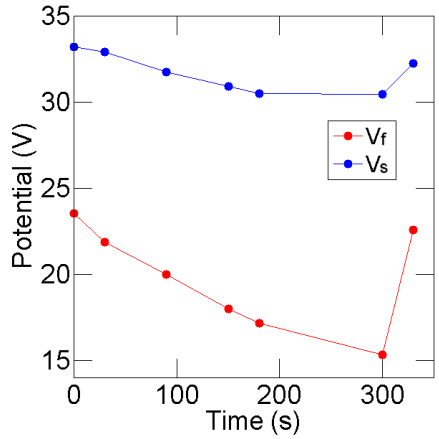

Figure 4.4: Plasma potential (V_s) and floating potential (V_f) as a function of time in a dusty plasma. The measurements at 0 s and 320 s correspond to the "initially pristine" plasma and the "after purging" plasma.

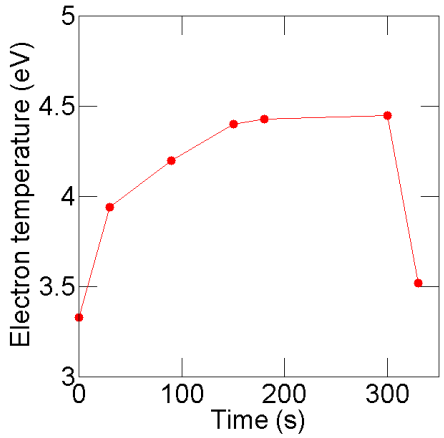

Figure 4.5: Electron temperature as a function of time in a dusty plasma. The measurements at 0 s and 320 s correspond to the "initially pristine" plasma and the "after purging" plasma.

Druyvesteyn-like and the 300 s EEPF is more Maxwellian-like.

Furthermore, while the applied RF power was held constant at 40 W, the true power dissipated in the plasma was 19.1 W in the "initially pristine" plasma, 28.5 W in the dusty plasma (measured at 300 s), and 20.9 W in the initiated "after purging" plasma. This is consistent with an increase in the electric field strength in the dusty plasma leading to higher electron temperature. Figure 4.4 shows that the plasma potential and the floating potential both decrease in the dusty plasma because the electron density decreases as electrons are depleted by the particles. The difference between the plasma potential

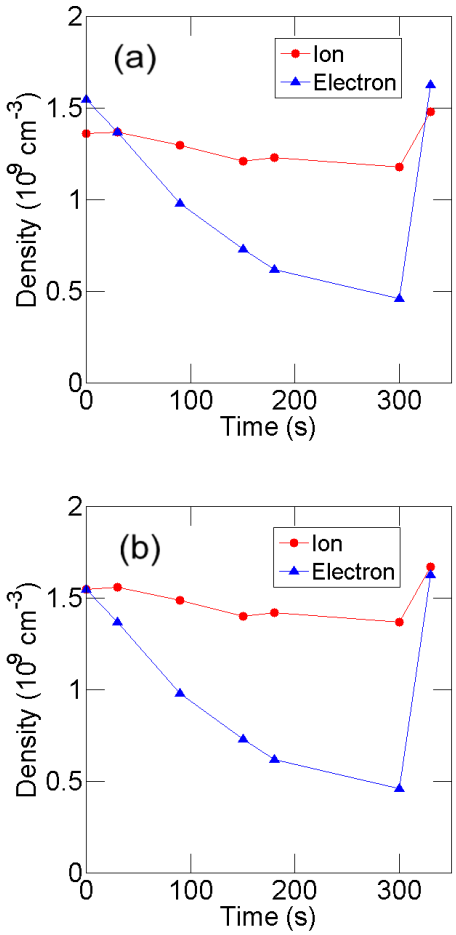

Figure 4.6: (a) Measured ion and electron densities in the dusty plasma. In both panels (a) and (b) the first and last data points at time = 0 s and time = 320 s correspond to the "initially pristine" and the "after purging" plasmas, respectively. (b) Scaled ion density by assuming the measured ion and electron densities are equal in the "initially pristine" argon plasma.

and the floating potential becomes larger, consistent with the increase in the electron temperature. Figure 4.5 shows the electron temperature in a dusty plasma as a function of time. As nanoparticles nucleate and grow in the plasma, the electron temperature rises from ≈ 3.3 eV for the pristine plasma up to ≈ 4.5 eV. This increase in the electron temperature is required to maintain a relatively constant (within a factor of two) ionization rate as the electron density decreases because of attachment losses to the nanoparticles.

Figure 4.6 shows the changes in the ion and the electron densities as a function of time in the dusty plasma. Figure 4.6(a) shows the electron density, as determined from the Langmuir probe using Eq. 2.18, and the ion densities determined independently from

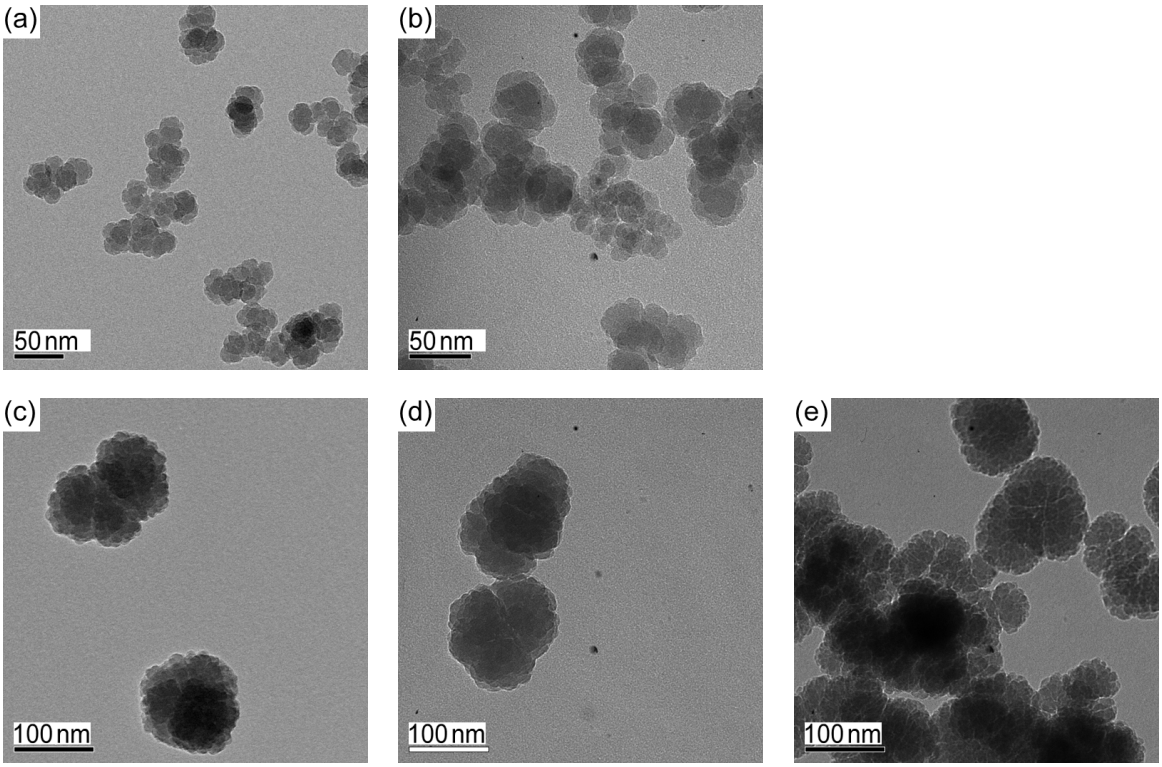

Figure 4.7: Dust (silicon nanoparticles) particles collected on TEM grids at designated times in 80 mTorr argon-silane dusty plasmas. (a) 30 s. (b) 90 s. (c) 150 s. (d) 180 s. (e) 300 s.

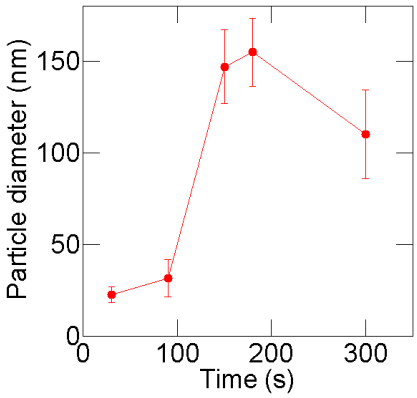

Figure 4.8: Estimated Average dust particle size in the argon-silane plasma as a function of time. Error bars correspond to the standard deviation of the particle size distribution.

the capacitive probe measurements. In the pristine plasma ($t = 0$), the electron and ion densities determined from these two different probes agree remarkably well and are within 15% of each other. Figure 4.6(b) shows the ion density scaled to be equal to the electron

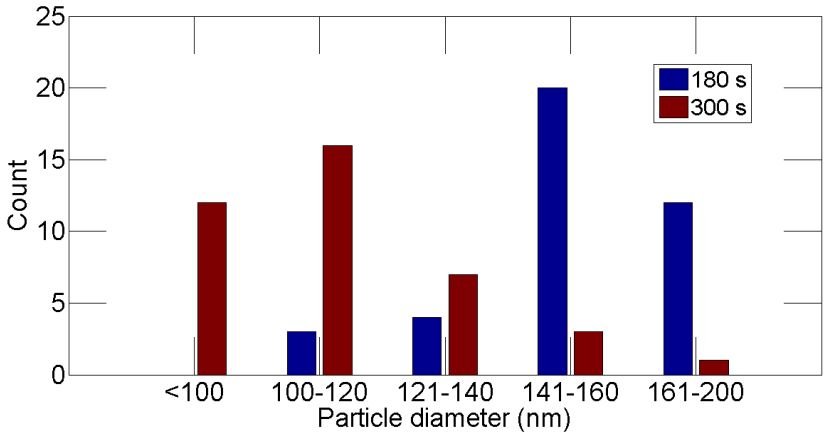

Figure 4.9: Size distributions of randomly selected particles collected at 180 s and 300 s after the dusty plasma initiation.

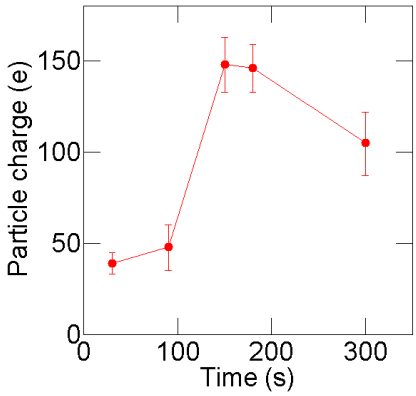

Figure 4.10: Estimated dust particle charge in the argon-silane plasma as a function of time.

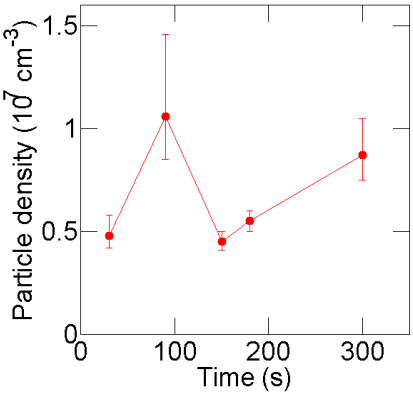

Figure 4.11: Estimated dust particle density in the argon-silane plasma as a function of time.

density in the pristine plasma. While the ion density decreases only slightly in the dusty plasma, the electron depletion is significant. The decrease in the electron density is due to attachment losses to the nanoparticles. After 300 seconds the electron-to-ion ratio is approximately 1/3.

Figure 4.7 shows TEM images of silicon nanoparticles collected at several different times from the argon-silane plasma at 80 mTorr. Figure 4.8 shows the average particle size as a function of time. The average nanoparticle size was determined by examining the particles collected on the TEM grid at each designated time. For each TEM grid, multiple TEM images were taken at different grid locations. Then from these images, 39 particles were randomly selected and measured to obtain the size distribution. Initially the particles grew rapidly in size, but the growth rate slowed after approximately 150 s. From 180 s to 300 s, the average particle size appeared to decrease but the particle size distribution widened as more small particles appeared to form while large particles (diameters greater than 120 nm) grew very little in size. Figure 4.9 shows the particle size distribution at 180 s compared to that of the 300 s. At 180 s, most of the samples have diameters larger than 140 nm while none had a diameter less than 100 nm. At 300 s, most of the samples have diameters less than 120 nm; only a few had diameters larger than 140 nm. This indicates most particles formed between 180 s and 300 s were small particles with diameters less than 120 nm.

Using the analytical model of particle charging developed by Gatti and Kortshagen discussed in section 2.2 [39], I estimated the dust particle charge using the ion-electron density difference and the average particle size. For small particles (diameter less than 1000 nm), assuming an OML electron current, equation 2.12 can be expanded and then simplified to:

$$\frac{n_i}{n_e}\sqrt{\frac{M}{\tau}}((1+\tau z)+\frac{16(\alpha z\tau)^3}{27Kn_a}+\frac{3\pi}{4\sqrt{2}}Kn_a\tau z[\exp(\frac{4\alpha z\tau}{3Kn_a}) -(1+\frac{4\alpha z\tau}{3Kn_a})])\exp(-\frac{4\alpha z\tau}{3Kn_a})\exp(z)=1. \tag{4.1}$$

Solving for z, the normalized particle potential and then for V_p, the particle charge Q_d

can subsequently be obtained from $Q_d = (4\pi\epsilon_0 a V_p)/(e)$.

It is worth pointing out that equation 4.1 is derived from equation 2.12 assuming an OML electron flux:

$$\Gamma_e = \pi a^2 n_e \sqrt{\frac{8kT_e}{\pi m_e}} \exp(\frac{eV_p}{kT_e}). \tag{4.2}$$

As figure 4.2(a) shows, the measured EEPFs, especially for the low dust concentration cases, are non-Maxwellian. Because of this, it is also possible to use the non-Maxwellian electron flux:

$$\Gamma_{e,non-Max} = \pi a^2 n_e \int_{-V_p}^{\infty} (1 + \frac{V_p}{\varepsilon}) \sqrt{\frac{2e\varepsilon}{m_e}} f_p(\varepsilon) \sqrt{\varepsilon} d\varepsilon, \tag{4.3}$$

where the integration accounts for the electrons with energies greater than the absolute value of the particle floating potential V_p [130]. This is because while electrons with energies below V_p are responsible for the particle charge, the current to the particle is determined by the electrons with energies higher than V_p since they are able to overcome the potential barrier due to the negative particle charge. Previous simulation study by Galli shows little difference in the calculated particle charge based on the Maxwellian and non-Maxwellian electron currents. EEPFs with similar effective electron temperature yield similar particle potentials and therefore charges [130]. This is especially true for the case of large particle size or high particle concentration where the EEPF shows Maxwellianization as illustrated in figure 4.3(b). The similarity arises from the fact that for low pressure plasmas, the non-Maxwellian EEPF and Maxwellian EEPF differ mainly in the high energy tail region; since the particle charge depends on the electrons with energies equal to or smaller than V_p, the differences in the high energy tail region have a negligible effect. Because of this reason, the Maxwellian expression is used in equation 4.1 for simplified calculation.

The results are plotted on figure 4.10, with error bars based on the standard deviations of the particle size. Figure 4.10 shows that the change in the particle charge correlates with the change in the particle size, first increasing rapidly and then decreasing significantly after 180 s as particle size distribution become less monodisperse. By comparing figures 4.8 and 4.10, it can be found that the particle charge is approximately given by one elementary

charge per nm of particle diameter.

The particle density n_p is calculated from $n_p = (n_i - n_e/Q_d)$ and plotted in figure 4.11. While no clear trend is apparent, it is interesting to note that the particle density is on the order of 10^7 cm^{-3}, which is about two orders of magnitude lower than the electron and ion densities in the dusty plasma, and the dust charge density is comparable to the ion charge density ($Q_d n_p \approx e n_i$).

4.2 Conclusion

In this part of the dissertation research, I demonstrated an experimental approach to achieve reliable EEPF measurements in a low pressure argon-silane dusty plasma using a shielded Langmuir probe to effectively minimize probe contamination. Compared to pristine argon plasmas the EEPFs in dusty argon plasmas are characterized by lower electron density and higher electron temperature accompanied by a drop in the low energy electron population. I also measured the ion densities using a capacitive probe. Using the electron and ion densities and the electron temperature derived from these two probes and the particle size information from the TEM measurements, I estimated the nanoparticle charge and density in the plasma. It was found that the particles have approximately one elementary charge per nanometer of diameter. The particle density was found to be two orders of magnitude below the electron and ion densities.

Chapter 5

Atmospheric Pressure Plasma: Background

5.1 Nanocrystal Heating and Charging at the Atmospheric Pressure

To design an atmospheric pressure plasma for nanocrystal synthesis, it is necessary to understand the key differences between the synthesis process at the low pressure and at the atmospheric pressure. In 2014 Kramer *et al.* developed a theoretical model of nanoparticle heating and charging over a wide range of pressure regimes ($10 - 10^5$ Pa). The model predicts the ion density, electron temperature and hydrogen density required to achieve sufficient heating to produce silicon nanocrystals of a particular size. Nanoparticle crystallinity is a function of the nanoparticle temperature. In the model, the nanoparticle temperature is calculated by solving a transient energy balance equation:

$$\frac{4}{3}\pi a^3 \rho C_{si} \frac{dT_p}{dt} = G_p - L_p, \tag{5.1}$$

where ρ is the silicon mass density, C_{si} is the heat capacity, T_p is the particle temperature, G_p is the heating rate (depends on the electron-ion recombination and the exothermic

hydrogen atom reactions on the particle surface), and L_p is the cooling rate due to conduction and convection [71]. The heating due to the electrons and ions is evaluated by calculating the electron and ion flux using the nanoparticle charging model discussed in section 2.2. The heating due to the hydrogen exothermic reactions, as well as the cooling due to the conduction and convection are simulated using Monte Carlo loops.

Kramer's model predicts that a higher ion density is required to form nanocrystals at the atmospheric pressure compared to lower pressures due to the rapid cooling of particles by collisions with background gas (the hydrogen density is held constant). It also predicts an increased nanoparticle agglomeration at the atmospheric pressure due to a reduced total negative particle charge. For 5 nm silicon nanocrystals, the model predicts that an ion density of 10^{13} cm^{-3} is required to achieve the nanoparticle temperature required for crystalization. These predictions are useful guidelines for designing the APGD reactor for nanocrystal synthesis.

5.2 Atmospheric Pressure Plasma Sources

5.2.1 Operation Regimes

Atmospheric pressure plasma refers to a wide range of plasma reactors operating under very difference regimes. Like their low pressure counter parts, atmospheric pressure plasmas operate in regimes roughly determined by two factors: the voltage-current (V-I) characteristic and the frequency. This section briefly reviews the available atmospheric pressure plasma sources, and discusses a few sources specifically suited for plasma-assisted nanocrystal synthesis.

The atmospheric pressure V-I characteristics is analogous to its low pressure DC counterpart, as shown in figure 5.1. To the left-most side of the graph is the background radiation region from A to B and the saturation region from B to C, where free electrons created by background radiation are swept from the cathode to the anode by the applied electric field, generating a weak current. This current then saturates since the number of

electrons created by the background radiation is limited. Applying an electrode voltage beyond the saturation region causes an ionization avalanche, leading to the rapid increase of the current. This region between point C and E is the Townsend or the dark discharge region. The discharge is invisible in this regime except for the corona discharges. When the breakdown voltage V_b is reached at point E, a significant number of secondary electrons are emitted from the cathode, and the discharge transitions into the normal glow discharge region from F to G and the discharge current increases rapidly. The path from F$'$ to D signifies the hysteresis in this region. The breakdown voltage depends on the Paschen's law, which will be discussed later. In the normal glow region, the voltage is independent of the current, since the current is allowed to increase by expanding the plasma coverage of the cathode area. When the entire cathode is covered by the plasma, further increasing the current requires increasing the voltage. This region of the positive V-I slope from point G to point H is the abnormal glow regime. Further biasing the electrode voltage beyond the abnormal glow regime causes significant electrode heating and thermionic secondary electron emission, which lead to the glow-to-arc transition (GAT) where the plasma changes from a non-thermal discharge to a thermal or arc discharge. In summary, just like the low pressure DC discharges, the atmospheric pressure plasmas can operate in these three distinct V-I regimes: the dark discharge region, the glow discharge region, and the arc discharge region.

Corona discharge is a very common form of atmospheric pressure plasma operating in the dark discharge region. These discharges are generated by high electric field surrounding sharp points. An interesting example is the St.Elmo's fire, a ghostly blue flame occasionally seen on ships named after St.Erasmus of Formia, the patron saint of sailors. The St.Elmo's fire is in fact a corona discharge generated around sharp points on ships (the masts) due to the strong electric field in the atmosphere created by thunderstorms. In modern days, corona discharge are widely used in industries for ozone production and sanitization. These commercial corona reactors are very robust and operate using low input power (< 1 kW). The disadvantages include low production rates and the difficulties in

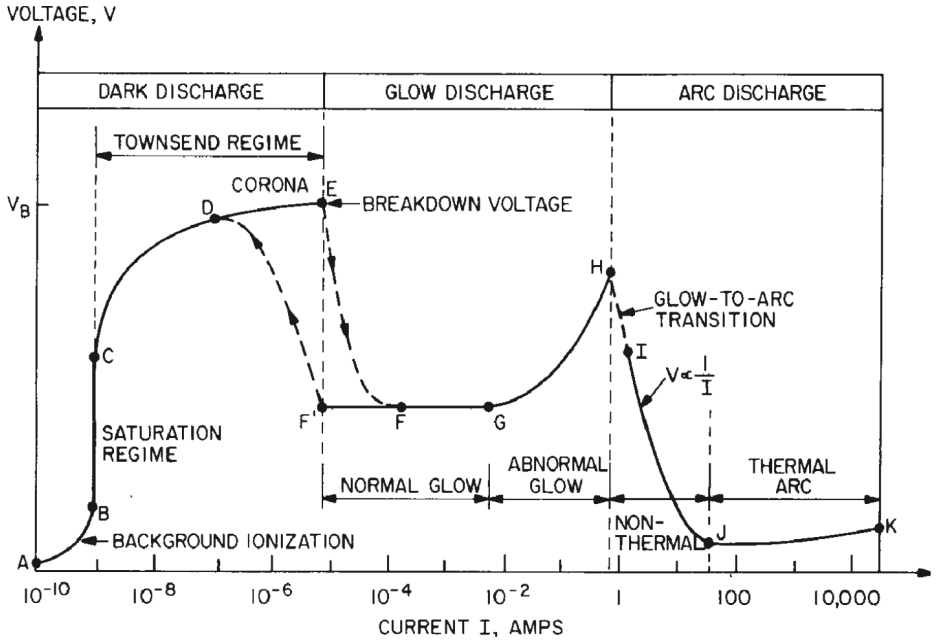

Figure 5.1: Typical voltage-current characteristic of a low pressure DC discharge [53].

controlling the flux of the active species since the discharge is highly non-uniform. Other applications of corona discharges include electrostatic precipitation, photon production, surface treatment and drag reduction, where corona discharges are used to reduce the thickness of the boundary layer of a flow past a flat surface [131, 132].

Atmospheric pressure plasmas operating in the arc discharge region are thermal discharges. An example would be the thermal plasma torch used for wielding, cutting, spraying, and occasionally material treatment and synthesis. The key difference between thermal plasmas and non-thermal plasmas is the neutral gas temperature. In non-thermal plasmas, the electron temperature is much higher compared to the gas temperature. In thermal plasmas, the electron and gas temperatures are equal due to the rapid collision between the two species. Typically for a non-thermal glow discharge, the electron temperature is as high as a few electron-volts while the gas temperature ranges between the room temperature up to 3000 K. For a typical arc plasma, however, the electrons and the gas have the same temperature, typically at 10,000 K [133]. At high pressures, the plasma tends to experience the GAT due to an increased electron-neutral collision rate, as shown in figure 5.2.

Atmospheric pressure plasmas also operate in different frequency regimes, as shown in figure 5.3. The low frequency region include the DC plasma, the pulsed DC plasma, and the plasmas operating in the kHz region. Since this frequency regime is below the electron and ion plasma frequency discussed in section 2.1, both electrons and ions are able to follow the applied field. Region 2 is the radio frequency region, where only the electrons are able to follow the applied field oscillation. Region 3 is the microwave region, where the behaviors in the RF region are enhanced. The choice of the frequency regime also determines the method of power delivery. For low frequency operations, the applied DC or AC power is delivered to the load (the discharge) with minimum reflection. At RF frequencies, a matching network is required to ensure the efficient delivery of the applied signal into the load; this is further discussed in section 5.4. In the microwave region, signals are easily absorbed or reflected and cannot be transmitted via cables; instead a wave applicator or a resonant cavity is used to deliver the microwave signal.

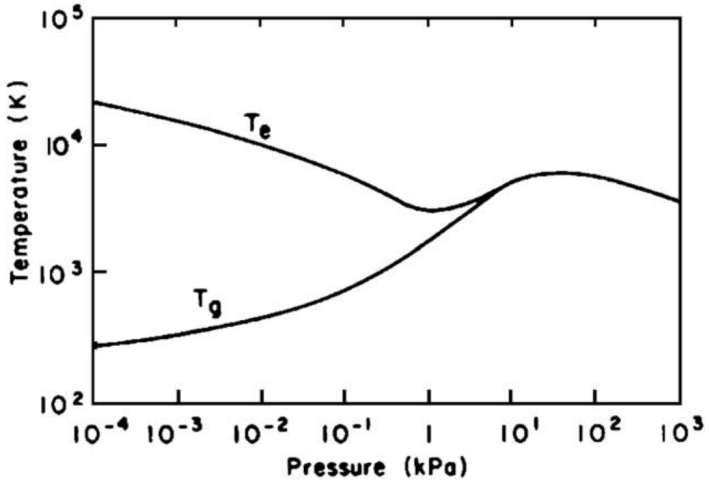

Figure 5.2: Electron and neutral gas temperatures as a function of pressure in a mercury plasma [134].

5.2.2 Atmospheric Pressure Glow Discharge

Plasmas operating in the glow discharge regime is preferred for nanoparticle synthesis due to its uniformity, stability and safety compared to corona discharges and thermal plasmas. Most nanoparticle-synthesizing atmospheric pressure glow plasmas today are

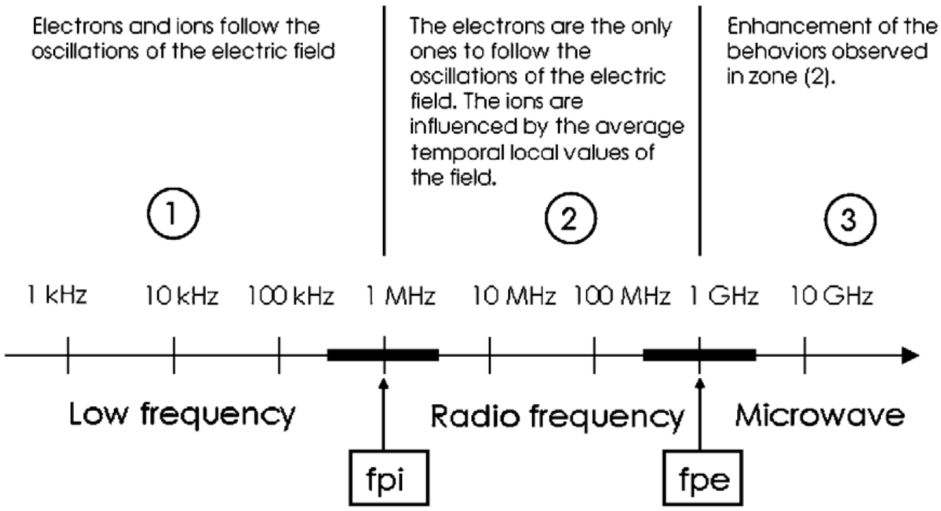

Figure 5.3: Electron and ion frequencies in non-thermal plasmas [133].

microplasmas [65–67, 79, 80, 135]. Microplasmas are plasmas with a characteristic length less than 1 mm. They are built this way to preserve the Pd scaling in Paschen's law, where P is the pressure and d is the gap spacing. Paschen's law is derived based on the total charge continuity in the vacuum breakdown of a DC discharge. It has the form:

$$V_b = \frac{B(Pd)}{\mathrm{Ln}A(Pd) - \mathrm{Ln}[\mathrm{Ln}(1 + 1/\gamma_{se})]}, \tag{5.2}$$

where V_b is the breakdown voltage, γ_{se} is the secondary electron emission coefficient of the cathode, and A and B are constants specific to the carrier gas and are often determined experimentally. By preserving the Pd scaling, microplasmas also preserve the favorable electrical properties of the low pressure plasmas while sacrificing its discharge volume by limiting the gap spacing to less than 1 mm. Mariotti and Sankaran have demonstrated theoretically and experimentally that microplasma reactors can maintain the non-thermal condition (electron temperature $\gg$ gas temperature) at high current densities [135, 136]. Because of this reason, microplasmas can achieve high electron and ion densities and produce nanocrystals smaller than 10 nm with very narrow size distributions [135]. In 2007, Nozaki *et al.* reported successfully producing tunable photoluminescent silicon nanocrystals less than 3 nm in size in an atmospheric pressure microplasma reactor. The

electron density in the reactor was as high as 10^{14} to 10^{15} cm^{-3} [66]. The disadvantages of microplasmas include the limited production quantity and the difficulty in scaling-up for industrial applications.

By looking at the Paschen's law and the V-I characteristic shown in figure 5.1, it seems that a large Pd value inevitably leads to a filamentary or an arc discharge. This is not true, for a uniform glow discharge can be generated in reactors with large Pd values by using unique designs and ignition techniques. Since Kanazawa *et al.* developed the first stable, large-volume and uniform atmospheric pressure glow discharge reactor in 1988, various reactor geometries and techniques have been utilized to ensure the stability and uniformity of such reactors [51–62]. The development of the large-volume non-thermal atmospheric pressure glow discharges (APGD) was facilitated by the research of atmospheric pressure gas lasers. Gas lasers typically have a large discharge volume (up to a few cm^3) and utilizes pre-ionization techniques to ensure uniformity over large volume [51]. Many gas laser reactor designs involve cylindrical geometries, these include the barrel reactor and the concentric cylinder reactor [131]. In a barrel reactor, a pair of ring or plate electrodes cover a glass tube in which the carrier gas flows through. In a concentric cylinder reactor, discharge is initiated in the gap between two concentric cylinder tubes, or between an electrode outside the cylinder and another electrode inside the cylinder. In 2006, Vons reported the production and coating of carbon nanoparticles in a non-thermal atmospheric pressure reactor utilizing the concentric cylinder geometry; the gap spacing was 1 mm [63]. The disadvantage of the cylindrical geometry is the difficulty in scaling-up. A larger reactor volume inevitably leads to a longer tube or a thicker dielectric barrier. A longer tube will change the particle residence time, and a thicker dielectric barrier leads to large current (up to a few A) followed by the necessity of water-cooling and / or using large flow rates to suppress the GAT, generating unwanted cost. Another other kind of APGD is the parallel plate reactor utilizing gap distances on the order of a few mm and currents on the order of 10 mA. Most parallel plate APGDs have at least one electrode covered by a dielectric barrier, while a few operate with bare electrodes [137]. Their operational

frequencies range from DC to RF [62]. Common carrier gases include helium, argon, and helium-argon mixtures. These parallel plate reactors, while relatively costly to build, are easier to scale-up compared to the concentric cylinder gas lasers. Scaling-up simply involves increasing the electrode area without changing the dielectric barrier thickness.

Properties of the APGD reactors have been vigorously studied over the past two decades [50–52, 62, 137–150]. Table 5.1 lists the typical RF APGD reactor parameters found in the literature [51, 52, 62, 137, 138, 140–144, 146, 151].

Carrier gas	Helium, argon, helium-argon mixture
Flow rate	≈ 10 slm
Frequency	13.56 MHz
Current density	$10 - 100$ mA cm^{-2}
Power density	$1 - 20$ W cm^{-3}
Electron temperature	$1 - 4$ eV
Gas temperature	<500 ^{o}C
Electron density	$\approx 10^{11}$ cm^{-3}
Dielectric barrier thickness	$0.5 - 0.7$ mm
Gap spacing	$1.6 - 5$ mm

Table 5.1: Typical RF APGD reactor parameters found in literature [51, 52, 62, 137, 138, 140–144, 146, 151].

The topic of nanoparticle synthesis using the APGDs is largely unexplored, in spite of the APGD's relatively simple setup and the possibilities of large-quantity production. To fill this knowledge gap, this dissertation presents an APGD reactor specifically designed for nanoparticle synthesis. Figure 5.4 shows the operation regime of the proposed APGD reactor. The reactor is a dielectric-barrier-discharge-like (DBD-like) discharge operating in the glow discharge regime under the RF driving frequency. It has a larger discharge volume compared to the microplasmas. Compared to gas lasers, it is cheaper to operate since it requires lower carrier gas flow rate and is free from the need of cooling water. There are three reasons for choosing the RF frequency. (1) RF operation is safer compared to microwave operations; (2) The rapidly oscillating RF field has an electron and ion trapping effect which limits the cathode heating and suppresses the GAT; (3) Compared to lower frequency operations, the RF frequency delivers the power more efficiently to the electrons.

Consider the electron power absorption in the plasma [131]:

$$\bar{P} = \frac{e^2 E^2}{2m_e} \times \frac{\nu_m}{\nu_m^2 + f^2}, \tag{5.3}$$

where $\bar{P}$ is the average power absorbed by the electron, E is the applied field strength and f is the applied field frequency. This expression indicates that the mean power absorbed by the electron is independent of the direction of the electric field. Therefore a high frequency source has a lower breakdown voltage, which is shown in figure 5.5. A lower breakdown voltage means the discharge is less prone to transition into an arc immediately after the breakdown.

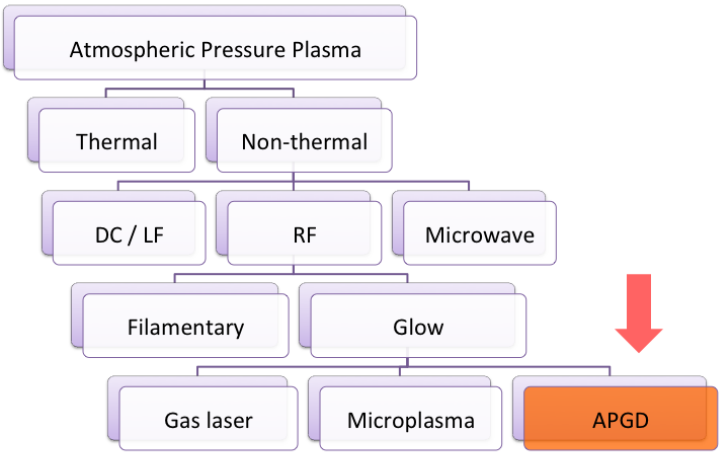

Figure 5.4: The target operation regime (highlighted) of the atmospheric pressure reactor for nanocrystal synthesis.

5.3 Discharge Uniformity at Large Volume

The key to producing an APGD is achieving discharge uniformity over large volume. Unlike low pressure discharges which can operate over a wide range of frequency and V-I regimes, APGDs can be obtained only by the careful selection of operation parameters and the implementation of proper reactor designs. In this section, I will highlight a few key design features that ensure the APGD uniformity.

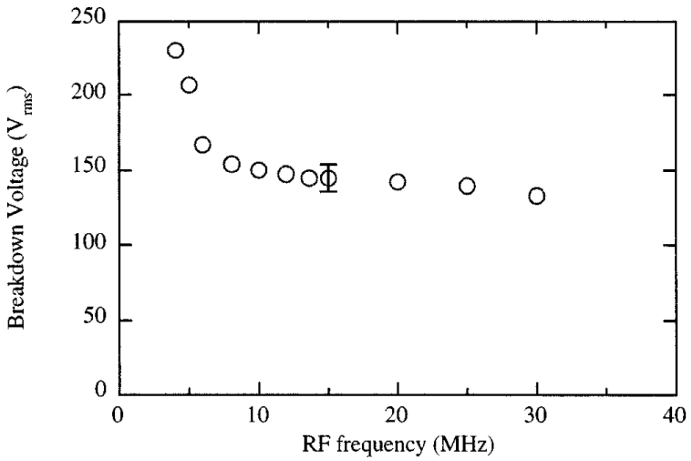

Figure 5.5: The breakdown voltage as function of frequency in a 600 Torr helium plasma with 0.16 cm gap spacing [147].

The use of the dielectric barrier is critical in APGDs since it suppresses the total current and limits the electrode heating [62]. Most APGDs, including the concentric cylinder gas lasers and the parallel plate reactors, are dielectric barrier discharges (DBD). During an AC cycle when the breakdown voltage is reached, an electron avalanche travels from the cathode to the anode. The electron avalanche is composed of a head of high-energy electron swarm followed by a positive tail of ions. When the avalanche reaches the dielectric barrier on the opposite electrode, the electrons spread out on the dielectric surface and leave behind a positive ion cloud. The negative charge built-up on the dielectric surface causes the local electric field to quickly collapse, terminating the current flow at that particular location [131, 152]. As a result, the conduction current in a DBD has a transient behavior as shown in figure 5.6. This behavior is often difficult to observe due to the large sinusoidal displacement current oscillation. In order to measure only the conduction current, the displacement current has to be subtracted from the total current. For low frequency discharges in the kHz range, the electron avalanches tend to form distinct microfilaments in the plasma, causing the discharge to be highly non-uniform. By fine-tuning the frequency, power density, gap spacing and the gas composition, the formation of these microfilaments can be suppressed and the DBD may be kept in the glow or the diffuse mode. This was done by Roth's group at the University of Tennessee to produce what they call the

OAUGDP^{TM}(one atmosphere uniform glow discharge plasma), an APGD operating in the normal glow regime. Specifically, the group defined a frequency regime for the generation of a normal glow APGD:

$$\frac{eV_{rms}}{\pi m_i \nu_{ni} d^2} \leq f \leq \frac{eV_{rms}}{\pi m_e \nu_m d^2}, \tag{5.4}$$

where V_{rms} is the rms driving voltage and ν_{ni} is the ion-neutral collision frequency. When this relation is satisfied, the applied field frequency (usually in the RF range) traps the ions within the gap spacing but does not trap the electrons. This reduces the cathode bombardment by the ions and therefore suppresses the GAT [53]. Similarly, an electron trapping mechanism that facilitates plasma uniformity is observed in RF discharges and is discussed in the papers by Liu and Shi [62, 153, 154].

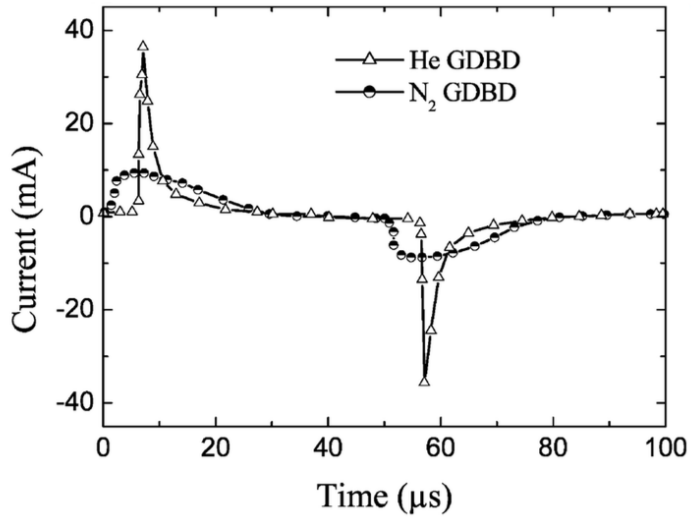

Figure 5.6: Current as a function of time in a kHz glow dielectric barrier discharge in helium and neon [155].

Another important factor in achieving APGD uniformity is pre-ionization—the degree of ionization in the plasma before each breakdown. To understand this, it is necessary to discuss the physics of the atmospheric pressure plasma breakdown. Low pressure plasmas typically experience the homogenous Townsend breakdown where the electron avalanches are independent of each other. The most basic form of the breakdown condition can be

expressed as:

$$\alpha d = \mathrm{Ln}(\frac{1}{\gamma_{se}} + 1), \tag{5.5}$$

where α is the Townsend ionization coefficient which gives the electron production per unit length [145]. This equation is used to derive the Paschen's law shown in equation 5.2. In plasmas with large Pd (such as the atmospheric pressure plasmas), the Townsend breakdown is not the likely mechanism. This is because the electron avalanches are able to grow into large sizes as they travel through the gap due to the high electron-neutral collision frequency (high P), the larger travel distance across the gap (high d), or the combined effect of both. These large avalanches contain large space charges and are no longer independent of each other. As a result, the avalanches form streamers (thin ionized channels) and cause a streamer (or spark) breakdown, which is often followed by a filamentary discharge or the GAT. Condition for the streamer formation is given by the Meek criterion, which equates the primary avalanche space charge field to the external field [145, 156]. Assuming the avalanche head radius is approximately $1/\alpha$, the streamer formation condition is given by:

$$\alpha(\frac{E}{P})d = \mathrm{Ln}(\frac{4\pi\epsilon_o E}{e\alpha^2}). \tag{5.6}$$

The streamer formation in the APGDs cannot be avoided by simply reducing the Pd value. Typically in a RF APGD, the Townsend breakdown is possible for Pd values only up to 10 Torr-cm [51]. Park reported that a helium RF APGD turned into an arc immediately after breakdown for Pd values above 240-270 Torr-cm [147]. Typical APGD reactors, including the proposed APGD reactor, have Pd values greater than 100 Torr-cm, and the streamer breakdown is indeed the more likely mechanism.

Fortunately, the streamer formation can be suppressed by pre-ionization techniques even when the Pd value is large. The concept is to prevent the primary avalanches from growing into streamers by having a large pre-ionization electron density (electrons present in the gap before each breakdown). Figure 5.7 and 5.8 illustrate this mechanism. During

a streamer breakdown as shown in figure 5.7, the primary electron avalanche initiates secondary avalanches by photoionization as it travels to the anode. Due to the strong space charge field within the primary avalanche (at a strength comparable to the applied external electric field), secondary avalanches converge to the primary avalanche, causing the primary avalanche to amplify and grow into a streamer [149]. When the streamer connects the electrodes, the plasma current can raise significantly leading to the glow to arc transition. If the plasma current is limited by the dielectric barriers, the streamers will lead to micro-discharge channels (filaments) distributed across the gap [145]. Figure 5.8 shows the case where sufficient pre-ionization electron density is achieved prior to the breakdown. These pre-ionization electrons ensure a large number of primary avalanches form at the beginning of each breakdown. These primary avalanches spatially overlap and their space charge field gradients are reduced. Consequently, secondary avalanches do not converge to the primary avalanches, and the streamer formation is suppressed [149]. Typically, a pre-ionization electron density higher than 10^6 to 10^7 cm^{-3} must be maintained prior to every discharge initiation in order to achieve this [149].

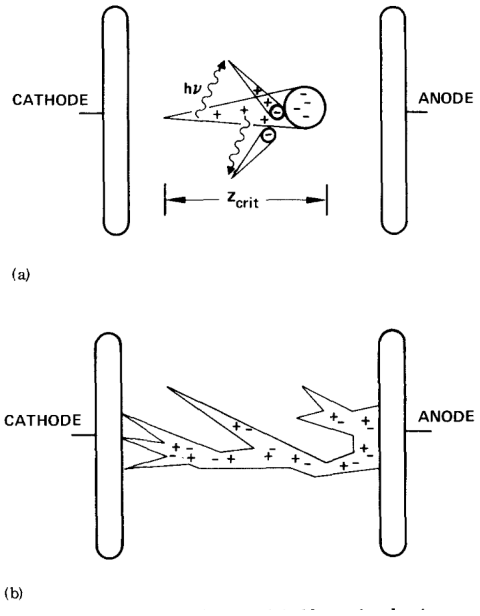

Figure 5.7: Streamer breakdown initiated by an electron avalanche. (a) Initial charge distribution. (b) Final charge distribution. z_{crit} is the distance which an individual avalanche must propagate in order to initiate the streamer breakdown [149].

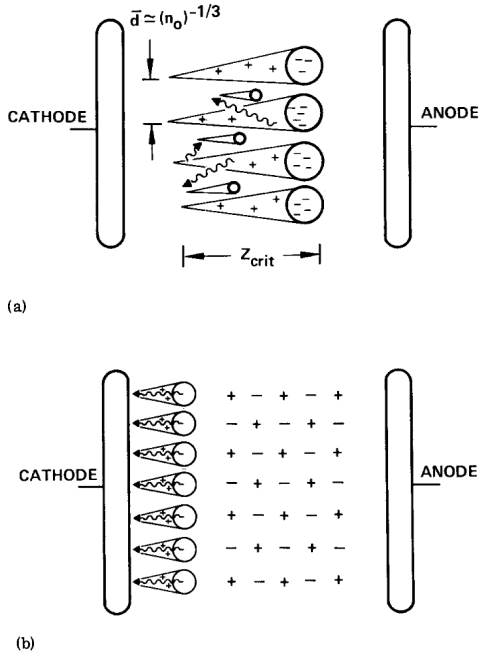

Figure 5.8: Breakdown initiated by multiple primary avalanches, where the formation of the streamers is suppressed by the pre-ionization. (a) Initial charge distribution. (b) Final charge distribution. n_o is the density of the primary avalanches [149].

Techniques for achieving high pre-ionization electron density include using high frequency fields (above 10 kHz), having dielectric barriers and encouraging gas impurities in helium discharges. Even trace amounts of impurity can significantly impact the electrical properties of helium APGDs. This is due to the increase of the effective ionization coefficient at low electric field through the Penning ionization by helium metastables [51, 148]. Another interesting technique is the tri-electrode (virtual cathode) reactor design, as shown in figure 5.9. This reactor contains three electrode: S is a metal electrode, G is a grid electrode, and T is an electrode covered by a dielectric barrier. Initially, a small discharge is initiated between G and S to create a pre-ionization electron population. Then utilizing the pre-ionization in the region, a large and uniform APGD is initiated between S and T [61].

Other interesting examples of atmospheric pressure uniform plasma designs include the gliding arc discharge and the transverse discharge. A gliding arc discharge is initiated between electrodes with a variable gap spacing. The discharge starts as an arc; then

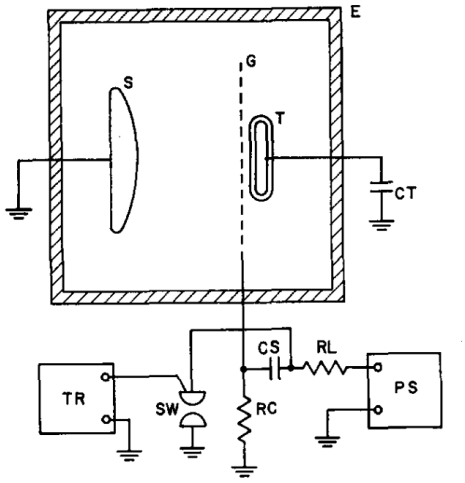

Figure 5.9: A tri-electrode atmospheric pressure uniform gas laser reactor utilizing the pre-ionization technique. E: container. S: shaped electrode. G: grid electrode. T: dielectric covered electrode. The discharge between G and T precedes the discharge beween S and G; this is controlled by the circuit below the reactor. CT: trigger capacitor. GS: energy storage capacitor. RL: current limiting resistor. RC: charging resistor. PS: high voltage DC power supply. SW: triggered spark gap. TR: trigger unit controlling the SW [61].

as the discharge travels toward the end of the electrodes with the larger gap spacing, it transitions into a non-thermal plasma due to a change in the surface area [158]. In the transverse discharge reactor design, the cathode region fluctuation (a primary cause of GAT) is suppressed by dividing the cathode into a number of pins, each ballasted with a large series resistor. As a result, current fluctuation in each pin is quenched by the voltage change across the resistor [159].

The carrier gas also has a significant influence on the discharge uniformity. Helium is normally used as the carrier gas in APGDs due to its low breakdown voltage and high uniformity maintained by the pre-ionization electron population generated by the helium metastables through Penning ionization [142–145, 150]. Figure 5.10 shows the Paschen curves for helium and argon discharges, where the helium curve shows a much lower breakdown voltage. The disadvantage of helium is its high cost, especially in atmospheric pressure reactors where the carrier gas flow rate is large. The argon carrier gas, or a mixture of helium and argon flow is preferable cost-wise. Because of this reason, the characteristics of helium, argon, and helium-argon mixture APGDs have been

investigated [141–144]. It was reported that compared to helium, argon discharge has approximately twice the electron density at the same applied power due to the argon atom's lower first excitation and ionization energy levels. On the other hand, argon discharge has lower electron temperature compared to helium discharge at the same current density [141, 143]. Moon *et al.* found that the addition of helium to an argon APGD lowered the discharge breakdown voltage and the gas temperature, but excessive helium addition resulted in the reduction of the discharge uniformity and the power coupling efficiency. They recommended an optimum mixing ratio of 30 to 50 percent helium in argon for an RF APGD with a power density up to 13 Wcm^{-3} and an argon flow rate of 10 slm [144].

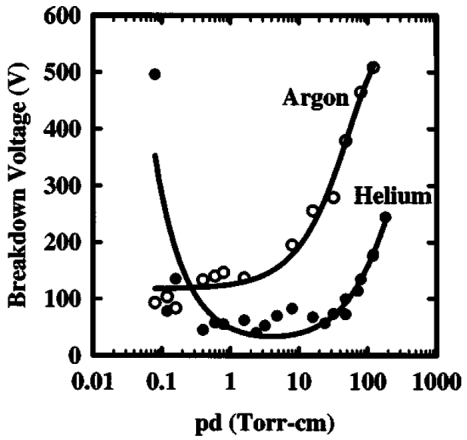

Figure 5.10: The Paschen curves for helium and argon RF discharges at the atmospheric pressure [143].

In summary, in order to achieve a uniform and stable APGD, appropriate designs have to be implemented, and important parameters need to be monitored. Some of these include maintaining a preionization electron density of 10^6 to 10^7 cm^{-3}, driving the discharge at the RF frequency, and choosing the appropriate carrier gas mixture.

5.4 Radio Frequency Matching

As discussed in the previous section, plasmas running at the RF frequency need to be connected to the power source through a matching network to ensure the efficient delivery of power. For low pressure plasmas, commercial matching networks are commonly used.

The atmospheric pressure plasma, however, involves much more instabilities compared to the low pressure plasmas, and the commercial matching networks are unable to adjust to these instabilities fast enough. Therefore it is usually necessary to build a custom matching network for the RF atmospheric pressure plasma. This section discusses the very basics of RF matching that applies to RF systems in general.

Without matching, the incident power from the power source to the load (plasma) is likely to be reflected rather than absorbed. This is because most commercial power sources are built to expect a load with the impedance $Z_L = 50 + 0j$, which means the load has $R = 50\Omega$ (the real part of the impedance, or resistance) and $X = 0$ (the imaginary part of the impedance, or the reactance). As the name suggests, the capacitively-coupled plasma has a non-zero reactance due to the capacitive component, and its impedance is not $50 + 0j$. By adding a matching network between the power source and the plasma, the total impedance of the plasma and the matching network will add to $Z_L = 50 + 0j$; that is, the load impedance Z_L as seen from the power source is now $50 + 0j$, and the system is said to be matched. Figure 5.11 illustrates the role of the matching network, where X1 and X2 are the serial and shunt components of the matching network, respectively.

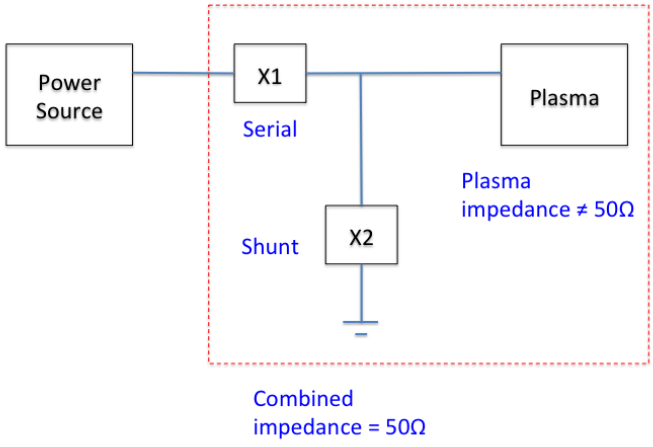

Figure 5.11: The role of the matching network in a RF plasma system.

The typical RF plasma matching network consists of a combination of up to four basic elements: the shunt capacitor, the shunt inductor, the parallel capacitor, and the parallel

inductor. Each element adds a component to the total impedance as shown in table 5.2, where L is the inductance, C is the capacitance, X_{norm} is the normalized reactance, B_{norm} is the normalized susceptance, and Z_o is the standard 50Ω resistance. For example, a system with a normalized impedance (normalized by a factor of Z_o) $Z_{L,norm} = 1 - 2j$ can be matched with a series inductor L. To solve for L, let $Z_{total,norm}$ be the total normalized impedance of the system and the matching network. Solving the equation $Z_{total,norm} = 1 = 1 + j(-2 + \frac{2\pi f L}{Z_o})$ yields $L = 15.9$ nH. Of course, this is a very simple example since the original system already has a 50Ω resistance and only requires a series inductor to cancel out the extra reactance. Real systems often have other resistance values and require more than one element to achieve the matching.

To match a real system, it is very convenient to use the Smith Chart, which can be found in any resource related to the field of RF and antenna engineering. The basic Smith Chart consists of circles of constant resistance and circles of constant reactance. The mirror image of the Smith Chart consists of circles of constant conductance and circles of constant susceptance. The center point of the Smith Chart corresponds to $Z_o + 0j$ (usually $50\Omega + 0j$), the desired matching condition. To use the Smith Chart, first mark the point corresponding to the plasma impedance. Then, using the Smith Chart path rules shown in table 5.2, choose the proper elements to move the system along the circles of constant resistance or constant conductance until the system reaches the Smith Chart center point. The path to the center point is not unique: it is possible to choose the most convenient combination of elements for building the physical matching network. In a real matching network the situation is not ideal: there are stray capacitances, stray inductances and contact resistances within and in-between the electrical components. While the Smith Chart provides a necessary reference, good matching in reality often involves trial-and-error. In addition, any voltage or current monitoring devices are considered part of the plasma system and need to be included in the matching network design. It is also desirable to have short transmission lines in the system, since long lines are considered matching elements and can shift the system along the constant voltage standing wave ratio (VSWR)

circles on the Smith chart. If long cables are required, it is necessary to choose the cables of the correct length for the particular driving frequency.

Finally I will briefly discuss the method for obtaining the plasma system impedance using an oscilloscope. First, measure the RMS voltage and current of the plasma and calculate the absolute value of the impedance by $Z_{abs} = V_{rms}/I_{rms}$. Next obtain the resistance and reactance by: $X = Z_{abs}\text{Sin}(\phi)$ and $R = Z_{abs}\text{Cos}(\phi)$ where ϕ is the phase angle between the voltage and the current (this needs to be measured carefully and compared to a calibration measurement where the load is a vacuum capacitor or a resistor). For capacitively-coupled plasma this angle should be negative. Finally the plasma system impedance, in the vector form, is given by $Z_L = R + Xj$.

Element	Normalized Impedance	Smith Chart Path
Series L	$+jX_{norm} = \frac{2\pi fL}{Z_o}$	Clock-wise along circles of constant resistance
Series C	$-jX_{norm} = \frac{1}{2\pi fCZ_o}$	Counter-clock-wise along circles of constant resistance
Shunt L	$-jB_{norm} = \frac{Z_o}{2\pi fL}$	Counter-clock-wise along circles of constant conductance
Shunt C	$+B_{norm} = 2\pi fCZ_o$	Clock-wise along circles of constant conductance

Table 5.2: Properties of the four basic elements in a RF plasma matching network.

5.5 Diagnostics

This section discusses the diagnostics methods used to measure the APGD plasma properties. These include the electron temperature and electron density measurements, the gas temperature measurement, and the plasma power measurement.

While for low pressure plasmas, the electron density and temperature can be obtained using a Langmuir probe, probe measurements are impractical for atmospheric pressure plasmas. This is because at the high pressure, the probe sheath is highly collisional and the probe dimension is too large compared to the electron mean free path; the accuracy requirements discussed in section 2.4.2 cannot be met. As a result, the electron density

and temperature in APGDs are often estimated using global plasma properties and zero-dimensional power balance models. Assuming the displacement current is small in the bulk plasma, the current density, $J_{rf,den}$, can be expressed as a function of the conduction current only:

$$J_{rf,den} = -n_e e \mu_e E_{bulk}, \tag{5.7}$$

where μ_e is the electron mobility and E_{bulk} is the electric field strength in the bulk region. Assuming the applied voltage is evenly distributed across the gap (that is, ignoring the difference between the sheath and the bulk electric fields), E_{bulk} can be estimated from $E_{bulk} = V/d$, where V is the electrode voltage [143, 146]. For better accuracy, E_{bulk} can be calculated by taking the sheath voltage and thickness into account. Collisional sheath thickness can be estimated from:

$$J_{rf,den} = 1.68\epsilon_o \sqrt{\frac{2e\lambda_i}{m_i}} \frac{V_{sheath}^{3/2}}{d_s^{5/2}}, \tag{5.8}$$

where d_s is the sheath thickness. From the sheath thickness, the sheath capacitance can be calculated:

$$C_s = 1.52 \frac{\epsilon_o A}{d_s}, \tag{5.9}$$

where C_s is the sheath capacitance and A is the electrode area. From this, the sheath voltage drop is:

$$V_{sheath} = \frac{J_{rf}}{2\pi f C_s}, \tag{5.10}$$

where V_{sheath} is the sheath voltage [1,143,146]. E_{bulk} can then be estimated by subtracting V_{sheath} from V and d_s from d. Similarly, the electron temperature can be estimated using a zero-dimensional power balance that equates the electron heating by RF fields to the electron energy lost due to electron-neutral collisions:

$$P_{in} = n_e \frac{P}{kT_g} k_1 I_1 + n_e (\frac{3}{2} kT_e - \frac{3}{2} kT_g) 2 \frac{m_e}{m_i} \nu_m, \tag{5.11}$$

where P_{in} is the power density, T_g is the neutral gas temperature, k_1 is the ionization

rate coefficient and I_1 is the first ionization energy of the carrier gas [143, 160, 161]. For a helium RF APGD, Moravej *et al.* found that inelastic collisions with excited species, recombination and radiative loss terms have little effect on the calculated T_e [143]. This is because the APGDs are usually weakly-ionized: densities of the excited states and the metastables are small compared to that of the ground states. The relevant constants used in equation 5.7 and 5.11 are found in the literature [1, 162–166]. During the particle synthesis process in the proposed reactor, trace amounts of the precursor gas (oxygen and diethylzinc (DEZ) diluted in helium) are added to the plasma. A portion of the input power will be dissipated in the precursors dissociation and excitation. Therefore equation 5.11 is used to estimate the electron temperatures in pristine plasmas but not in plasmas with precursors.

Unlike low pressure plasmas where the gas temperature is close to the room temperature, the APGD gas temperature can be a few hundred degrees and its effect is not negligible. Usually the gas temperature is measured optically. For example, Moon and Choe presented an optical method for measuring T_g in a helium-argon mixture RF APGD by analyzing the OH diatomic spectrum in the feed gas impurities [144, 167]. Optical measurements are non-invasive and have a wide measurable range. While acknowledging these advantages, the gas temperature in the proposed APGD reactor is measured directly using a thermocouple. This is because the reactor design allows a thin thermocouple wire to be physically inserted into the plasma through the gas exit. This is a low-cost and simple alternative to the optical characterization. However, this method does not allow *in situ* measurements, and most APGDs today still rely on the optical measurements to obtain the gas temperature.

The power dissipation measurement discussed in section 2.6 is inapplicable if the matching network does not contain a variable capacitor. This is possible for the case of APGD, since APGDs typically operate at higher electrode potential compared to low pressure plasmas, and high voltage variable capacitors in the correct capacitance range might not be commercially available. A more traditional method is used to determine

the plasma power in the APGD where the plasma is extinguished between each measurement. The detailed steps are: (1) With the plasma on, record the forwarded power and the electrode voltage; (2) With the plasma off, record the forwarded power at the same electrode voltage; (3) Subtract the forwarded power in (2) from the forwarded power in (1) to obtain the power dissipation in the plasma [1]. This method is valid as long as the power dissipation in the matching network is constant with and without the plasma. This can be verified by measuring the matcher coil temperature with and without the plasma.

It is also important to continuously monitor the plasma voltage-current characteristics in order to identify the plasma operation mode. Like their low pressure counterparts, APGDs operate in two distinct modes: the α mode characterized by stability, uniformity and volumetric ionization, and the γ mode characterized by secondary electron emission, thin sheath, and a high plasma power density. In a helium RF APGD, it was observed that the transition from the α mode to the γ mode was accompanied by the sheath breakdown followed by a 40% drop in voltage, 12% drop in current and an increase in power density from 25 Wcm^{-3} to 2083 Wcm^{-3} [138]. The γ mode is often unstable since intense ion flux from the sheath heats the cathode and causes the GAT [141, 146]. Therefore it is usually desirable to operate in the α mode. α mode and γ mode can be distinguished by monitoring the differential conductivity (dI/dV), which is positive for α mode and negative for γ mode as shown in figure 5.12 where region I is the α mode, region II is the α to γ transition mode, and region III is the γ mode [52,139]. The $\alpha-\gamma$ transitional phase can be identified by the relatively constant current-voltage phase angle as a function of the plasma current [139]. Physically, the α to γ transition occurs when the oscillation amplitude of plasma boundary exceeds half the total thickness of the sheath. Please see the paper by Vitruk for a detailed physical model of the α to γ transition in a RF discharge [168].

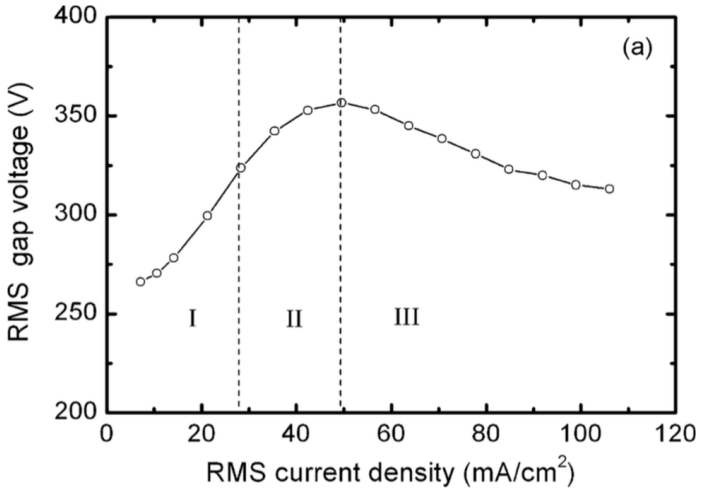

Figure 5.12: The voltage-current relationship in three glow modes in a RF atmospheric pressure glow discharge in helium [139].

5.6 Zinc Oxide Precursor

The precursors are chosen to be oxygen and diethylzinc (DEZ) for the production of zinc oxide nanocrystals. Zinc oxide is chosen over silicon due to its higher tendency to form crystals in the atmospheric pressure plasma. According to the atmospheric pressure nanoparticle heating model by Kramer, a much higher ion density is required for silicon nanoparticles to crystalize at the high pressure due to the rapid cooling by the neutral gas molecules [71]. In typical APGDs, the ion density is on the order of 10^{11} cm^{-3} as shown in table 5.1. This is insufficient for silicon nanocrystal formation according to the model. In contrast, zinc oxide nanoparticles produced by the DEZ-oxygen reaction crystalizes easily since the reaction is exothermic. A stoichiometry ratio of 7 oxygen : 1 DEZ is required for complete combustion.

As a material, ZnO has been extensively researched due to its applications in the ceramic, rubber, pharmaceutical and semiconductor industries. As semiconductors, ZnO nanocrystals are the building blocks for devices such as the transparent thin-film transistors, photodetectors and light-emitting devices due to its large and direct band gap, high electron mobility, high thermal conductivity and large excitation binding energy [169,170]. However, controlling the ZnO's electrical conductivity is a challenge. In 2014, Thimsen

et al. demonstrated a method for controlling the ZnO nanocrystal film resistivity by synthesizing ZnO nanocrystals in a low pressure plasma system, and then coating the film with a few nanometers of aluminum oxide using the atomic layer deposition technique. The aluminum oxide coating decreased the nanocrystal film resistivity by seven orders of magnitude. This supports the hypothesis that the OH contamination on the film surface acts as electron traps, which can be removed by the aluminum oxide coating to increase the nanocrystal film conductivity [171].

Chapter 6

Atmospheric Pressure Plasma: Experiment

6.1 System

Figure 6.1 shows the APGD reactor schematic. The reactor has a concentric cylinder geometry. The outer copper electrode is coil-shaped and is wrapped around a quartz tube functioning as the dielectric barrier, and the inner electrode is a grounded tungsten wire. In spite of the presence of the coil, the discharge is capacitive rather than inductive since the coil is floating at the RF potential. This capacitive nature is confirmed by the reactor's current-voltage waveform, where the current leads the voltage by $60-75$ degrees. The coil electrode can be replaced by a copper mesh at the same length to produce the same discharge, again confirming the capacitive nature of the discharge. For practical purposes, the coil electrode is preferred due to its rigorousness compared to the copper mesh. The quartz tube has an outer diameter of 7 mm and a thickness of 1 mm; the coil is 5.5 centimeters in length. The capacitive dielectric barrier discharge is generated between the electrodes using a 13.56 MHz RF source and a minimum of 3 slm (standard liters per minute) of helium or argon flow. The matching network is a single 7.3 μH coil. The discharge appears uniform when viewed by the eye, though at large power density (more than 35 W/cm^{-3}), local filament formation is visible in argon-oxygen discharges.

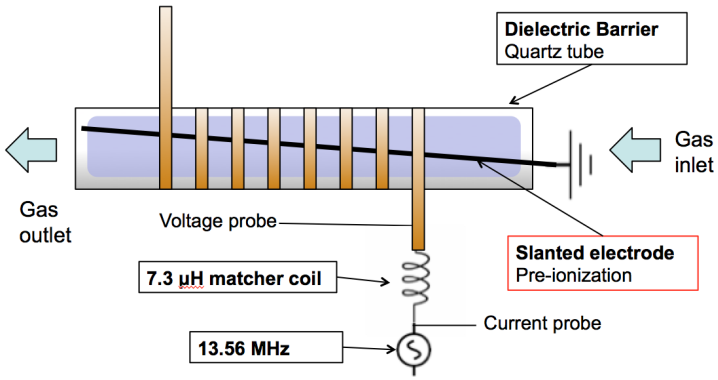

Figure 6.1: Schematic of the atmospheric pressure glow discharge reactor for nanocrystal synthesis.

As shown in figure 6.1, the center tungsten electrode is slanted such that the reactor gap spacing is non-uniform with an average gap spacing of 2.4 mm. This non-uniform gap spacing ensures the discharge uniformity by encouraging the production of the pre-ionization electron population discussed in the previous chapter. The mechanism is similar to that of the tri-electrode reactor discussed earlier: the discharge is first initiated in a local region where the gap spacing is minimum, then the discharge expands to fill the entire volume as the electrode voltage is increased. This way, the discharge remains uniform over a large volume. This could be due to the free electrons (and helium metastables in the case of a helium discharge) created by the initial discharge facilitating the formation of a uniform plasma downstream of the excited species, suppressing the streamer formation and the glow-to-arc transition.

Figure 6.2 shows the gas injection system. The reactor tube is attached to a three-way Swagelok® connector. The carrier gas (either argon or helium) is injected into the reactor through the bottom branch at large flow rates (on the order of slm). A separate stream of helium at low flow rate (on the order of sccm) is injected into a stainless steel bubbler containing the zinc precursor DEZ. The bubbling helium and the DEZ vapor then mix with the high flow rate carrier gas as they enter the reactor. Meanwhile through separate gas lines, a stream of oxygen at low flow rate (on the order of sccm) is injected into a small ceramic tube (3 mm outer diameter and 0.7 mm inner diameter), which is fed through the

three-way Swagelok® connector into the plasma. This way, oxygen is injected into the plasma without mixing with the DEZ. This is necessary to control the size distribution of the synthesized particles, since oxygen reacting with DEZ without the presence of the plasma results in large agglomerates on the order of micrometers. The actual DEZ flow rate Q_{dez} can be calculated from

$$Q_{dez} = Q_{bubble} * (P_v/P_c), \tag{6.1}$$

where Q_{bubble} is the bubbler gas flow rate, P_v is the vapor pressure of the DEZ, and P_c is the bubbler gas partial pressure, which is obtained from subtracting P_v from the pressure at the bubbler exit. Since the entire system is at the atmospheric pressure and Q_{bubble} is only on the order of sccm, the pressure at the bubbler exit is approximately equal to the atmospheric pressure. This give a 1.5 sccm DEZ flow for a 50 sccm bubbler gas flow.

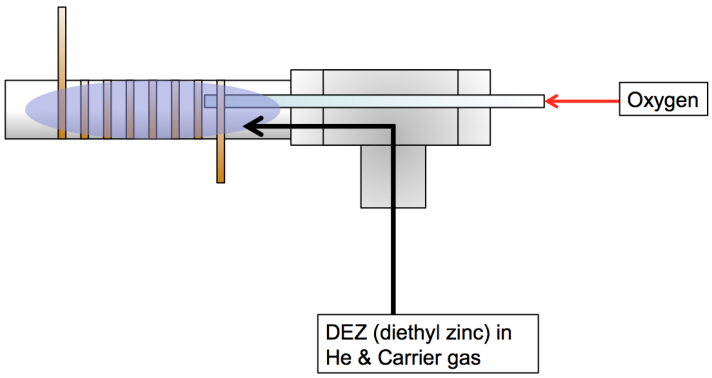

Figure 6.2: Gas injection system for the atmospheric pressure glow discharge reactor.

The diagnostics tools include a Tektronix® P6015A high voltage probe (bandwidth 75 MHz), a Pearson® current monitor (bandwidth 200 MHz), a Picoscope®, a substrate holder and a thermocouple. The high voltage probe measures the electrode voltage at the driven electrode, and a current monitor measures the current amplitude at the RF input. The dissipated power is measured using the method discussed in the last chapter. During the particle collection, a TEM grid or a substrate (2 cm × 2 cm silicon wafer) is mounted onto the substrate holder, which is positioned approximately 2 mm away from the tube opening to collect the synthesized nanoparticles carried by the carrier gas

flow. The 1 mm outer diameter thermocouple is inserted directly into the plasma through the tube opening for gas temperature measurement. This method is limited to *ex situ* temperature measurement, since the presence of the thermocouple during the particle collection disturbs the flow of particles from the reactor onto the TEM grid.

To investigate the effect of various plasma parameters on the particle morphology, it is necessary to control the neutral gas temperature independently of the power density and the residence time. This is done by immersing the reactor in a container filled with dry ice or insulating the reactor using styrofoam. At a 23 slm carrier gas flow rate and a 48 Wcm^{-3} power density, the dry ice lowers the neutral gas temperature by approximately 32^oC and the styrofoam insulator increases the temperature by about 80^oC.

6.2 Experiment Procedure

The experiment was conducted in the following sequence.

1. The system was purged using a 3 slm argon flow to clear the ZnO deposits and any residual DEZ liquid in the gas lines.

2. An argon-oxygen or helium-oxygen plasma was initiated in the APGD reactor.

3. The helium gas was injected into the bubbler to allow the DEZ vapor to be injected into the reactor.

4. The substrate holder was physically positioned in front of the tube opening to collect the nanoparticles carried by the gas flow.

5. During the collection, the Picoscope® recorded the current-voltage characteristics and the operator recorded the forwarded and reflected power.

6. After the collection, the substrate holder was physically moved away from the tube opening. The operator then shut down the precursor gas flow, the carrier gas flow, and then the plasma.

7. Without the plasma, the electrode voltage was adjusted to match the voltage during the collection. The current-voltage waveform, the forwarded power and the reflected power were again recorded.

8. A plasma was initiated under the same conditions as the nanoparticle synthesis plasma. The thermocouple was inserted into the plasma to measure its temperature.

Chapter 7

Atmospheric Pressure Plasma: Results

Part of the content in this section has been submitted to *Journal of Applied Physics* in March 2016 for consideration for publication.

7.1 Data and Analysis

Figure 7.1(a) shows the voltage-current characteristic of the APGD reactor under various carrier gas compositions: (1) 3 slm of helium, (2) 3 slm of argon, (3) 3 slm of helium and 20 sccm of oxygen, and (4) 3 slm of argon and 20 sccm of oxygen. For all cases, the voltage-current characteristic shows a positive slope, indicating that the discharge operates in the α mode. Figure 7.1(b) shows the electron density as a function of the power density with and without the precursor flow. The electron densities are slightly higher for the case without the precursor flow, showing that a portion of the applied power is dissipated in precursor dissociation and excitation. The difference between the electron densities (calculated using equation 5.7) is low for low power densities. Figure 7.1(c) shows the gas temperature as a function of the power density, and figure 7.1(d) shows the gas temperature as a function of the carrier gas flow rate for both a 3 slm argon plasma and a 3 slm argon plasma with 20 sccm oxygen impurity; the power density was held

between 20 and 23 Wcm^{-3}. Figure 7.1(d) illustrates that adding the oxygen impurity results in little difference in the gas temperature. The electron temperatures, calculated using equation 5.11, are approximately 2 eV in pristine plasmas.

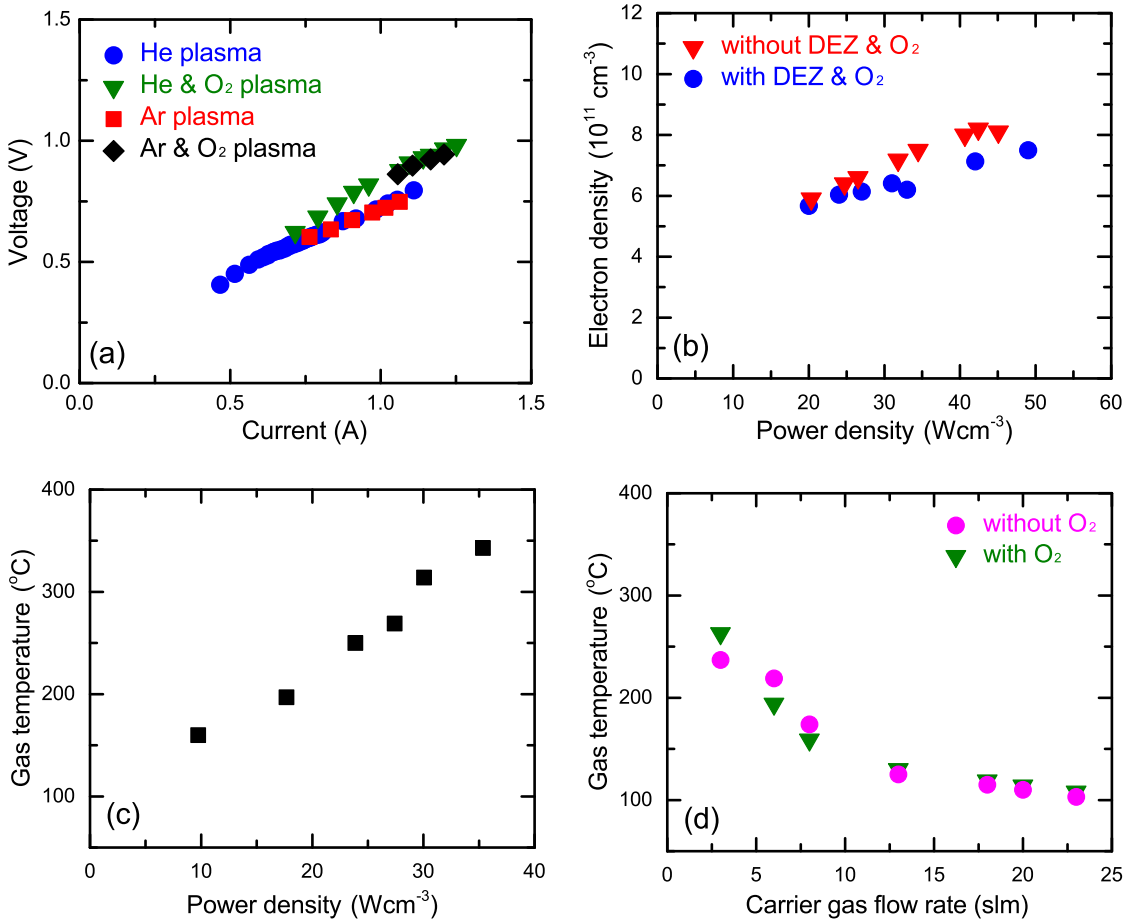

Figure 7.1: Electrical and thermal properties of the APGD tube reactor. (a) Voltage-current characteristics; the displayed voltage and current values are amplitudes. (b) Electron density vs. power density in a 23 slm argon plasma. (c) Gas temperature vs. power density in a 3 slm argon plasma with 20 sccm oxygen impurity. (d) Gas temperature vs. carrier gas flow rate in a 3 slm argon plasma with and without the 20 sccm oxygen impurity; the power density was held between 20 and 23 Wcm^{-3}.

Figure 7.6 shows the TEM images of typical ZnO particles synthesized using the APGD tube reactor. Depending on the reactor parameters, four types of particles are produced: (1) relatively mono-disperse spherical particles with diameters of 20 nm or less (figure 7.2(a)); (2) a mixture of spherical and nonspherical particles with diameters of 20 nm or less (figure 7.2(b)); (3) mainly nonspherical particles with diameters of 20 nm

or less (figure 7.2(c)); and (4) mainly high-aspect-ratio nonspherical platelets with diameters larger than 20 nm (figure 7.2(d)). Large particles tend to be nonspherical rather than spherical, indicating that the growth along the faceted surface is energetically favorable.Figure 7.3 shows tilted TEM images of the large particles shown in figure 7.2(d). The right image is tiled by 19 degrees relative to the left one. The rod-shaped object in the left image turns into a platelet in the right image after the tilt, demonstrating that the large particles are indeed platelets rather than rods. The large particles shown in figure 7.2(d) appear only occasionally: they were synthesized 4 out of 7 times under the same reactor condition. One speculation is that the formation of the large platelets (growth along the faceted surface) is influenced by the level of carbon impurity in the DEZ precursor. Since the system operates without a pump and is exposed to the ambient atmosphere during the operation, a small amount of ambient air can gradually leak into the DEZ bubbler, resulting in a varying amount of carbon impurities in the DEZ precursor over time. This could contribute to the variations in the synthesized particle morphology. Figure 7.4 shows the X-ray diffraction measurement of a typical sample made using the APGD tube reactor. The sample shows strong crystalline peaks which indicate that the average crystalite size is about 11 nm.

Condition	Carrier gas flow rate	Oxygen flow rate	DEZ flow rate	Power density	Deposition rate
no plasma	3 slm	50 sccm	1.5 sccm	NA	4 nm/s
argon plasma	3 slm	50 sccm	1.5 sccm	24 Wcm^{-3}	100 nm/s
argon plasma	23 slm	20 sccm	0.6 sccm	24 Wcm^{-3}	0.3 nm/s
argon plasma	23 slm	20 sccm	0.6 sccm	34 Wcm^{-3}	3 nm/s
argon plasma	23 slm	50 sccm	1.5 sccm	25 Wcm^{-3}	0.9 nm/s
argon plasma	23 slm	50 sccm	1.5 sccm	34 Wcm^{-3}	5.4 nm/s
argon plasma	23 slm	50 sccm	1.5 sccm	41 Wcm^{-3}	11 nm/s

Table 7.1: ZnO nanoparticle deposition rate for various reactor conditions.

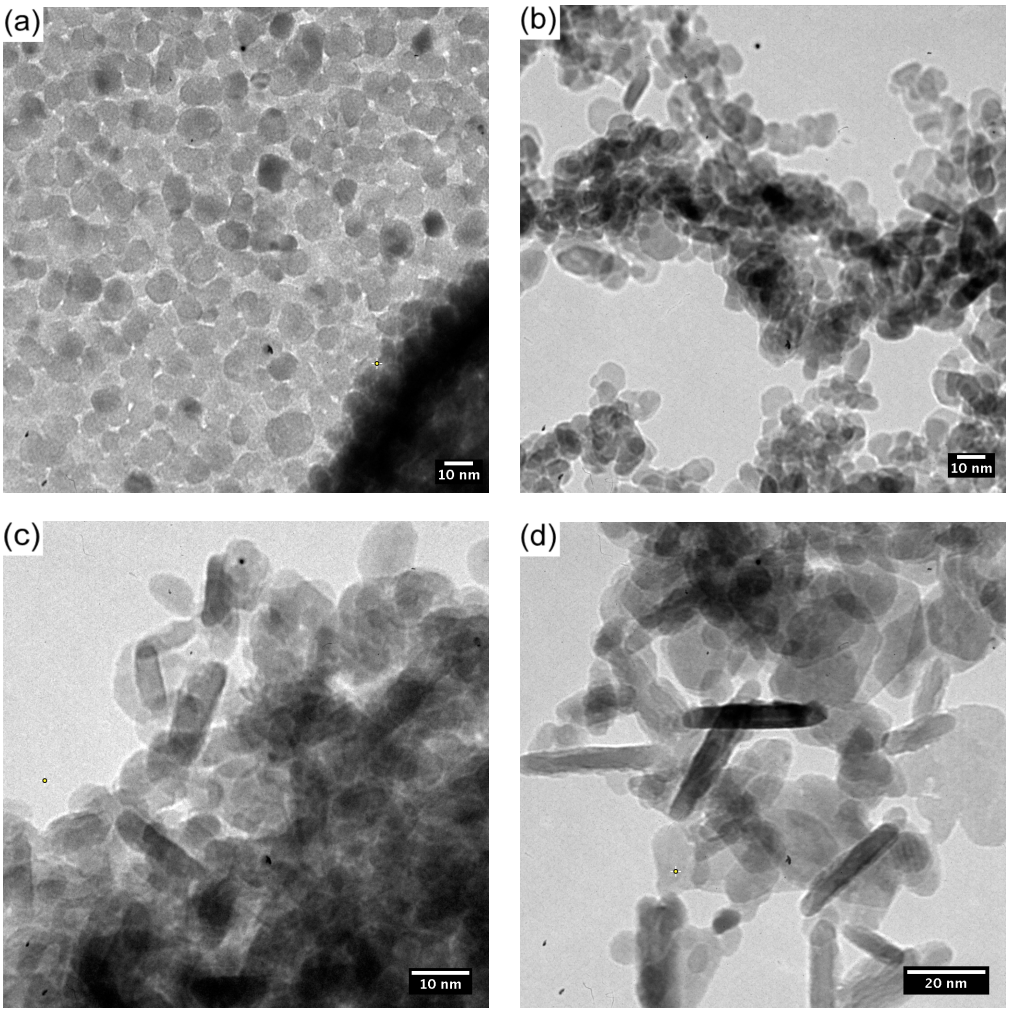

Figure 7.2: Four kinds of ZnO nanoparticles made using the APGD tube reactor. (a) Relatively mono-disperse spheres made in an argon plasma with a 23 slm carrier gas flow, 20 sccm of oxygen flow, 0.6 sccm of DEZ flow, and a power density of 61 Wcm^{-3}. (b) A mixture of spherical and nonspherical particles made in an argon plasma with a 23 slm carrier gas flow, 13 sccm of oxygen flow, 0.6 sccm of DEZ flow, and a power density of 23 Wcm^{-3}. (c) Mainly nonspherical particles made in a helium plasma with 13 slm of carrier gas flow, 20 sccm of oxygen flow, 0.6 sccm of DEZ flow, and a power density of 39 Wcm^{-3}. (d) Mainly large platelets formed occasionally in an argon plasma with a 23 slm of carrier gas flow, 20 sccm of oxygen flow, 0.6 sccm of DEZ flow, and a power density of 49 Wcm^{-3}.

The presence of the plasma greatly improves the particle size distribution and the production rate. Without the plasma, the oxygen-DEZ reaction produces large amounts of ZnO agglomerates ranging from a few hundred nanometers up to a micrometer in size, as shown in figure 7.5. When the plasma is present, the synthesized particles are negatively charged so that agglomeration is suppressed. As shown in table 7.1, the presence of

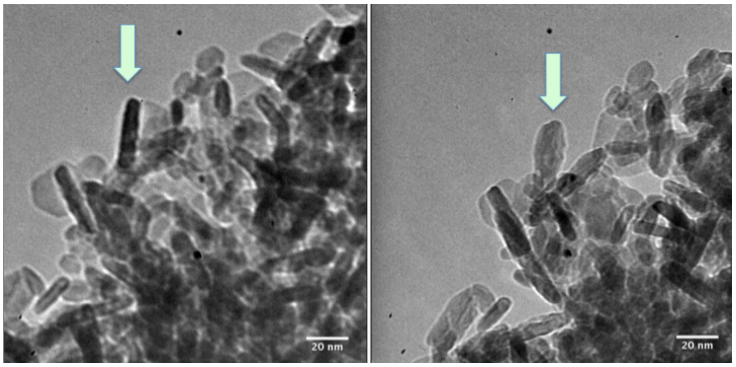

Figure 7.3: Tilted TEM images of the large particles shown in figure 7.2(d). The right images is tiled by 19 degrees relative to the left one, showing that the rod-shaped object is the side-view of a platelet-shaped particle.

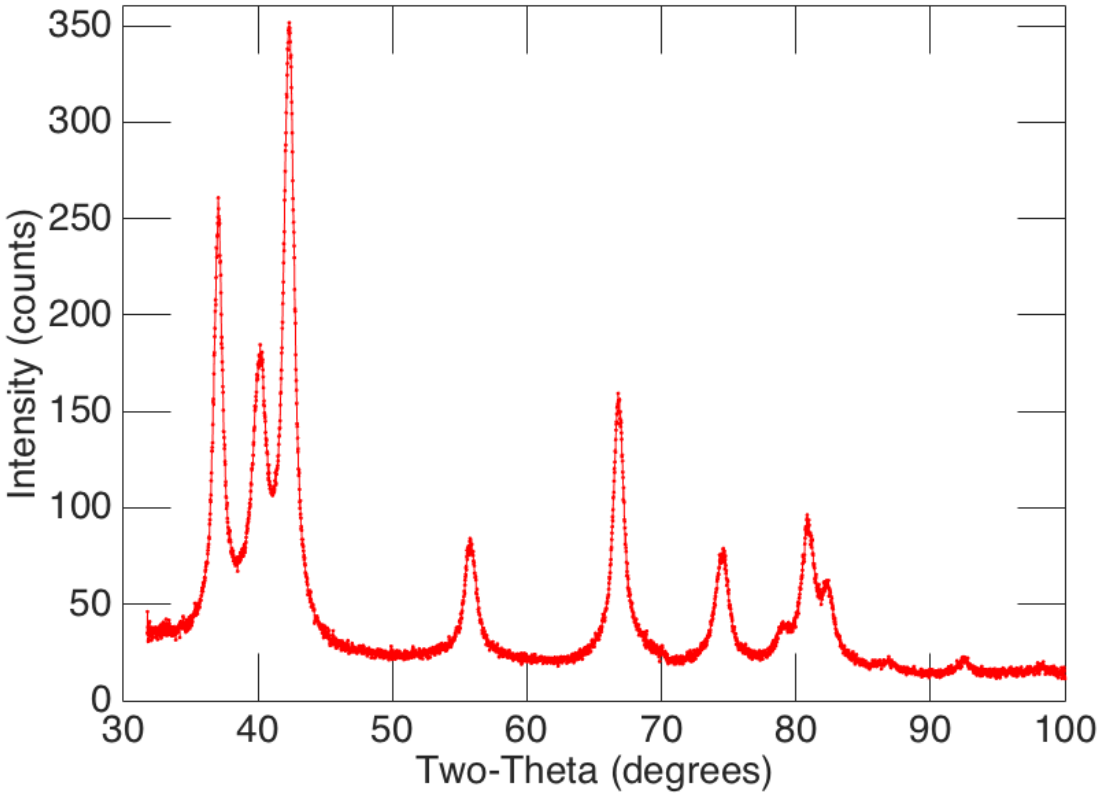

Figure 7.4: X-ray diffraction of ZnO nanocrystals made in the APGD reactor under the following condition: 3 slm of carrier gas (helium) flow, 50 sccm of oxygen flow, 1.5 sccm of DEZ flow and a power density of 14 Wcm^{-3}. The average crystallite size is about 11 nm.

the plasma also increases the production rate from 4 nm/s (20 μg/min) to 100 nm/s (400 μg/min), with higher power density leading to higher production rates. This demonstrates that the plasma electrons significantly enhance the precursor dissociation rate. Due to

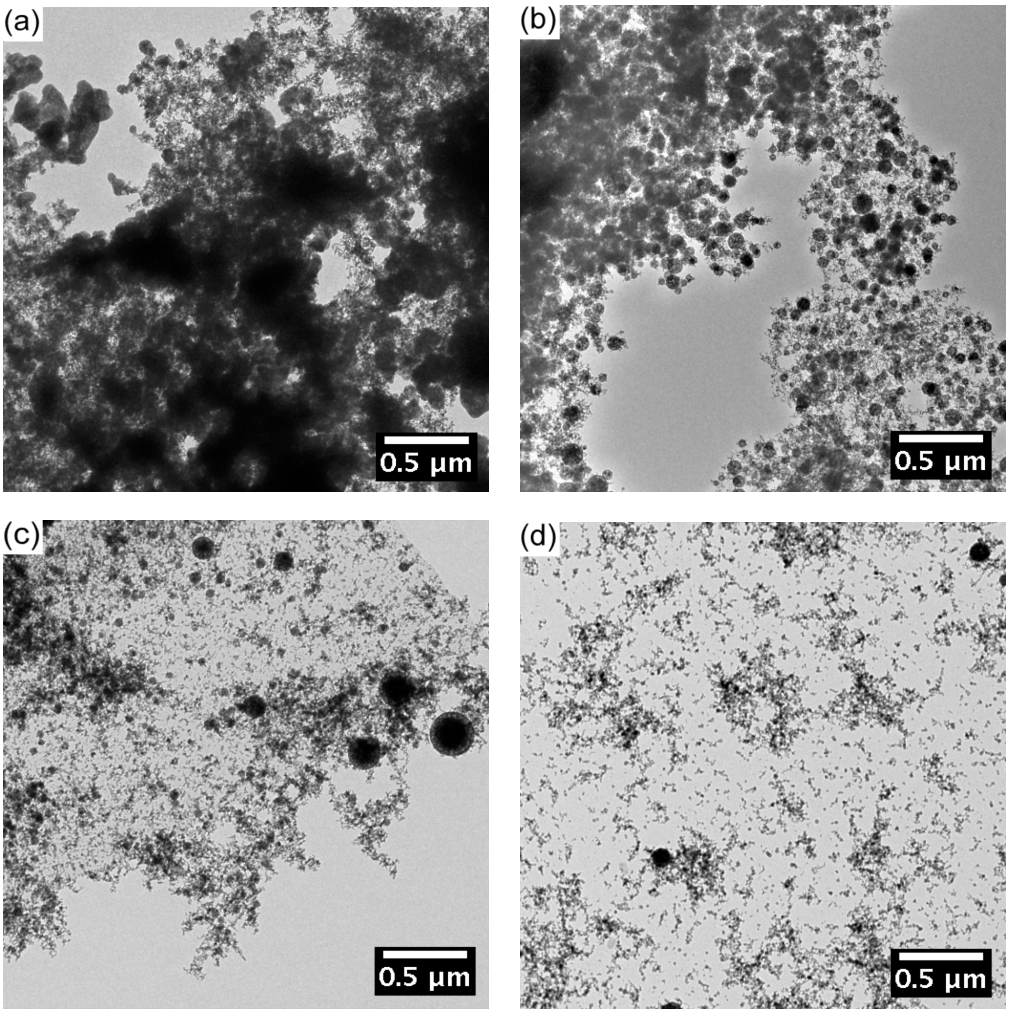

Figure 7.5: The effect of plasma on the size distribution of the synthesized ZnO nanocrystals. (a) No plasma is used and the nanocrystals are formed solely by the oxygen-DEZ reaction, leading to a large size distribution and the presence of large agglomerates. (b) Oxygen and DEZ are allowed to mix and react in the Swagelok connector before entering the plasma; the size distribution is slightly improved. (c) Oxygen and DEZ are not allowed to mix prior to entering the plasma and the size distribution is further improved; however, large agglomerates are still present due to the residual DEZ in the gas lines reacting with oxygen over time. (d) Oxygen and DEZ are not allowed to mix prior to entering the plasma and the gas lines are purged before the experiment; the size distribution is greatly improved. For all cases, the carrier gas flow rate is 3 slm, the oxygen:DEZ ratio is 33 and and the power density is $13 - 18$ Wcm^{-3}.

the particle bounce effect at large Stokes number at atmospheric-pressure [172, 173], the deposition rate greatly drops at large carrier gas flow rate (dropping from 100 nm/s (400 μg/min) at a 3 slm flow rate to 0.9 nm/s (4 μg/min) at a 23 slm flow rate).

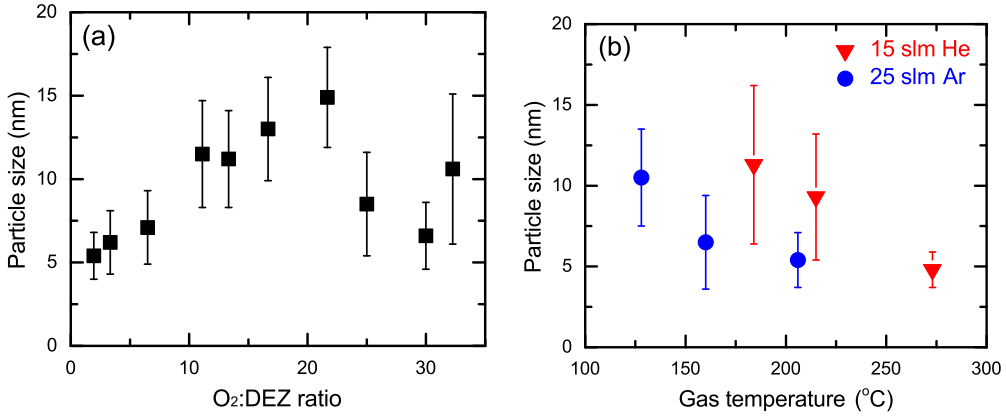

Figure 7.6: Particle size as a function of reactor parameters. (a) Particle size vs. oxygen:DEZ ratio. (b) Particle size vs. gas temperature. Error bars correspond to the standard deviations of the particle size. Other factors are kept approximately constant.

A certain degree of control over the particle size has been achieved by varying the oxygen:DEZ ratio and the gas temperature, as shown in figure 7.6(a) and figure 7.6(b). The average particle size is calculated by measuring 30 randomly selected particles collected on the TEM grid. Figure 7.6(a) shows that the particle size increases for ratios less than 20:1 and decreases for ratios beyond 22:1. This shows that while an oxygen-poor plasma leads to small particles due to insufficient oxygen for complete reaction, an oxygen-rich plasma also suppresses the particle growth due to the diminished plasma density. It's worth pointing out that the particle size keeps increasing even when the O_2 : DEZ ratio is beyond the stoichiometry ratio of 7 : 1. This is possibly due to the impurities present in the DEZ precursor, as discussed earlier. The particle size is primarily affected by the O_2 : DEZ ratio rather than the precursor flow rate: similar particle sizes and standard deviations are produced by flowing 20 sccm O_2 and 0.6 sccm DEZ, and by flowing 50 sccm O_2 and 1.5 sccm DEZ, both having the same O_2: DEZ ratio of 33. Figure 7.6(b) shows that smaller particles are produced at higher gas temperatures, indicating that heating the particles during synthesis by increasing the neutral gas temperature seems to discourage the growth along the faceted surface. This result seems to agree with Kramer's model, demonstrating that the neutral gas molecules indeed play an important role in the atmospheric pressure plasma particle synthesis. Unlike silicon nanocrystals synthesized

in low pressure plasmas, increasing the power alone does not increase the particle size in the atmospheric pressure case. This is because an increased power also leads to increased neutral gas temperature, resulting in smaller particle size. For all cases, larger particle size is often accompanied by a larger standard deviation in particle size, since small particles less than 10 nm are always present, even when the majority of the particles are larger than 10 nm.

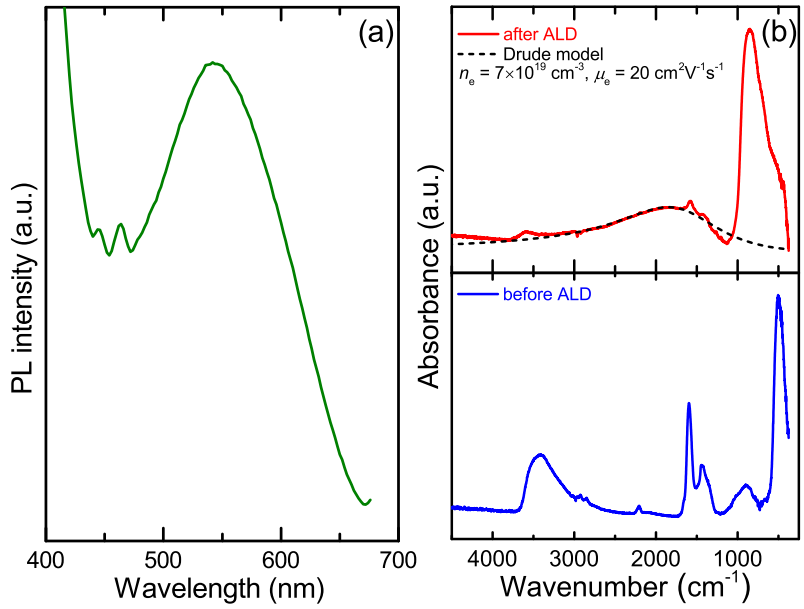

Figure 7.7: Optical properties of the zinc oxide nanocrystals. (a) Photoluminescence spectrum of 4-10 nm nanocrystals dispersed in ethanol and excited by a 350 nm light source. The near-band-gap emission is not visible due to overlap with the source (image courtesy of Jihua Yang). (b) Diffuse reflectance Fourier transform infrared spectra of 7-8 nm nanocrystals deposited on gold-coated silicon substrates before (blue curve) and after (red curve) ALD treatment. Before ALD, OH groups (absorption features at 1600 and 3400 cm^{-1}) on the nanocrystal surfaces trap electrons and suppress the LSPR. The absorption feature at 500 cm^{-1} is due to Zn-O bonds. After ALD, which removes OH groups and seals the nanocrystals, an LSPR absorption feature appears at 1900 cm^{-1}. The absorption feature at 800 cm^{-1} is due to Al-O bonds (image courtesy of Benjamin Greenberg).

A few optical characterizations have been performed on the synthesized nanocrystals. Figure 7.7(a) shows the photoluminescence measurement of 4-10 nm ZnO nanocrystals dispersed in ethanol and excited by a 350 nm light source. The spectrum shows a luminescent peak at 550 nm possibly due to OH groups on the nanocrystal surface. Figure

7.7 (b) shows the Fourier transform infrared spectroscopy (FTIR) spectrum of the ZnO nanocrystals deposited on a gold-coated silicon substrate before and after a 7.7 nm of aluminum oxide coating by atomic layer deposition (ALD). The nanocrystals had an average particle size of 7-8 nm. Similar to the ZnO nanocrystals synthesized under vacuum pressure and deposited using a supersonic flow [171], these ZnO nanocrystals show an air-stable plasmonic resonance at ≈ 1900 cm^{-1} after the aluminum oxide coating. However, performing the same ALD coating on ZnO nanocrystals deposited on a salt substrate did not result in a visible plasmonic resonance. This is likely due to the difference in the size and surface properties of the two kinds of substrates, especially at the atmospheric pressure where the bouncing effect plays an important role.

7.2 Conclusion

This part of the dissertation research presented an APGD reactor for zinc oxide nanoparticle synthesis. This reactor demonstrated that a large volume (non-micro) argon discharge can be maintained in α mode at the atmospheric pressure. The uniformity and stability of the discharge were ensured by using a dielectric barrier, the RF driving frequency, and a pre-ionization technique. The nanoparticle synthesis process showed that the presence of the plasma increased the deposition rate of the ZnO nanoparticles and improved their size distribution. The synthesized zinc oxide particles were crystalline and exhibited photoluminescence in the visible spectrum due to surface defects. Their size and size distribution were mainly affected by three parameters: the carrier gas flow rate, the neutral gas temperature and the oxygen to DEZ ratio. A larger size was observed for a higher carrier gas flow rate, lower neutral gas temperature, and an oxygen to DEZ ratio of about 20 : 1. The deposition rate was affected largely by the carrier gas flow rate and the power density, and slightly by the precursor flow rate. When deposited on a gold-coated silicon wafer and coated with aluminum oxide, the synthesized nanocrystals showed plasmonic resonance at ≈ 1900 cm^{-1}.

Chapter 8

Conclusion

This dissertation research initially focused on the characterization of the dust-plasma interactions at low pressure by measuring the EEPF in a 80 mtorr argon-siline dusty plasma using a Langmuir probe. The probe surface contamination problem was solved by adding a solenoid-actuated shield structure to the probe, physically protecting it from the dust particle deposition. The probe was exposed to the dusty plasma briefly and only during the voltage scan. This, combined with rapid scan cycles and a noise suppression circuity, helped to achieve the first reliable dusty plasma EEPF measurements. The dusty plasma EEPFs were characterized by lower electron density and higher electron temperature accompanied by a drop in the low energy electron population. As the dust particles nucleated and grew in the plasma, the EEPFs showed Maxwellianization. The Langmuir probe measurements was complimented by the capacitive probe measurement, electrical characterization and dust particle collection. From these diagnostics, the ion density and the particle morphology information were obtained. These results were then put into an analytical model of nanoparticle charging to estimate the nanoparticle charge and density in the plasma. It was found that the particles have approximately one elementary charge per nanometer of diameter. The particle density was found to be two orders of magnitude below the electron and ion densities.

The second part of the dissertation focused on studying the dust-plasma interactions at the atmospheric pressure by designing and developing a large volume (non-micro) APGD

reactor for zinc oxide nanoparticle synthesis. The reactor was a capacitively-coupled RF DBD discharge operating in the α mode. Its uniformity at large volume was ensured by the use of a dielectric barrier, a RF driving frequency, and a pre-ionization process induced by a varied gap spacing. The APGD reactor was able to operate stably using either helium or argon as the carrier gas. DEZ and oxygen were injected into the APGD to produce ZnO nanoparticles. A deposition rate of up to 100 nm/s (400 μg/min) was achieved. The nanoparticles were crystalline and their size and size distribution can be controlled by varying the neutral gas temperature and the oxygen to DEZ ratio. A larger size was observed for lower neutral gas temperatures and an oxygen to DEZ ratio of about 20 : 1. The deposition rate was affected largely by the carrier gas flow rate and the power density, and slightly by the precursor flow rate. The nanoparticles typically had diameters ranging from 4 to 15 nm and exhibited PL at $\approx$ 550 nm. After depositing the nanoparticles on a gold-coated silicon wafer and coating the film with aluminum oxide using ALD, the nanoparticles showed LSPR at $\approx$ 1900 cm^{-1}.

By measuring the dusty plasma EEPF for the first time and developing a unique APGD for nanocrystal synthesis, this dissertation research helped to fill a few knowledge gaps in the field of the experimental dusty plasma research. The experimental results presented will be able to compliment the computer simulations and analytical models and help to achieve a more detailed understanding of the dusty plasma physics, which is essential to the improvement of plasma-assisted processes in the nanotechnology laboratories and the nano-manufacturing industry.

References

[1] MA Lieberman and AJ Lichtenberg. Principles of plasma discharges and materials processing. *MRS Bulletin*, 30:899–901, 1994.

[2] PK Shukla. A survey of dusty plasma physics. *Physics of Plasmas (1994-present)*, 8(5):1791–1803, 2001.

[3] PK Shukla and AA Mamun. *Introduction to dusty plasma physics*. CRC Press, 2010.

[4] VA Godyak and VI Demidov. Probe measurements of electron-energy distributions in plasmas: what can we measure and how can we achieve reliable results? *Journal of Physics D: Applied Physics*, 44(23):233001, 2011.

[5] CL Lee and CL Lu. Cf4 plasma etching on linbo3. *Applied Physics Letters*, 35(10):756–758, 1979.

[6] FY Huang and MJ Kushner. Shapes of agglomerates in plasma etching reactors. *Journal of applied physics*, 81(9):5960–5965, 1997.

[7] Gary S Selwyn. Optical characterization of particle traps. *Plasma Sources Science and Technology*, 3(3):340, 1994.

[8] UR Kortshagen, UV Bhandarkar, MT Swihart, Steven L Girshick, et al. Generation and growth of nanoparticles in low-pressure plasmas. *Pure and Applied Chemistry*, 71(10):1871–1878, 1999.

[9] L Mangolini, E Thimsen, and UR Kortshagen. High-yield plasma synthesis of luminescent silicon nanocrystals. *Nano letters*, 5(4):655–659, 2005.

[10] L Mangolini and UR Kortshagen. Plasma-assisted synthesis of silicon nanocrystal inks. *Adv. Mater.*, 19(18):2513–2519, 2007.

[11] NJ Kramer, RJ Anthony, Meenakshi Mamunuru, ES Aydil, and UR Kortshagen. Plasma-induced crystallization of silicon nanoparticles. *Journal of Physics D: Applied Physics*, 47(7):075202, 2014.

[12] O Ishihara. Complex plasma: dusts in plasma. *Journal of Physics D: Applied Physics*, 40(8):R121, 2007.

[13] VE Fortov, AV Ivlev, SA Khrapak, AG Khrapak, and GE Morfill. Complex (dusty) plasmas: Current status, open issues, perspectives. *Physics reports*, 421(1):1–103, 2005.

[14] NN Rao, PK Shukla, and MY Yu. Dust-acoustic waves in dusty plasmas. *Planetary and space science*, 38(4):543–546, 1990.

[15] PK Shukla and VP Silin. Dust ion-acoustic wave. *Physica Scripta*, 45:508, 1992.

[16] A Barkan, N D'Angelo, and RL Merlino. Experiments on ion-acoustic waves in dusty plasmas. *Planetary and Space Science*, 44(3):239–242, 1996.

[17] Y Nakamura, H Bailung, and PK Shukla. Observation of ion-acoustic shocks in a dusty plasma. *Physical review letters*, 83(8):1602, 1999.

[18] C Thompson, A Barkan, N DAngelo, and RL Merlino. Dust acoustic waves in a direct current glow discharge. *Physics of Plasmas (1994-present)*, 4(7):2331–2335, 1997.

[19] A Usachev, A Zobnin, O Petrov, V Fortov, MH Thoma, H Höfner, M Fink, A Ivlev, and G Morfill. Externally excited planar dust acoustic shock waves in a strongly coupled dusty plasma under microgravity conditions. *New Journal of Physics*, 16(5):053028, 2014.

[20] JH Chu and I Lin. Direct observation of coulomb crystals and liquids in strongly coupled rf dusty plasmas. *Physical review letters*, 72(25):4009, 1994.

[21] H Thomas, GE Morfill, V Demmel, J Goree, B Feuerbacher, and D Möhlmann. Plasma crystal: Coulomb crystallization in a dusty plasma. *Physical Review Letters*, 73(5):652, 1994.

[22] RA Quinn, C Cui, J Goree, JB Pieper, H Thomas, and GE Morfill. Structural analysis of a coulomb lattice in a dusty plasma. *Physical Review E*, 53(3):R2049, 1996.

[23] JB Pieper, J Goree, and RA Quinn. Three-dimensional structure in a crystallized dusty plasma. *Physical Review E*, 54(5):5636, 1996.

[24] VE Fortov, OS Vaulina, OF Petrov, VI Molotkov, AV Chernyshev, AM Lipaev, G Morfill, H Thomas, H Rotermell, SA Khrapak, et al. Dynamics of macroparticles in a dusty plasma under microgravity conditions (first experiments on board the iss). *Journal of Experimental and Theoretical Physics*, 96(4):704–718, 2003.

[25] S Khrapak, D Samsonov, G Morfill, H Thomas, V Yaroshenko, H Rothermel, T Hagl, V Fortov, A Nefedov, V Molotkov, et al. Compressional waves in complex (dusty) plasmas under microgravity conditions. *Physics of Plasmas (1994-present)*, 10(1):1–4, 2003.

[26] MR Akdim and WJ Goedheer. Modeling the effect of dust on the plasma parameters in a dusty argon discharge under microgravity. *Physical Review E*, 67(6):066407, 2003.

[27] E Thomas Jr, RL Merlino, and M Rosenberg. Magnetized dusty plasmas: the next frontier for complex plasma research. *Plasma Physics and Controlled Fusion*, 54(12):124034, 2012.

[28] M Schwabe, U Konopka, P Bandyopadhyay, and GE Morfill. Pattern formation in a complex plasma in high magnetic fields. *Physical review letters*, 106(21):215004, 2011.

[29] J Goree. Charging of particles in a plasma. *Plasma Sources Science and Technology*, 3(3):400, 1994.

[30] EC Whipple, TG Northrop, and DA Mendis. The electrostatics of a dusty plasma. *Journal of Geophysical Research: Space Physics (1978–2012)*, 90(A8):7405–7413, 1985.

[31] M Lampe, G Joyce, G Ganguli, and V Gavrishchaka. Interactions between dust grains in a dusty plasma. *Physics of Plasmas (1994-present)*, 7(10):3851–3861, 2000.

[32] O Havnes, TK Aanesen, and F Melandsø. On dust charges and plasma potentials in a dusty plasma with dust size distribution. *Journal of Geophysical Research: Space Physics (1978–2012)*, 95(A5):6581–6585, 1990.

[33] A Bouchoule and L Boufendi. Particulate formation and dusty plasma behaviour in argon-silane rf discharge. *Plasma Sources Science and Technology*, 2(3):204, 1993.

[34] S Ratynskaia, S Khrapak, A Zobnin, MH Thoma, M Kretschmer, A Usachev, V Yaroshenko, RA Quinn, GE Morfill, O Petrov, et al. Experimental determination of dust-particle charge in a discharge plasma at elevated pressures. *Physical review letters*, 93(8):085001, 2004.

[35] L Boufendi and A Bouchoule. Particle nucleation and growth in a low-pressure argon-silane discharge. *Plasma Sources Science and Technology*, 3(3):262, 1994.

[36] A Melzer, S Hübner, L Lewerentz, K Matyash, R Schneider, and R Ikkurthi. Phase-resolved optical emission of dusty rf discharges: Experiment and simulation. *Physical Review E*, 83(3):036411, 2011.

[37] DN Polyakov, VV Shumova, LM Vasilyak, and VE Fortov. Study of glow discharge positive column with cloud of disperse particles. *Physics Letters A*, 375(37):3300–3305, 2011.

[38] Ch Hollenstein. The physics and chemistry of dusty plasmas. *Plasma physics and controlled fusion*, 42(10):R93, 2000.

[39] M Gatti and UR Kortshagen. Analytical model of particle charging in plasmas over a wide range of collisionality. *Physical Review E*, 78(4):046402, 2008.

[40] GI Sukhinin and AV Fedoseev. Influence of dust-particle concentration on gas-discharge plasma. *Physical Review E*, 81(1):016402, 2010.

[41] MJ McCaughey and MJ Kushner. A model for particulate contaminated glow discharges. *Journal of applied physics*, 69(10):6952–6961, 1991.

[42] JP Boeuf. Characteristics of a dusty nonthermal plasma from a particle-in-cell monte carlo simulation. *Physical Review A*, 46(12):7910, 1992.

[43] K Ostrikov, I Denysenko, MY Yu, and S Xu. Electron energy distribution function in low-pressure complex plasmas. *Journal of plasma physics*, 71(02):217–224, 2005.

[44] WJ Goedheer, MR Akdim, and Yu I Chutov. Hydrodynamic and kinetic modelling of dust free and dusty radio-frequency discharges. *Contributions to Plasma Physics*, 44(5-6):395–404, 2004.

[45] DZ Wang and JQ Dong. Kinetics of low pressure rf discharges with dust particles. *Journal of applied physics*, 81(1):38–42, 1997.

[46] I Denysenko, K Ostrikov, MY Yu, and NA Azarenkov. Behavior of the electron temperature in nonuniform complex plasmas. *Physical Review E*, 74(3):036402, 2006.

[47] I Denysenko, MY Yu, K Ostrikov, NA Azarenkov, and L Stenflo. A kinetic model for an argon plasma containing dust grains. *Physics of Plasmas (1994-present)*, 11(11):4959–4967, 2004.

[48] I Denysenko, MY Yu, K Ostrikov, and A Smolyakov. Spatially averaged model of complex-plasma discharge with self-consistent electron energy distribution. *Physical Review E*, 70(4):046403, 2004.

[49] I Denysenko, MY Yu, and S Xu. Effect of plasma nonuniformity on electron energy distribution in a dusty plasma. *Journal of Physics D: Applied Physics*, 38(3):403, 2005.

[50] S Kanazawa, Moriwaki Kogoma, T Moriwaki, and S Okazaki. Stable glow plasma at atmospheric pressure. *J. Phys. D: Appl. Phys.*, 21(5):838, 1988.

[51] F Massines, A Rabehi, P Decomps, RB Gadri, P Ségur, and C Mayoux. Experimental and theoretical study of a glow discharge at atmospheric pressure controlled by dielectric barrier. *J. Appl. Phys.*, 83(6):2950–2957, 1998.

[52] D Staack, B Farouk, A Gutsol, and A Fridman. Characterization of a dc atmospheric pressure normal glow discharge. *Plasma Sources Sci. Technol., PSST*, 14(4):700, 2005.

[53] J Roth, J Rahel, X Dai, and D Sherman. The physics and phenomenology of one atmosphere uniform glow discharge plasma (oaugdp) reactors for surface treatment applications. *J. Phys. D: Appl. Phys.*, 38(4):555, 2005.

[54] AJ Beaulieu. Transversely excited atmospheric pressure co2 lasers. *Appl. Phys. Lett.*, 16(12):504–505, 1970.

[55] WB Tiffany, R Targ, and JD Foster. Kilowatt co2 gas-transport laser. *Appl. Phys. Lett.*, 15(3):91–93, 1969.

[56] K Watanabe, S Kashiwabara, K Sawai, S Toshima, and R Fujimoto. Performance characteristics of a transverse-flow, oxygen-iodine chemical laser in a low gas-flow velocity. *J. Appl. Phys.*, 54(3):1228–1231, 1983.

[57] KM Abramski, AD Colley, HJ Baker, and DR Hall. Power scaling of large-area transverse radio frequency discharge co2 lasers. *Appl. Phys. Lett.*, 54(19):1833–1835, 1989.

[58] DJ Benard, WC McDermott, NR Pchelkin, and RR Bousek. Efficient operation of a 100-w transverse-flow oxygen-iodine chemical laser. *Appl. Phys. Lett.*, 34(1):40–41, 1979.

[59] S Sato and M Taniwaki. 1-kw, capacitively coupled radio frequency discharge excited co laser with a closed-cycle fast axial flow. *Appl. Phys. Lett.*, 61(6):621–623, 1992.

[60] P Pearson and H Lamberton. Atmospheric pressure co 2 lasers giving high output energy per unit volume. *IEEE J. Quant. Electron.*, 8(2):145–149, 1972.

[61] AK Laflamme. Double discharge excitation for atmospheric pressure co2 lasers. *Rev. Sci. Instrum.*, 41(11):1578–1581, 1970.

[62] JJ Shi, DW Liu, and MG Kong. Effects of dielectric barriers in radio-frequency atmospheric glow discharges. *IEEE Trans. Plasma Sci.*, 35(2):137–142, 2007.

[63] V Vons, Y Creyghton, and A Schmidt-Ott. Nanoparticle production using atmospheric pressure cold plasma. *J. Nanopart. Res.*, 8(5):721–728, 2006.

[64] S Askari, I Levchenko, K Ostrikov, P Maguire, and D Mariotti. Crystalline si nanoparticles below crystallization threshold: Effects of collisional heating in non-thermal atmospheric-pressure microplasmas. *Appl. Phys. Lett.*, 104(16):163103, 2014.

[65] RM Sankaran, D Holunga, RC Flagan, and KP Giapis. Synthesis of blue luminescent si nanoparticles using atmospheric-pressure microdischarges. *Nano Lett.*, 5(3):537–541, 2005.

[66] T Nozaki, K Sasaki, T Ogino, D Asahi, and K Okazaki. Microplasma synthesis of tunable photoluminescent silicon nanocrystals. *Nanotechnology*, 18(23):235603, 2007.

[67] T Nozaki, K Sasaki, T Ogino, D Asahi, and K Okazaki. Silicon nanocrystal synthesis in microplasma reactor. *J. Therm. Sci. Tech-JPN.*, 2(2):192–199, 2007.

[68] Souvik Ghosh, Tianqi Liu, Mihai Bilici, Jonathan Cole, I-Min Huang, David Staack, Davide Mariotti, and R Mohan Sankaran. Atmospheric-pressure dielectric barrier discharge with capillary injection for gas-phase nanoparticle synthesis. *J. Phys. D: Appl. Phys.*, 48(31):314003, 2015.

[69] N. Layadi, JI Colonell, and JT Lee. An introduction to plasma etching for vlsi circuit technology. *Bell Labs technical journal*, 4(3):155–171, 1999.

[70] PC Boyle, AR Ellingboe, and MM Turner. Independent control of ion current and ion impact energy onto electrodes in dual frequency plasma devices. *Journal of Physics D: Applied Physics*, 37(5):697, 2004.

[71] NJ Kramer, ES Aydil, and UR Kortshagen. Requirements for plasma synthesis of nanocrystals at atmospheric pressures. *Journal of Physics D: Applied Physics*, 48(3):035205, 2015.

[72] R Gresback, Z Holman, and UR Kortshagen. Nonthermal plasma synthesis of size-controlled, monodisperse, freestanding germanium nanocrystals. *Appl. Phys. Lett.*, 91(9):093119, 2007.

[73] L Mangolini, D Jurbergs, E Rogojina, and U Kortshagen. Plasma synthesis and liquid-phase surface passivation of brightly luminescent si nanocrystals. *J. Lumin.*, 121(2):327–334, 2006.

[74] L Mangolini, D Jurbergs, E Rogojina, and U Kortshagen. High efficiency photoluminescence from silicon nanocrystals prepared by plasma synthesis and organic surface passivation. *physica status solidi (c)*, 3(11):3975–3978, 2006.

[75] R Gresback, T Nozaki, and K Okazaki. Synthesis and oxidation of luminescent silicon nanocrystals from silicon tetrachloride by very high frequency nonthermal plasma. *Nanotechnology*, 22(30):305605, 2011.

[76] UR Kortshagen. Nonthermal plasma synthesis of semiconductor nanocrystals. *J. Phys. D: Appl. Phys.*, 42(11):113001, 2009.

[77] XD Pi, RW Liptak, J Deneen Nowak, NP Wells, CB Carter, SA Campbell, and U Kortshagen. Air-stable full-visible-spectrum emission from silicon nanocrystals synthesized by an all-gas-phase plasma approach. *Nanotechnology*, 19(24):245603, 2008.

[78] IV Schweigert, AL Alexandrov, DA Ariskin, FM Peeters, I Stefanović, Eva Kovačević, Johannes Berndt, and Jörg Winter. Effect of transport of growing nanoparticles on capacitively coupled rf discharge dynamics. *Physical Review E*, 78(2):026410, 2008.

[79] S Kona, JH Kim, CK Harnett, and MK Sunkara. Carbon nanotube growth studies using an atmospheric, microplasma reactor. *IEEE Trans. Nanotechnol.*, 8(3):286–290, 2009.

[80] I Levchenko, K Ostrikov, and D Mariotti. The production of self-organized carbon connections between ag nanoparticles using atmospheric microplasma synthesis. *Carbon*, 47(1):344–347, 2009.

[81] Y Shimizu, T Sasaki, T Ito, K Terashima, and N Koshizaki. Fabrication of spherical carbon via uhf inductively coupled microplasma cvd. *J. Phys. D: Appl. Phys.*, 36(23):2940, 2003.

[82] C Richmonds and RM Sankaran. Plasma-liquid electrochemistry: rapid synthesis of colloidal metal nanoparticles by microplasma reduction of aqueous cations. *Appl. Phys. Lett.*, 93(13):131501, 2008.

[83] D Vendor and RW Boswell. Numerical modeling of low-pressure rf plasmas. *Plasma Science, IEEE Transactions on*, 18(4):725–732, 1990.

[84] I Stefanović, B Sikimić, A Aschinger, J Berndt, E Kovačević, and J Winter. Development of voids in pulsed and cw-driven reactive plasmas with large nanoparticle density. *Journal of Physics D: Applied Physics*, 48(38):385202, 2015.

[85] D Samsonov and J Goree. Instabilities in a dusty plasma with ion drag and ionization. *Physical Review E*, 59(1):1047, 1999.

[86] CH Courteille, CH Hollenstein, JL Dorier, P Gay, W Schwarzenbach, AA Howling, E Bertran, G Viera, R Martins, and A Macarico. Particle agglomeration study in rf silane plasmas: Insitu study by polarization-sensitive laser light scattering. *Journal of applied physics*, 80(4):2069–2078, 1996.

[87] L Boufendi, J Hermann, A Bouchoule, B Dubreuil, E Stoffels, WW Stoffels, and ML De Giorgi. Study of initial dust formation in an ar-sih4 discharge by laser induced particle explosive evaporation. *Journal of applied physics*, 76(1):148–153, 1994.

[88] A Bouchoule, A Plain, L Boufendi, J Ph Blondeau, and C Laure. Particle generation and behavior in a silane-argon low-pressure discharge under continuous or pulsed radio-frequency excitation. *Journal of applied physics*, 70(4), 1991.

[89] G Praburam and J Goree. Experimental observation of very low-frequency macroscopic modes in a dusty plasma. *Physics of Plasmas (1994-present)*, 3(4):1212–1219, 1996.

[90] Z Ehsan, NL Tsintsadze, and S Poedts. A modified orbital motion limited (oml) theory. *arXiv preprint arXiv:1110.6304*, 2011.

[91] JE Allen, BM Annaratone, and U De Angelis. On the orbital motion limited theory for a small body at floating potential in a maxwellian plasma. *Journal of plasma physics*, 63(04):299–309, 2000.

[92] M Lampe. Limits of validity for orbital-motion-limited theory for a small floating collector. *Journal of plasma physics*, 65(03):171–180, 2001.

[93] RV Kennedy and JE Allen. The floating potential of spherical probes and dust grains. part 1. radial motion theory. *Journal of plasma physics*, 67(04):243–250, 2002.

[94] C Cui and J Goree. Fluctuations of the charge on a dust grain in a plasma. *Plasma Science, IEEE Transactions on*, 22(2):151–158, 1994.

[95] M Lampe, V Gavrishchaka, G Ganguli, and G Joyce. Effect of trapped ions on shielding of a charged spherical object in a plasma. *Physical review letters*, 86(23):5278, 2001.

[96] AV Zobnin, AP Nefedov, VA SinelShchikov, and VE Fortov. On the charge of dust particles in a low-pressure gas discharge plasma. *Journal of Experimental and Theoretical Physics*, 91(3):483–487, 2000.

[97] RN Varney. Mean free paths, ion drift velocities, and the poisson distribution. *American Journal of Physics*, 39:534–538, 1971.

[98] VA Godyak and RB Piejak. Abnormally low electron energy and heating-mode transition in a low-pressure argon rf discharge at 13.56 mhz. *Physical review letters*, 65(8):996, 1990.

[99] N Bilik, R Anthony, BA Merritt, ES Aydil, and UR Kortshagen. Langmuir probe measurements of electron energy probability functions in dusty plasmas. *Journal of Physics D: Applied Physics*, 48(10):105204, 2015.

[100] L Conde. An introduction to langmuir probe diagnostics of plasmas. *Madrid: Dept. Física. ETSI Aeronáut ngenieros Aeronáuticos Universidad Politécnica de Madrid*, 2011.

[101] VA Godyak, RB Piejak, and BM Alexandrovich. Electron energy distribution function measurements and plasma parameters in inductively coupled argon plasma. *Plasma Sources Science and Technology*, 11(4):525, 2002.

[102] RJ d'Arcy. Dielectric impurities and surface instability in langmuir probe plasma measurements. *Journal of Physics D: Applied Physics*, 7(10):1391, 1974.

[103] A Bouchoule and L Boufendi. High concentration effects in dusty plasmas. *Plasma Sources Science and Technology*, 3(3):292, 1994.

[104] M Klindworth, O Arp, and A Piel. Langmuir probe system for dusty plasmas under microgravity. *Review of scientific instruments*, 78(3):033502, 2007.

[105] E Thomas Jr and M Watson. First experiments in the dusty plasma experiment device. *Physics of Plasmas (1994-present)*, 6(10):4111–4117, 1999.

[106] RA Quinn and J Goree. Experimental investigation of particle heating in a strongly coupled dusty plasma. *Physics of Plasmas (1994-present)*, 7(10):3904–3911, 2000.

[107] RA Quinn and J Goree. Single-particle langevin model of particle temperature in dusty plasmas. *Physical Review E*, 61(3):3033, 2000.

[108] K Tachibana, Y Hayashi, T Okuno, and T Tatsuta. Spectroscopic and probe measurements of structures in a parallel-plates rf discharge with particles. *Plasma Sources Science and Technology*, 3(3):314, 1994.

[109] E Thomas Jr, K Avinash, and RL Merlino. Probe induced voids in a dusty plasma. *Physics of Plasmas (1994-present)*, 11(5):1770–1774, 2004.

[110] JB Pieper and J Goree. Dispersion of plasma dust acoustic waves in the strong-coupling regime. *Physical review letters*, 77(15):3137, 1996.

[111] UR Kortshagen, C Busch, and LD Tsendin. On simplifying approaches to the solution of the boltzmann equation in spatially inhomogeneous plasmas. *Plasma Sources Science and Technology*, 5(1):1, 1996.

[112] VI Demidov, SV Ratynskaia, and K Rypdal. Electric probes for plasmas: The link between theory and instrument. *Review of scientific instruments*, 73(10):3409–3439, 2002.

[113] LD Tsendin. Energy distribution of electrons in a weakly ionized current-carrying plasma with a transverse inhomogeneity. *Sov. Phys. JETP*, 39(5):805–810, 1974.

[114] N St J Braithwaite, JP Booth, and G Cunge. A novel electrostatic probe method for ion flux measurements. *Plasma Sources Science and Technology*, 5(4):677, 1996.

[115] MC Petcu, AC Bronneberg, Aniruddha Sarkar, MA Blauw, M Creatore, and MCM van de Sanden. A capacitive probe with shaped probe bias for ion flux measurements in depositing plasmas. *Review of Scientific Instruments*, 79(11):115104, 2008.

[116] H-B Valentini. Bohm criterion for the collisional sheath. *Physics of Plasmas (1994-present)*, 3(4):1459–1461, 1996.

[117] D Lee, L Oksuz, and N Hershkowitz. Exact solution for the generalized bohm criterion in a two-ion-species plasma. *Physical review letters*, 99(15):155004, 2007.

[118] KU Riemann. The bohm criterion and boundary conditions for a multicomponent system. *Plasma Science, IEEE Transactions on*, 23(4):709–716, 1995.

[119] PC Stangeby. The bohm–chodura plasma sheath criterion. *Physics of Plasmas (1994-present)*, 2(3):702–706, 1995.

[120] VA Godyak. Modified bohm criterion for a collisional plasma. *Physics Letters A*, 89(2):80–81, 1982.

[121] K Riemann. The influence of collisions on the plasma sheath transition. *Physics of plasmas*, 4(11), 1997.

[122] RN Franklin. Plasmas with more than one species of positive ion and the bohm criterion. *Journal of Physics D: Applied Physics*, 33(24):3186, 2000.

[123] HB Valentini and F Herrmann. Boundary value problems for multi-component plasmas and a generalized bohm criterion. *Journal of Physics D: Applied Physics*, 29(5):1175, 1996.

[124] RN Franklin and J Snell. The plasma-sheath transition with a constant mean free path model and the applicability of the bohm criterion. *Physics of Plasmas (1994-present)*, 8(2):643–647, 2001.

[125] VV Yaroshenko, Frank Verheest, HM Thomas, and GE Morfill. The bohm sheath criterion in strongly coupled complex plasmas. *New Journal of Physics*, 11(7):073013, 2009.

[126] JX Ma and MY Yu. Electrostatic sheath at the boundary of a dusty plasma. *Physics of Plasmas (1994-present)*, 2(4):1343–1348, 1995.

[127] BP Pandey and A Dutta. The bohm criterion for a dusty plasma sheath. *Pramana*, 65(1):117–124, 2005.

[128] JY Liu, ZX Wang, XG Wang, Q Zhang, X Zou, and Y Zhang. The bohm criterion for the dusty plasma sheath. *Physics of Plasmas (1994-present)*, 10(9):3507–3511, 2003.

[129] VA Godyak and RB Piejak. Insitu simultaneous radio frequency discharge power measurements. *Journal of Vacuum Science & Technology A*, 8(5):3833–3837, 1990.

[130] F Galli. *Charge and energy interactions between nanoparticles and low pressure plasmas*. PhD thesis, UNIVERSITY OF MINNESOTA, 2010.

[131] J Roth. *Industrial Plasma Engineering: Volume 2-Applications to Nonthermal Plasma Processing*, volume 2. CRC Press, 2001.

[132] S El-Khabiry and GM Colver. Drag reduction by dc corona discharge along an electrically conductive flat plate for small reynolds number flow. *Physics of Fluids (1994-present)*, 9(3):587–599, 1997.

[133] C Tendero, C Tixier, P Tristant, J Desmaison, and P Leprince. Atmospheric pressure plasmas: A review. *Spectrochimica Acta Part B: Atomic Spectroscopy*, 61(1):2–30, 2006.

[134] MI Boulos, P Fauchais, and E Pfender. Thermal plasma-fundamental and applications, vol. 1, 1994.

[135] D Mariotti and RM Sankaran. Perspectives on atmospheric-pressure plasmas for nanofabrication. *Journal of Physics D: Applied Physics*, 44(17):174023, 2011.

[136] D Mariotti. Nonequilibrium and effect of gas mixtures in an atmospheric microplasma. *Applied Physics Letters*, 92(15):151505, 2008.

[137] J Park, I Henins, HW Herrmann, GS Selwyn, JY Jeong, RF Hicks, D Shim, and CS Chang. An atmospheric pressure plasma source. *Applied Physics Letters*, 76(3):288–290, 2000.

[138] X Yang, M Moravej, GR Nowling, SE Babayan, J Panelon, JP Chang, and RF Hicks. Comparison of an atmospheric pressure, radio-frequency discharge operating in the α and γ modes. *Plasma Sources Science and Technology*, 14(2):314, 2005.

[139] JJ Shi and MG Kong. Mode characteristics of radio-frequency atmospheric glow discharges. *Plasma Science, IEEE Transactions on*, 33(2):624–630, 2005.

[140] G Dilecce and S De Benedictis. Laser diagnostics of high-pressure discharges: laser induced fluorescence detection of oh in he/ar–h2o dielectric barrier discharges. *Plasma Physics and Controlled Fusion*, 53(12):124006, 2011.

[141] SZ Li, JP Lim, JG Kang, and HS Uhm. Comparison of atmospheric-pressure helium and argon plasmas generated by capacitively coupled radio-frequency discharge. *Physics of Plasmas (1994-present)*, 13(9):093503, 2006.

[142] S Wang, V Schulz-von Der Gathen, and HF Dobele. Discharge comparison of nonequilibrium atmospheric pressure ar/o 2 and he/o 2 plasma jets. *Applied physics letters*, 83(16):3272–3274, 2003.

[143] M Moravej, X Yang, GR Nowling, JP Chang, RF Hicks, and SE Babayan. Physics of high-pressure helium and argon radio-frequency plasmas. *J. Appl. Phys.*, 96(12):7011–7017, 2004.

[144] SY Moon, J Han, and W Choe. Control of radio-frequency atmospheric pressure argon plasma characteristics by helium gas mixing. *Physics of Plasmas (1994-present)*, 13(1):013504, 2006.

[145] A Fridman, A Chirokov, and A Gutsol. Non-thermal atmospheric pressure discharges. *Journal of Physics D: Applied Physics*, 38(2):R1, 2005.

[146] J Park, I Henins, HW Herrmann, GS Selwyn, and RF Hicks. Discharge phenomena of an atmospheric pressure radio-frequency capacitive plasma source. *J. Appl. Phys.*, 89(1):20–28, 2001.

[147] J Park, I Henins, HW Herrmann, and GS Selwyn. Gas breakdown in an atmospheric pressure radio-frequency capacitive plasma source. *journal of Applied Physics*, 89(1):15–19, 2001.

[148] Xiaohui Yuan and Laxminarayan L Raja. Role of trace impurities in large-volume noble gas atmospheric-pressure glow discharges. *Applied physics letters*, 81(5):814–816, 2002.

[149] AJ Palmer. A physical model on the initiation of atmospheric-pressure glow discharges. *Appl. Phys. Lett.*, 25(3):138–140, 1974.

[150] T Yokoyama, Moriwaki Kogoma, T Moriwaki, and S Okazaki. The mechanism of the stabilisation of glow plasma at atmospheric pressure. *Journal of Physics D: Applied Physics*, 23(8):1125, 1990.

[151] M Moravej and RF Hicks. Atmospheric plasma deposition of coatings using a capacitive discharge source. *Chemical vapor deposition*, 11(11-12):469–476, 2005.

[152] U Kogelschatz and B Eliasson. Fundamentals and applications of dielectric barrier discharges. In *HAKONE VII Int. Symp. On High Pressure Low Temperature Plasma Chemistry, Greifswald*, 2000.

[153] DW Liu, JJ Shi, and Michael G Kong. Electron trapping in radio-frequency atmospheric-pressure glow discharges. *Applied physics letters*, 90(4):041502, 2007.

[154] JJ Shi and Michael G Kong. Mechanisms of the α and γ modes in radio-frequency atmospheric glow discharges. *Journal of applied physics*, 97(2):023306, 2005.

[155] F Massines, P Segur, N Gherardi, C Khamphan, and A Ricard. Physics and chemistry in a glow dielectric barrier discharge at atmospheric pressure: diagnostics and modelling. *Surface and Coatings Technology*, 174:8–14, 2003.

[156] A Fridman and L Kennedy. *Plasma physics and engineering*. CRC press, 2004.

[157] J Dutton, F Llewellyn-Jones, and DB Rees. Ionization coefficients in helium at high pressures. *Nature*, 1963.

[158] M Kossitsyn, A Gutsol, and A Fridman. Generation and diagnostics of non-equilibrium plasma in gliding arc discharge. In *Electronic Proceedings of 16th International Symposium on Plasma Chemistry, Taormina, Italy*, 2003.

[159] EE Kunhardt. Generation of large-volume, atmospheric-pressure, nonequilibrium plasmas. *IEEE Trans. Plasma Sci.*, 28(1):189–200, 2000.

[160] R Pearse, A Gaydon, and R Pearse. *The identification of molecular spectra*, volume 297. Chapman and Hall London, 1976.

[161] M Mitchner and CH Kruger. *Partially ionized gases*, volume 8. Wiley New York, 1973.

[162] J Annaloro, V Morel, A Bultel, and P Omaly. Global rate coefficients for ionization and recombination of carbon, nitrogen, oxygen, and argon. *Physics of Plasmas (1994-present)*, 19(7):073515, 2012.

[163] W Lotz. Electron-impact ionization cross-sections and ionization rate coefficients for atoms and ions from hydrogen to calcium. *Zeitschrift für Physik*, 216(3):241–247, 1968.

[164] LS Frost and AV Phelps. Momentum-transfer cross sections for slow electrons in he, ar, kr, and xe from transport coefficients. *Physical Review*, 136(6A):A1538, 1964.

[165] H Petersen. The properties of helium: density, specific heats, viscosity, and thermal conductivity at pressures from 1 to 100 bar and from room temperature to about 1800 k. Technical report, 1970.

[166] C Evers, HW Lösch, and W Wagner. An absolute viscometer-densimeter and measurements of the viscosity of nitrogen, methane, helium, neon, argon, and krypton over a wide range of density and temperature. *International journal of thermophysics*, 23(6):1411–1439, 2002.

[167] SY Moon and W Choe. A comparative study of rotational temperatures using diatomic oh, o and n molecular spectra emitted from atmospheric q 2 2 plasmas. *Spectrochimica Acta Part B*, 58:249–257, 2003.

[168] PP Vitruk, HJ Baker, and DR Hall. The characteristics and stability of high power transverse radio frequency discharges for waveguide co2 slab laser excitation. *Journal of Physics D: Applied Physics*, 25(12):1767, 1992.

[169] A Janotti and CG Van de Walle. Fundamentals of zinc oxide as a semiconductor. *Reports on Progress in Physics*, 72(12):126501, 2009.

[170] Ü Özgür, Y Alivov, C Liu, A Teke, MAn Reshchikov, S Doğan, VCSJ Avrutin, SJ Cho, and H Morkoc. A comprehensive review of zno materials and devices. *Journal of applied physics*, 98(4):041301, 2005.

[171] E Thimsen, M Johnson, X Zhang, AJ Wagner, KA Mkhoyan, UR Kortshagen, and ES Aydil. High electron mobility in thin films formed via supersonic impact deposition of nanocrystals synthesized in nonthermal plasmas. *Nat. commun.*, 5, 2014.

[172] SS Pak, BYH Liu, and KL Rubow. Effect of coating thickness on particle bounce in inertial impactors. *Aerosol Sci. Technol.*, 16(3):141–150, 1992.

[173] MJ Ellenbecker, D Leith, and JM Price. Impaction and particle bounce at high stokes numbers. *J. Air Pollut. Control Assoc.*, 30(11):1224–1227, 1980.

[174] CJ Tsai and YH Cheng. Solid particle collection characteristics on impaction surfaces of different designs. *Aerosol Science and Technology*, 23(1):96–106, 1995.

[175] C Wöll. The chemistry and physics of zinc oxide surfaces. *Progress in Surface Science*, 82(2):55–120, 2007.